

Radiation from particles revolving around a magnetized  
Schwarzschild black hole

by

Christos C. Tzounis

A thesis submitted in partial fulfillment of the requirements for the degree of

Doctor of Philosophy

Department of Physics  
University of Alberta

©Christos C. Tzounis, 2016

## Abstract

One of the methods of study of black holes in astrophysics is based on broadening of the spectrum of radiation of ionized iron atoms. The line  $K\alpha$  associated with iron emission at 6.4 keV is very narrow. If such an ion is revolving around a black hole, this line is effectively broadened as a result of the Doppler and gravitational redshift effects. The profile of the broadened spectrum contains information about the gravitational field of the black hole. In the presence of a regular magnetic field in the vicinity of a black hole, the characteristics of the motion of charged ions are modified. In particular, their innermost stable circular orbits become closer to the horizon. The purpose of this work is to study how this effect modifies the spectrum broadening of lines emitted by such an ion. Our final goal is to analyze whether the change of the spectrum profiles can give us information about the magnetic field in the black hole vicinity.

## Preface

There is more and more evidence that astrophysical black holes exist [1, 2, 3, 4, 5, 6, 7, 8, 9, 10, 11, 12, 13, 14, 15]. An example of such evidence is the discovery of black hole mergers from LIGO due to the gravitational waves that are produced during the process of two black holes becoming one. There were two events that were observed, the first one was the gravitational waves produced by the merging of a  $36M_{\odot}$  and a  $29M_{\odot}$  mass black holes [16]. The second observation was published recently and it is the gravitational waves produced by the merging of a  $14.2M_{\odot}$  and a  $7.5M_{\odot}$  mass black hole [17]. Another example of a program that should provide further evidence that astrophysical black hole exists is the Event Horizon Telescope program which is planned to probe in the next decade the apparent shape (“shadow”) of the black hole (Sagittarius  $A^*$ )<sup>1</sup> in the centre of our galaxy via Very Long Baseline Interferometry [18]. Black hole candidates (both stellar mass and supermassive) are identified by observing that a large mass compact object is located in a region of sufficiently small size, which practically excludes objects other than a black hole. Accretion of matter onto a black hole produces intense radiation. By means of this radiation black holes manifest themselves. In particular, such radiation may contain information about properties of spacetime in the vicinity of a black hole and may confirm that a compact object is really a black hole. (For a comprehensive review of the present status of black holes in astrophysics see, e.g., [19].)

There is both theoretical and observational evidence that magnetic fields play

---

<sup>1</sup> Sagittarius  $A^*$  is a bright and very compact astronomical radio source at the centre of the Milky Way, near the border of the constellations Sagittarius and Scorpius. This compact object is thought to be the location of a supermassive black hole with a mass of around  $4 \times 10^6 M_{\odot}$  and around radius  $12 \times 10^{11}$  cm.

an important role in black hole physics. An example is the explanation of angular momentum transfer in accretion disks where the magnetic field seems to be an essential part of the process [20, 21]. Recent observations of the Faraday rotation of the radiation of a pulsar in the vicinity of a black hole in the centre of the Milky Way (SgrA\*) indicates that at a distance of a few Schwarzschild radii there exist magnetic fields of several hundred Gauss [22]. These observations also support emission models of SgrA\* that require similar magnetic fields for the explanation of the synchrotron radiation from a near-horizon region (see, e.g., [23, 24, 25]).

Guided by observations with the Ginga, ASCA, RXTE and BeppoSAX satellites, astrophysicists agree that X-ray irradiation of the surface layers of the accretion disk in a class of active galactic nuclei gives rise to fluorescent  $K\alpha$  emission line of cold iron. Such line is extremely narrow in frequency, the observed emission spectra of the radiation of the accreting matter are broadened due to special and general relativistic effects. In this thesis, we would like to discuss another interesting aspect of spectral line broadening, namely the use of iron  $K\alpha$  lines (defined in subsection 1.2.2) as probes of the magnetic field in the black hole vicinity. The magnetic field that we take into account, as we explain later in more detail, is not strong enough to modify the background geometry. In our work, we consider a simplified model. Namely, we assume a static, spherical spacetime, i.e., a Schwarzschild black hole, placed in a uniform magnetic field of strength  $B$ . We call this a magnetized Schwarzschild black hole in the sequel.

The thesis is organized as follows:

**Chapter 1:** In the first section of the introduction we discuss the magnetic field around a black hole. In section 1.1, we discuss the theoretical and observational evidence for the existence of magnetic fields around black holes. In subsection 1.1.1,

we describe the spacetime of magnetized black hole. In section 1.2, we discuss the emission spectra, the natural broadening and the definition of the iron  $K\alpha$  lines. In section 1.3, we discuss the main features of line broadening of the narrow Fe  $K\alpha$  spectral line which arises when an iron atom or ion is moving in a gravitational field.

**Chapter 2:** We present the main features of the motion of particles and rays around a magnetized Schwarzschild black hole. We present the main features of the effective potential. We discuss in subsections 2.1.4 and 2.1.5 the main features of stable circular orbits and innermost stable circular orbits, respectively. In section 2.2, we collect the main formulas concerning null ray propagation in the Schwarzschild geometry that will be used later in the thesis. This is done in order to fix notation. In particular, we explain the dimensionless form of the main expressions compatible with the adopted for the particle motion which we discussed earlier.

**Chapter 3:** In this chapter, we discuss imaging the orbits of a charged particle around a weakly magnetized black hole by constructing the map between the equatorial and impact plane. We close section 3.1 by identifying direct and indirect rays. In section 3.2, we study the effect of the magnetic field on spectral broadening. We describe a useful formula for the solid angle for the emitted photons and for the study of the spectral broadening of a single emitter. We do not discuss effects connected with a finite ring of emitters in this thesis, because that would require the choice of a specific model for the size of the disk around the black hole. We close the chapter with a discussion of general properties of the spectral function.

**Chapter 4:** In this chapter, we present our results of the spectral broadening. In particular, we present plots of the spectral function of the emitted radiation

from a charged particle revolving a magnetized Schwarzschild black hole. We close the chapter with a discussion of main features of the spectral function plots.

**Chapter 5:** In this chapter, we sum up the main results and discuss possible applications and generalizations of our work.

This thesis is based on the following published papers: V. P. Frolov, A. A. Shoom and C. Tzounis, “Radiation from an emitter revolving around a magnetized nonrotating black hole,” *Phys. Rev. D* **90**, no. 2, 024027 (2014), and V. P. Frolov, A. A. Shoom and C. Tzounis, “Spectral line broadening in magnetized black holes,” *JCAP* **1407**, 059 (2014) [27, 28]. I was responsible for calculations, confirmation of results, writing and editing the text of the paper. In addition I was responsible for the programming in order to produce the results of the fourth chapter.

During my Ph.D. program I worked on seven papers [27, 28, 29, 30, 31, 32, 33]. In [29], we presented cross-sections for the black hole and string ball production in proton-proton collisions in a TeV-scale gravity model with split fermions in two dimensions. In [30], we introduced the notion of a local shadow for a black hole and determined its shape for the particular case of a distorted Schwarzschild black hole. Considering the lowest-order even and odd multiple moments, we computed the relation between the deformations of the shadow of a Schwarzschild black hole and the distortion multiple moments. In [31], in the simulations of the multi-black holes and merging black holes a larger primary image and a secondary smaller image which looks like an eyebrow and the deformation of the shadows have been observed. However, this kind of eyebrow-like structure was considered as a unique feature of multi black hole systems. In this work, we illustrated the new result that in the case of octupole distortions of a Schwarzschild black hole, the local observer sees two shadows or two images for this single black hole, i.e., also an

eyebrow-like structure. The presence of two images in our case is remarkable, as we studied only one black hole, however, the observer could see two dark images of this single black hole. In [32], we investigated the properties of the ergoregion and the location of the curvature singularities for the Kerr black hole distorted by the gravitational field of external sources. The particular cases of quadrupole and octupole distortions were studied in detail. Also, we investigated the scalar curvature invariants of the horizon and compare their behaviour with the case of the isolated Kerr black hole. In [33], we presented an approximate time-dependent metric in ingoing Eddington-Finkelstein coordinates for an evaporating black hole as a first-order perturbation of the Schwarzschild metric, using the linearized back reaction from a realistic approximation to the stress-energy tensor for the Hawking radiation in the Unruh quantum state.

The subjects I have worked on are rather different, so that I chose only one of them, based on the first two papers, for my thesis.

The most beautiful thing we can experience is the mysterious. It is the source of all true art and science. He to whom the emotion is a stranger, who can no longer pause to wonder and stand wrapped in awe, is as good as dead - his eyes are closed.

Albert Einstein (1879-1955)

*To*  
*My wife and my son*

## Acknowledgements

I am very much thankful to my parents, sisters and brother who have been always a support for me. I overcame difficult times with their love despite the great geographical distance. Special thanks to my parents that they managed to raise me and help me achieve what I was always dreaming despite the financial obstacles.

I am grateful to my supervisor, Professor Valeri P. Frolov. It has been a great privilege to be his student. I am very much grateful to my co-supervisor, Professor Don N. Page, for his advice, support and the opportunity that I had to work with him during my PhD program. I have learnt so many things from him. I want to thank him for his kindness and encouragement. I really thank him for his very interesting lectures. It has been a great privilege and honour to be his student. I would like to thank my master advisor Professor Charis Anastopoulos for his support, kindness and advice. I would like to thank Professor Richard Marchand for his kindness.

I thank the members of the Theoretical Physics Institute, and other colleagues and friends: Professor Robert B. Mann, Professor Elias Vagenas and Dr. Andrei Zel'nikov.

I would like to thank Sandra Hamilton, Carolyn Steinborn, and Dr. Isaac Isaac for their numerous help and support. My especial thanks goes to Sarah Derr for answering all my questions during my Ph.D. program. Moreover, I would like to thank Cathy Page, Phil and Marjie Ebert for all their support and love the last three years.

I do not have words to thank my wife Dr. Shohreh Abdolrahimi and my son.

They are my inspiration and my source of energy to overcome all the difficulties during my program. I would like to thank all my friends in Greece for their support, kindness and love all this years. I want to close this acknowledgement with special thanks to my best friends Alexis Anastasovitis and Dimitris Kakavoulas. We have known each other since school, and they were always encouraging me to go higher.

## Notations and conventions

Here is a list of the notation and conventions that we use throughout the text.

M stands for the mass of the black hole.

B stands for the strength of the magnetic field.

q stands for the charge of a particle.

Q stands for the charge of the black hole.

$\xi$  stands for Killing vectors.

Mass of the sun:  $M_{\odot} = 1.989 \times 10^{33}$  g

Mass of an electron:  $m_e = 9.109 \times 10^{-28}$  g

Mass of a proton:  $m_p = 1.673 \times 10^{-24}$  g

Charge of a proton:  $e = 4.8 \times 10^{-10}(\text{g cm}^3/\text{s}^2)^{1/2}$

Gravitational constant:  $G = 6.674 \times 10^{-8}$  cm<sup>3</sup>/(g s<sup>2</sup>)

Speed of light:  $c = 2.998 \times 10^{10}$  cm/s

Planck's constant:  $h = 6.626 \times 10^{-27}$  cm<sup>2</sup> g/s

Reduced Planck's constant:  $\hbar = 1.055 \times 10^{-27}$  cm<sup>2</sup> g/s

Gravitational radius:  $r_g = 2 M G/c^2$

Maxwell tensor:

$$F_{\mu\nu} = A_{\nu;\mu} - A_{\mu;\nu} \quad (1)$$

where  $A_{\mu}$  is the vector potential.

Partial derivative:

$$A_{\nu;\mu} \equiv \partial_{\mu} A_{\nu} \equiv \frac{\partial A_{\nu}}{\partial x^{\mu}} \quad (2)$$

Covariant derivative:

$$A_{\nu;\mu} \equiv \partial_{\mu}A_{\nu} - \Gamma_{\mu\nu}^{\lambda}A_{\lambda} \quad (3)$$

$$A^{\nu}{}_{;\mu} \equiv \partial_{\mu}A^{\nu} + \Gamma_{\lambda\mu}^{\nu}A^{\lambda} \quad (4)$$

Christoffel symbols:

$$\Gamma_{\beta\gamma}^{\alpha} = \frac{g^{\alpha\mu}}{2} [g_{\mu\beta,\gamma} + g_{\mu\gamma,\beta} - g_{\beta\gamma,\mu}] \quad (5)$$

Riemann curvature tensor:

$$R^{\rho}{}_{\sigma\mu\nu} = \Gamma^{\rho}{}_{\nu\sigma,\mu} - \Gamma^{\rho}{}_{\mu\sigma,\nu} + \Gamma^{\rho}{}_{\mu\lambda}\Gamma^{\lambda}{}_{\nu\sigma} - \Gamma^{\rho}{}_{\nu\lambda}\Gamma^{\lambda}{}_{\mu\sigma} \quad (6)$$

or

$$R_{\rho\sigma\mu\nu} = \frac{1}{2} (g_{\rho\nu,\sigma\mu} + g_{\sigma\mu,\rho\nu} - g_{\rho\mu,\sigma\nu} - g_{\sigma\nu,\rho\mu}) + g_{\alpha\beta} (\Gamma^{\alpha}{}_{\sigma\mu}\Gamma^{\beta}{}_{\rho\nu} - \Gamma^{\alpha}{}_{\sigma\nu}\Gamma^{\beta}{}_{\rho\mu}) \quad (7)$$

Ricci curvature tensor:

$$\begin{aligned} R_{\alpha\beta} = R^{\rho}{}_{\alpha\rho\beta} &= \Gamma^{\rho}{}_{\beta\alpha,\rho} - \Gamma^{\rho}{}_{\rho\alpha,\beta} + \Gamma^{\rho}{}_{\rho\lambda}\Gamma^{\lambda}{}_{\beta\alpha} - \Gamma^{\rho}{}_{\beta\lambda}\Gamma^{\lambda}{}_{\rho\alpha} \\ &= 2\Gamma^{\rho}{}_{\alpha[\beta,\rho]} + 2\Gamma^{\rho}{}_{\lambda[\rho}\Gamma^{\lambda}{}_{\beta]\alpha} \end{aligned} \quad (8)$$

For any two vectors  $p^{\mu}$  and  $q^{\mu}$ ,

$$(\mathbf{p}, \mathbf{q}) \equiv p_{\mu}q^{\mu}. \quad (9)$$

# Table of Contents

<b>1</b>	<b>Introduction</b>	<b>1</b>
1.1	Magnetized black holes . . . . .	1
1.1.1	Weakly magnetized black holes . . . . .	9
1.2	Emission spectra . . . . .	13
1.2.1	Natural broadening . . . . .	16
1.2.2	Fe $K\alpha$ spectral lines . . . . .	19
1.3	Features of the line broadening . . . . .	20
1.3.1	Newtonian case . . . . .	21
1.3.2	Emission from a ring of finite width . . . . .	24
1.3.3	Relativistic case . . . . .	28
<b>2</b>	<b>Motion of charged particles and null rays</b>	<b>35</b>
2.1	Charged particle . . . . .	36
2.1.1	Effective potential . . . . .	40
2.1.2	Stable circular orbits (SCO's) . . . . .	49
2.1.3	Innermost stable circular orbits (ISCO's) . . . . .	52
2.1.4	Circular motion in the rest frame basis . . . . .	58
2.2	Null rays in the Schwarzschild geometry . . . . .	59
2.2.1	Conserved quantities and equations of motion . . . . .	59
2.2.2	Motion in the equatorial plane . . . . .	60
2.2.3	Integrals of motion and impact parameters . . . . .	62
2.2.4	Asymptotic data for null rays . . . . .	65
<b>3</b>	<b>Imaging the radiation</b>	<b>67</b>
3.1	Orbit images . . . . .	68
3.1.1	Angular relations . . . . .	68
3.1.2	Map between equatorial and impact planes . . . . .	71
3.1.3	Direct and indirect rays . . . . .	75
3.2	Spectral broadening . . . . .	82
3.2.1	Photon momentum and conserved quantities . . . . .	82
3.2.2	Photon beam from the emitter . . . . .	83

TABLE OF CONTENTS

xv

3.2.3	Solid angle at the emitter . . . . .	84
3.2.4	Spectral broadening . . . . .	86
3.2.5	General properties of spectral functions . . . . .	90
<b>4</b>	<b>Spectral function plots and common features</b>	<b>94</b>
<b>5</b>	<b>Conclusion</b>	<b>105</b>
<b>A</b>	<b><math>\ell</math>-parametrization of the orbit</b>	<b>124</b>
<b>B</b>	<b>Radiation from a point-like source</b>	<b>127</b>
<b>C</b>	<b>Small oscillations</b>	<b>130</b>
<b>D</b>	<b>Time of a charged particle on a circular orbit</b>	<b>134</b>
<b>E</b>	<b>Charge accretion</b>	<b>138</b>

# List of Figures

1.1	The black curve (1) shows the spectral line which is not affected by natural broadening. The red curve (2) represents a spectral line with large lifetime, due to natural broadening in comparison to the lifetime of the black curve. . . . .	18
1.2	The profile of the Fe $K\alpha$ line from Seyfert 1 galaxy MCG-6-30-15 observed by ASCA SIS detector. The figure is taken from [74]. . .	20
1.3	The modified spectrum as a function of the ratio of the frequencies due to the non-relativistic Doppler effect. Here, $v_{\max} = 0.1c$ , and the dimensionless radius of the emitter is $\rho = 2000$ . . . . .	24
1.4	The modified spectrum of a disk as a function of the ratio of the frequencies due to the non-relativistic Doppler effect. . . . .	27
1.5	The modified spectrum of a disk as a function of the ratio of the frequencies due to the non-relativistic Doppler effect. The black curve is the spectrum of a disk with $\rho_{in} = 2000$ and $\rho_{out} = 7000$ . The blue curve is the spectrum of a disk with $\rho_{in} = 2000$ and $\rho_{out} = 5000$ . The red curve is the spectrum of a disk with $\rho_{in} = 2000$ and $\rho_{out} = 3000$ . . . . .	28
1.6	The modified spectrum of a disk as a function of the ratio of the frequencies due to the non-relativistic Doppler effect. The black curve is the spectrum of a disk with $\rho_{in} = 2000$ and $\rho_{out} = 7000$ . The blue curve is the spectrum of a disk with $\rho_{in} = 3000$ and $\rho_{out} = 7000$ . The red curve is the spectrum of a disk with $\rho_{in} = 4000$ and $\rho_{out} = 7000$ . . . . .	29
1.7	Geometry of the rays in the flat spacetime. At the points 1 and 2 the angle $\Phi$ is $90^\circ$ . . . . .	31
1.8	Spectrum in the relativistic case. . . . .	33
2.1	The effective potential for $b = 0.5$ and $l = 1.18$ . . . . .	40
2.2	The effective potential for $b = 0.5$ and $l = 2.07$ . . . . .	41
2.3	The effective potential for $b = 0.5$ and $l = 3.22$ . . . . .	42

2.4 Type of a bounded trajectory with curls. Arrows illustrate the direction of motion of a charged particle. . . . . 44

2.5 Limiting case of bounded trajectory with curls. Arrows illustrate the direction of motion of a charged particle. . . . . 45

2.6 Type of a bounded trajectory without curls. Arrows illustrate the direction of motion of a charged particle. . . . . 46

2.7 Angular velocity,  $\Omega$ , as a function of the radius,  $\rho$ , for different values of magnetic field,  $b$  for anti-Lamor particles. The dark red curve has  $b = 0$ , the blue curve has  $b = 0.25$ , the black curve has  $b = 1$ , the red curve has  $b = 3$ , and the green curve has  $b = 5$ . . . . . 50

2.8 Angular velocity  $\Omega$  as a function of the radius,  $\rho$ , for different values of magnetic field,  $b$  for Lamor particles. The dark red curve has  $b = 0$ , the blue curve has  $b = 0.05$ , the black curve has  $b = 0.1$ , the red curve has  $b = 0.25$ , and the green curve has  $b = 1$ . . . . . 51

2.9 Magnetic field  $b$  of a magnetized black hole as a function of the ISCO radius  $\rho$ . Labels + and - stand for the anti-Larmor and Larmor orbit branches, respectively. . . . . 53

2.10 Specific energy  $\mathcal{E}$  of a charged particle at ISCO in a magnetized black hole as a function of the ISCO radius  $\rho$ . Labels + and - stand for the anti-Larmor and Larmor orbit branches, respectively. . . . . 54

2.11 Angular velocity  $|\Omega|$  as a function of the ISCO radius in a magnetized black hole. Labels + and - stand for the anti-Larmor and Larmor orbit branches, respectively. . . . . 55

2.12 Velocity  $v$  of a charged particle at the ISCO in a magnetized black hole as a function of the ISCO radius  $\rho$ . Labels + and - stand for the anti-Larmor and Larmor orbit branches, respectively. . . . . 56

2.13 Motion of a photon in the equatorial plane. The photon emitted at  $P_e$  propagates to a distant observer along a trajectory without radial turning points (a direct ray). The ray emitted at  $P'_e$  is indirect. It at first moves toward the black hole, and only after it passes through a radial turning point does it propagate outward to the distant observer. The image is from [27] . . . . . 63

3.1 Angular definitions. The image is from [27] . . . . . 69

3.2 Schematic diagram of the impact plane. The horizontal axis corresponds to the  $\phi$  coordinate and the vertical axis corresponds to the  $\theta$  coordinate. The image does not distinguish between the domain *III* and *IV*. The image is from [27] . . . . . 73

3.3 The boundary  $\Gamma$  between the regions *I* and *II* for different values of the observer's angle  $\theta_o$ : Curve 1:  $\theta_o = 5^\circ$ ; Curve 2:  $\theta_o = 45^\circ$ ; Curve 3:  $\theta_o = 85^\circ$ . A great circle is a curve  $|\xi| = \ell_* = 3\sqrt{3}/2$ . . . . . 74

3.4 Function  $C(z)$ . It monotonically grows with  $z$  from  $\pi/2$  at  $z = 0$  and becomes infinite at  $z = 2/3$ . . . . . 77

3.5 The critical inverse radius  $\zeta_*$  as a function of the inclination angle  $\theta_o$ . 78

3.6 Images of some orbits corresponding to  $\theta_o = 85^\circ$ . The innermost curve is the image of the  $\zeta_e = 5/6$  orbit. The next curve is the image of the  $\zeta_e = 2/3$  orbit. And the outermost curve is the image of the  $\zeta_e = 1/3$  orbit. The circle represents the rim of the black hole shadow. Note that the angle  $\theta_o$  is increasing from the axis of the black hole to the equatorial plane. . . . . 79

3.7 Image corresponds to  $\theta_o = 5^\circ$ . The inner circle represents the rim of the black hole shadow. The outer circle is the image of the  $\zeta_e = 1/3$  orbit. . . . . 80

3.8 Image corresponds to  $\theta_o = 5^\circ$ . The outer circle represents the rim of the black hole shadow. The inner circle is the image of the  $\zeta_e = 5/6$  orbit. . . . . 80

3.9 Image corresponds to  $\theta_o = 45^\circ$ . The circle represents the rim of the black hole shadow. The deformed curve is the image of the  $\zeta_e = 1/3$  orbit. . . . . 81

3.10 Image corresponds to  $\theta_o = 45^\circ$ . The circle represents the rim of the black hole shadow. The deformed curve is the image of the  $\zeta_e = 5/6$  orbit. . . . . 81

3.11 Diagram illustrating orbit of the emitter. The arrows show the direction of the emitter's motion ( $\Omega > 0$ ). For the emitter located in the right semicircle,  $\varphi \in [0, \pi]$ , photons have Doppler redshift, and for the emitter located in the left semicircle,  $\varphi \in (-\pi, 0]$ , photons have Doppler blueshift. The spectral function diverges at  $\varphi = \varphi_m$  and  $\varphi = -\varphi_m$ , where  $|\varphi_m| > \pi/2$ . The portion of the orbit corresponding to indirect null rays is defined by the angle  $|\varphi| > \varphi_*$ . There is a nonzero Doppler shift at  $\varphi = 0$  and  $\varphi = \pm\pi$ ; it is with respect to this Doppler shift that we define which photons are redshifted and blueshifted. . . . . 91

4.1 Spectral function for the anti-Larmor ISCO,  $b = 0$ , at  $\zeta_e = 1/3$ . The inclination angle is  $\theta_o = 30^\circ$ . The angular velocity of the emitter is  $\Omega = 0.136$ , and its specific energy is  $\mathcal{E} = 0.943$ . The spectrum has peaks at  $w_- = 0.571$  ( $\varphi_m = 97^\circ 85'$ ) and at  $w_+ = 0.928$  (at  $-\varphi_m$ ). The minimal values (0.290 and 0.370) of  $n_w$  for the two spectral branches are at  $w_0 = 0.707$ . The width parameter is  $\Delta = 0.476$ , and the asymmetry parameter is  $\delta = 0.236$ . One also has  $N_o = 0.285$ . . . . . 96

- 4.2 Spectral function for the anti-Larmor ISCO,  $b = 0$ , at  $\zeta_e = 1/3$ . The inclination angle is  $\theta_o = 60^\circ$ . The angular velocity of the emitter is  $\Omega = 0.136$ , and its specific energy is  $\mathcal{E} = 0.943$ . The spectrum has peaks at  $w_- = 0.497$  ( $\varphi_m = 107^\circ 9'$ ) and at  $w_+ = 1.224$  (at  $-\varphi_m$ ). The minimal values (0.127 and 0.222) of  $n_w$  for two spectral branches are at  $w_0 = 0.707$ . The width parameter is  $\Delta = 0.845$ , and the asymmetry parameter is  $\delta = 0.423$ . One also has  $N_o = 0.356$ . . 97
- 4.3 Spectral function for the anti-Larmor ISCO,  $b = 0$ , at  $\zeta_e = 1/3$ . The inclination angle is  $\theta_o = 85^\circ$ . The angular velocity of the emitter is  $\Omega = 0.136$ , and its specific energy is  $\mathcal{E} = 0.943$ . The spectrum has peaks at  $w_- = 0.472$  ( $\varphi_m = 118^\circ 4'$ ) and at  $w_+ = 1.407$  (at  $-\varphi_m$ ). The minimal values (0.079 and 0.196) of  $n_w$  for two spectral branches are at  $w_0 = 0.707$ . The width parameter is  $\Delta = 0.995$ , and the asymmetry parameter is  $\delta = 0.498$ . One also has  $N_o = 0.397$ . 98
- 4.4 Spectral function for the anti-Larmor ISCO,  $b = 2.251$ , at  $\zeta_e = 5/6$ . The inclination angle is  $\theta_o = 30^\circ$ . The angular velocity of the emitter is  $\Omega = 0.162$ , and its specific energy is  $\mathcal{E} = 0.465$ . The spectrum has peaks at  $w_- = 0.315$  ( $\varphi_m = 104^\circ 7'$ ) and at  $w_+ = 0.415$  (at  $-\varphi_m$ ). The minimal values (0.128 and 0.186) of  $n_w$  for two spectral branches are at  $w_0 = 0.358$ . The width parameter is  $\Delta = 0.274$ , and the asymmetry parameter is  $\delta = 0.137$ . One also has  $N_o = 0.050$ . . 99
- 4.5 Spectral function for the anti-Larmor ISCO,  $b = 2.251$ , at  $\zeta_e = 5/6$ . The inclination angle is  $\theta_o = 60^\circ$ . The angular velocity of the emitter is  $\Omega = 0.162$ , and its specific energy is  $\mathcal{E} = 0.465$ . The spectrum has peaks at  $w_- = 0.284$  ( $\varphi_m = 124^\circ 6'$ ) and at  $w_+ = 0.486$  (at  $-\varphi_m$ ). The minimal values (0.055 and 0.117) of  $n_w$  for two spectral branches are at  $w_0 = 0.358$ . The width parameter is  $\Delta = 0.525$ , and the asymmetry parameter is  $\delta = 0.262$ . One also has  $N_o = 0.058$ .100
- 4.6 Spectral function for the anti-Larmor ISCO,  $b = 2.251$ , at  $\zeta_e = 5/6$ . The inclination angle is  $\theta_o = 85^\circ$ . The angular velocity of the emitter is  $\Omega = 0.162$ , and its specific energy is  $\mathcal{E} = 0.465$ . The spectrum has peaks at  $w_- = 0.264$  ( $\varphi_m = 158^\circ 6'$ ) and at  $w_+ = 0.558$  (at  $-\varphi_m$ ). The minimal values (0.036 and 0.105) of  $n_w$  for two spectral branches are at  $w_0 = 0.358$ . The width parameter is  $\Delta = 0.714$ , and the asymmetry parameter is  $\delta = 0.357$ . One also has  $N_o = 0.085$ .101

- 4.7 Spectral function for an anti-Larmor SCO,  $b = 2.251$ , at  $\zeta_e = 1/3$ . The inclination angle is  $\theta_o = 30^\circ$ . The angular velocity of the emitter is  $\Omega = 0.005$ , and its specific energy is  $\mathcal{E} = 0.817$ . The spectrum has peaks at  $w_- = 0.809$  ( $\varphi_m = 97^\circ 85'$ ) and at  $w_+ = 0.823$  (at  $-\varphi_m$ ). The minimal values (10.46 and 13.35) of  $n_w$  for two spectral branches are at  $w_0 = 0.816$ . The width parameter is  $\Delta = 0.018$ , and the asymmetry parameter is  $\delta = 0.009$ . One also has  $N_o = 0.390$ . 102
- 4.8 Spectral function for an anti-Larmor SCO,  $b = 2.251$ , at  $\zeta_e = 1/3$ . The inclination angle is  $\theta_o = 60^\circ$ . The angular velocity of the emitter is  $\Omega = 0.005$ , and its specific energy is  $\mathcal{E} = 0.817$ . The spectrum has peaks at  $w_- = 0.804$  ( $\varphi_m = 107^\circ 9'$ ) and at  $w_+ = 0.829$  (at  $-\varphi_m$ ). The minimal values (4.578 and 8.018) of  $n_w$  for two spectral branches are at  $w_0 = 0.816$ . The width parameter is  $\Delta = 0.031$ , and the asymmetry parameter is  $\delta = 0.016$ . One also has  $N_o = 0.382$ . 103
- 4.9 Spectral function for an anti-Larmor SCO,  $b = 2.251$ , at  $\zeta_e = 1/3$ . The inclination angle is  $\theta_o = 85^\circ$ . The angular velocity of the emitter is  $\Omega = 0.005$ , and its specific energy is  $\mathcal{E} = 0.817$ . The spectrum has peaks at  $w_- = 0.802$  ( $\varphi_m = 118^\circ 4'$ ) and at  $w_+ = 0.832$  (at  $-\varphi_m$ ). The minimal values (2.836 and 7.051) of  $n_w$  for two spectral branches are at  $w_0 = 0.816$ . The width parameter is  $\Delta = 0.037$ , and the asymmetry parameter is  $\delta = 0.019$ . One also has  $N_o = 0.388$ . . 104

# Chapter 1

## Introduction

### 1.1 Magnetized black holes

Magnetic fields play an important role in black hole physics. In the presence of a magnetic field, the motion of plasma and charged particles is modified. In this thesis we study the action of a magnetic field in the vicinity of a black hole on charged particle bound orbits. The main effect is that the position of the innermost stable circular orbit (ISCO) can be closer than for an uncharged particle. This observation opens an interesting opportunity for the study of a regular magnetic field near a black hole by observing the radiation emitted by charged particle motion around the black hole.

In this chapter, first we discuss magnetic fields around a black hole. In Section 1, we start with theoretical and observational evidence concerning the existence of magnetic fields around astrophysical black holes and describe several models of a weakly magnetized black hole which were studied earlier. In Section 2, we discuss the effect of spectral line broadening of the emitted radiation from the matter

accreting onto the black hole. This method, namely usage of iron  $K\alpha$  lines, is often used for the study of the motion of matter near compact objects. We briefly describe the natural broadening of the spectral lines and explain why one of the Fe  $K\alpha$  spectral lines plays such an important role in astrophysics. In the last section of the introduction, we discuss the main features of the line broadening.

A black hole can be magnetized by large-scale magnetic fields. However, these fields are negligibly small. The strength of such magnetic fields ranges from 0.1 to  $10^2 \mu\text{G}$ . Evidence for the observed large-scale magnetic field in the galactic and intergalactic media is presented in [34]. The large-scale magnetic fields have mainly cosmological implications. There are several more efficient mechanisms which may “magnetize” a black hole. For example, a black hole can be magnetized by a companion magnetar<sup>1</sup>. Black hole-neutron star binaries are studied in [35]. Black holes can also be magnetized by plasma motion in their own accretion disks [36, 37]. Actually, such magnetic fields are the most significant magnetic fields in the study of black hole physics.

Magnetic fields are important in black hole astrophysics for explaining the synchrotron radiation from the region of spacetime near the horizon region, the interaction of the black hole with the disk, the power of the winds in the disk, the black hole jets energetics and the formation of relativistic jets. Furthermore, observations show that winds in the disk of stellar mass black hole are powered by

---

<sup>1</sup> A magnetar is a class of neutron star with powerful magnetic field  $10^8$  to  $10^{11}$  tesla. Such a magnetic field powers the emission of X-rays and gamma rays. Magnetars are the most powerful magnetic objects detected throughout the universe. Their magnetic fields result from a magnetohydrodynamic dynamo process in the turbulent, very dense conducting fluid that exists before the neutron star settles into its equilibrium state. Then, such fields continue to exist because of persistent currents in a proton-superconductor phase of matter that exists between the core and the surface of the neutron star. A similar process produces extremely intense transient fields during the coalescence of neutron stars binaries [38, 39, 40].

the pressure due to magnetic viscosity [41].

In the Blandford-Znajek model [42] a regular magnetic field in the vicinity of a black hole is often used to explain black hole jets energetics [43, 42, 47]. For example, in order to produce power of the magnitude  $\sim 10^{45}$  erg/sec seen in the jets of supermassive (with mass  $10^9 M_\odot$ ) rotating black holes, regular magnetic fields of the order of  $10^4$  G are required [47]. In [43], it was shown that it is possible for a magnetic field to hold plasma stationary and stable at some radius,

$$r_0 = r_g(1 + \epsilon), \quad (1.1)$$

where  $0 < \epsilon \ll 1$  and  $r_g = 2MG/c^2$  is the gravitational radius. According to [43], this can be achieved with a regular and large magnetic field. However such a magnetic field is not large enough to modify the black hole geometry. Another mechanism proposed for explaining the energy extraction from a rotating black hole and the formation of relativistic jet is based on the analogue of the Penrose mechanism for a magnetic field. It was proposed in [44, 45, 46]. The authors performed numerical simulations and demonstrated that the power in the jet emission as a result of such a magnetohydrodynamic (MHD) Penrose process is of the same order as the one estimated based on the Blandford-Znajek mechanism. In particular, for a strong magnetic field  $\sim 10^{15}$  G around a stellar-mass ( $M \sim 10M_\odot$ ) extreme rotating black hole, the power of emission is estimated as  $\sim 4 \times 10^{52}$  erg/sec, which is similar to the power seen in gamma-ray bursts. Estimates based on the observed optical polarization for a number of active galactic nuclei give values  $\sim 10^3 - 10^5$  G for the magnetic field at the horizon of the corresponding black holes [48, 49, 50].

Faraday rotation<sup>1</sup> is a method of observing and estimating the magnetic field around a black hole. The recent measurements of multi-frequency radio emission of a pulsar in  $\sim 3''$  angular proximity to the centre of our galaxy [51, 52, 53, 54] reported in [22] show an unusually large Faraday rotation. According to [22, 54, 55, 56] the value of the rotation measure is

$$RM = (-6.696 \pm 0.005) \times 10^4 \text{ rad m}^{-2}. \quad (1.2)$$

According to [57] the actual value of  $RM$  is closer to  $-5 \times 10^5 \text{ rad m}^{-2}$ . This rotation measure<sup>2</sup> ( $RM$ ) is the largest measured for any object in our galaxy other than the supermassive black hole in the centre of it [58, 59]. Moreover, this value is more than ten times larger than all the other rotation measures observed within several parsec of Sgr A\* [60].

This large value of the rotation measure limits the location of the magnetized gas causing the Faraday rotation to be within some ten parsecs from the centre of Milky Way. A robust estimation gives the magnetic field to be  $B \geq 50 \mu\text{G}$  [54]. However, based on the estimation of [22] for  $r = 0.12$  parsec or  $3 \times 10^5$

---

<sup>1</sup>The rotation of the plane of polarization during propagation through plasma in an external magnetic field. The angle of the rotation of the plane is given by

$$\Delta\phi = RM \lambda^2,$$

where  $RM$  is the rotation measure and  $\lambda$  is the wavelength of the light.

<sup>2</sup> Interstellar Faraday rotation depends on the wavelength of light and the RM, the rotation measure. The overall strength of the effect is characterized by RM, the rotation measure. This depends on the projection of the interstellar magnetic field on the line of sight, and the number density of electrons  $n(s)$ , both of which may vary along the propagation path,

$$RM = \frac{e^3}{2\pi m_e^2 c^4} \int n(\vec{x}) \vec{B}(\vec{x}) \cdot d\vec{x} = \frac{e^3}{2\pi m_e^2 c^4} \int B(s) n(s) ds, \quad (1.3)$$

where  $e$  is the charge of the electron,  $m_e$  is the mass of the electron,  $c$  is the speed of light, and  $B(s)$  is the projection of the magnetic field along the line of sight.

Schwarzschild radii, the magnetic field is  $B \sim 2.6$  mG. Taking into account that  $B \propto r^{-1}$ , one should expect that at a few Schwarzschild radii from the event horizon the magnetic field would be several hundred gauss. This supports emission models of SgrA\* that require similar magnetic fields for the explanation of the synchrotron radiation from a near horizon region (see, e.g., [23, 24, 25]).

Magnetized black holes have been studied theoretically in various papers. For a black hole drifting in an arbitrary direction with respect to a uniform magnetic field in any orientation, see [62]. A Kerr black hole in a tilted uniform “test” magnetic field was found in [63] with the help of the Newman-Penrose formalism. A mechanism of creating a weak magnetic field around a black hole was studied in [95]. The magnetic field is produced by an axisymmetric current loop around a Schwarzschild black hole. Moreover, the dipole part was studied as well in [95]. A more general case which includes eccentric symmetric current loops was studied in [64]. The geometry in [64] is Kerr. Another generalization for the extreme Reissner-Nordstrom black hole was conducted in [65].

In our work, we consider how a regular magnetic field in the vicinity of a black hole changes the parameters of the charged particle orbits. We use a simplified model. Namely, we assume that the black hole is not rotating and the magnetic field is static, axisymmetric and homogeneous at infinity. Our aim is to obtain the images of such orbits as they are seen by a distant observer. We also study the effect of the broadened spectrum of the emission lines of iron ions moving near magnetized black holes. Let us mention that the influence of a magnetic field on the distortion of the iron  $K\alpha$  line profile was earlier discussed in [66]. The authors focused on the splitting of lines of emission due to the Zeeman effect. They demonstrated that this effect might be important if the magnetic field is of

the order of  $10^{10} - 10^{11}$  G. We consider the modification of the orbits of charged particles, which might exist at much weaker magnetic fields. Namely, we assume that an iron ion, emitting radiation, revolves around a magnetized black hole. The Lorentz force, acting on a moving charged emitter in the magnetic field, modifies its motion.

A question that naturally arises here and is also relevant to the next two subsections is the following: Is the magnetic field that modifies the orbits of the charged particles enough to cause any back-reaction to the spacetime? The space-time local curvature created by the magnetic field  $B$  is of the order of magnitude  $GB^2/c^4$ . This value of magnetic field is comparable to the spacetime curvature near a black hole of mass  $M$  only if

$$\frac{GB^2}{c^4} \sim \frac{1}{r_g^2} \sim \frac{c^4}{G^2 M^2}. \quad (1.4)$$

This yields,

$$B \sim B_M = \frac{c^4}{G^{2/3} M_\odot} \left( \frac{M_\odot}{M} \right) \sim 10^{19} \left( \frac{M_\odot}{M} \right) G \quad (1.5)$$

In our study the magnetic field  $B$  is much smaller than the field in (1.5), so the field  $B$  will be considered as a “test” field in the given gravitational background. Such a magnetic field does not effect the motion of neutral particles if we ignore the effect of an inhomogeneous magnetic field on a neutral particle with a magnetic moment. On the other hand, the acceleration induced in the motion of charged particles by the Lorentz force can be large [68]. Here we are going to show that for astrophysical black holes this can happen.

One of the effects of the magnetic field can be seen by the analysis of the equations of motion of charged particles. The position of the ISCO for charged

particles is closer to the black hole horizon than the ISCO radius for a neutral particle ( $6M$ ) [67, 68]. This modification of the orbit is more profound in the case when the Lorentz force is repulsive. The modification of the orbits is characterized by the dimensionless parameter (in the CGS system of units)

$$b = \frac{qBMG}{mc^4}. \quad (1.6)$$

Here  $q$  and  $m$  are charge and mass of the charged particle,  $B$  is the strength of the magnetic field, and  $M$  is the mass of the black hole. (Here we use the CGS system of units.) The parameter  $b$  is proportional to the ratio of the cyclotron frequency of a charged particle in the magnetic field  $B$  in the absence of gravity, to the Keplerian frequency of a neutral particle of the same mass  $m$  at the ISCO in the gravitational field of the black hole. To estimate the value of this parameter one can consider the motion of a proton (mass  $m_p = 1.67 \times 10^{-24}$ g and charge  $e = 4.8 \times 10^{-10}$ (g cm<sup>3</sup>/sec<sup>2</sup>)<sup>1/2</sup>). Then for a stellar mass black hole,  $M = 10M_\odot$ , this parameter takes the value  $b = 1$  for the magnetic field  $B \sim 2$  G. For a supermassive black hole  $M \sim 10^9 M_\odot$ , if  $b = 1$  the corresponding field is  $B \sim 2 \times 10^{-8}$  G. If the charge of the ion is  $q = Ze$  and its mass is  $m = Am_p$  the corresponding expression for the magnetic field parameter  $b$  contains an additional factor  $Z/A$ . One can expect that for astrophysical black holes where the magnetic field can be hundreds of Gauss, the parameter  $b$  is large. Therefore, the acceleration induced in the motion of charged particles by the Lorentz force can be large in comparison with the gravitational force.

As we will see later in detail, the magnetic field essentially modifies the orbits already when the parameter  $b$  is of the order of 1. For the repulsive Lorentz force

case, the radius of ISCO in the strong magnetic field ( $b \gg 1$ ) can be located arbitrary close to the horizon. Thus, two new effects are present in the motion of charged particles in magnetized black holes:

1. The position of the ISCO depends on the magnetic field.
2. Even for a circular motion of the same radius, the angular velocity of a charged particle differs from the Keplerian angular velocity.

In particular, we can say that with the increase of the magnetic field, the orbital frequency tends to zero and the ISCO is approaching the horizon of the black hole, in the case that the rotation direction induces a repulsive magnetic force.

The consequences of the new effects in the motion of charged particles, due to the magnetic field as we mentioned above, can be observed in the emission spectrum. The results show that the spectrum has the following features,

1. The existence of two sharp peaks at the extrema of the frequencies due to the Doppler effect.
2. The existence of two branches of the spectrum.
3. The increase of the average redshift of the spectral frequencies for the ISCO with the increase of the magnetic field.
4. The narrowing of the frequency bands with the increase of the magnetic field.
5. The asymmetry of the spectrum with respect to the spectral average frequency. (This is a generic feature as we will see in the relativistic case.)

### 1.1.1 Weakly magnetized black holes

As we mentioned before, in our study we do not consider back-reaction from the magnetic field on the metric. In other words, we are considering a weak field approximation. A special simple solution for a test magnetic field was found by Robert Wald in 1974. In his work, a rotating black hole is immersed in a weak “test” field. The magnetic field is uniform and aligned along the axis of symmetry of the black hole. As we will see, by using linear combinations of the Killing vectors (i.e., use them as the 4-vector potential for the electromagnetic field) of the spacetime of interest (which is Ricci flat,  $R_{\mu\nu} = 0$ ), we get solutions to the Maxwell equations [72]<sup>1</sup>.

Here we will follow the calculations of [72]. A Killing vector,  $\xi_{(\nu)}^\mu$ , in a vacuum spacetime generates a solution of Maxwell’s equations in that spacetime [73]. Here we will use  $G = c = 1$ . If we have

$$F_{\mu\nu} = \xi_{\nu;\mu} - \xi_{\mu;\nu}, \quad (1.7)$$

then the source free Maxwell’s equations are satisfied,

$$F^{\mu\nu}{}_{;\nu} = -2\xi^{\mu;\nu}{}_{;\nu} = 0. \quad (1.8)$$

This can be proven in two steps. In the first step, we use the definition of the

---

<sup>1</sup>The spacetime in [72] is a Kerr spacetime; therefore the rotation of the black hole induces electric fields near the horizon. The black hole will accrete charges until its charge reaches  $Q = 2BJ$  (here we consider  $G = c = 1$ ) because of the electric potential difference between horizon and the infinity. Here,  $Q$  is the charge that black hole accretes,  $B$  is the strength of the magnetic field, and  $J$  is the angular momentum of the Kerr spacetime.

Riemann tensor,

$$\xi_{\mu;\nu;\kappa} - \xi_{\mu;\kappa;\nu} = -\xi^\lambda R_{\lambda\mu\nu\kappa}, \quad (1.9)$$

the Killing equation

$$\xi_{\mu;\nu} + \xi_{\nu;\mu} = 0, \quad (1.10)$$

and the properties of the cyclical permutations of the indices  $\mu, \nu, \kappa$ . In particular we have,

$$\begin{aligned} & \xi_{\mu;\nu;\kappa} - \xi_{\mu;\kappa;\nu} + \xi_{\nu;\kappa;\mu} - \xi_{\nu;\mu;\kappa} + \xi_{\kappa;\mu;\nu} - \xi_{\kappa;\nu;\mu} \\ = & -\frac{1}{6}\xi^\lambda (R_{\lambda\mu\nu\kappa} + R_{\lambda\nu\kappa\mu} + R_{\lambda\kappa\mu\nu}) \\ = & 0. \end{aligned} \quad (1.11)$$

Here we use the Killing equation in order to get

$$\xi_{\mu;\nu;\kappa} + (\xi_{\kappa;\mu;\nu} - \xi_{\kappa;\nu;\mu}) = 0 \quad (1.12)$$

Then one finds that the Killing vectors satisfy

$$\xi_{\mu;\nu;\kappa} = \xi^\lambda R_{\lambda\kappa\mu\nu}. \quad (1.13)$$

In the second step, we contract the indices  $\nu$  and  $\kappa$  so that

$$\xi^{\mu;\nu}{}_{;\nu} = \xi^\lambda R^\mu{}_\lambda. \quad (1.14)$$

In the spacetime of interest, which is vacuum, the Ricci tensor is zero, so one obtains equation (1.8). For more details, see [72].

In flat spacetime there are ten independent Killing vector fields.

1. Three boost Killing vectors. These vectors generate uniform electric fields.
2. Three rotational Killing vectors. These vectors generate uniform magnetic fields.
3. Four translation Killing vectors. The electromagnetic field generated by such Killing vectors vanishes.

If the spacetime is static and axisymmetric, that is, it has time translation and axial Killing vectors, then the vector potential can be written as

$$A^\mu = \alpha \xi_{(t)}^\mu + \beta \xi_{(\phi)}^\mu. \quad (1.15)$$

The constants  $\alpha$  and  $\beta$  are determined by the properties of the Maxwell tensor and Gauss law (see [72]). In order to obtain the solution for the electromagnetic test field which occurs when a stationary, axisymmetric black hole is placed in a uniform magnetic field of strength  $B$  aligned along the symmetry axis of the black hole,  $F_{\mu\nu}$  must satisfy the following properties:

1.  $F_{\mu\nu}$  is stationary and axisymmetric.
2.  $F_{\mu\nu}$  is nonsingular in the exterior region and on the horizon of the black hole.
3.  $F_{\mu\nu}$ , at large distances, must asymptotically approach the Faraday tensor of a uniform magnetic field of strength  $B$ .
4.  $F_{\mu\nu}$  has no charge or magnetic monopole moment.

For a Schwarzschild spacetime that is magnetized and has charge  $Q = 0$ , the first two properties of the Maxwell tensor imply that  $\alpha$  and  $\beta$  must be constants. Calculating the invariant quantity  $(1/2)F^{\mu\nu}F_{\mu\nu}$  at infinity, we get  $B^2 - \tilde{\epsilon}^2$  where  $\tilde{\epsilon}$  denotes the strength of the electric field. However, if  $\tilde{\epsilon} = 0$  we have,

$$\frac{1}{2}F^{\mu\nu}F_{\mu\nu} = B^2. \quad (1.16)$$

In our case we have,

$$\frac{1}{2}F^{\mu\nu}F_{\mu\nu} = 4\beta^2 \frac{r - 2M \sin^2 \theta}{r}. \quad (1.17)$$

Therefore, the third property of the Maxwell tensor implies that  $\beta = B/2$ . Using the Gauss law,

$$\int_{\Sigma} F^{\mu\nu} d^2\Sigma_{\mu\nu} = 4\pi Q, \quad (1.18)$$

we can calculate what should be the value of the constant  $\alpha$ . Here  $Q$  is the charge of the black hole, and  $\Sigma$  is a 2-dimensional surface element surrounding the black hole,

$$d^2\Sigma_{\mu\nu} = \frac{\sqrt{-g}}{2} \epsilon_{\mu\nu\lambda\sigma} dx^\lambda \wedge dx^\sigma, \quad (1.19)$$

where  $g$  is the determinant of the Schwarzschild metric and  $\epsilon_{\mu\nu\lambda\sigma}$  is the Levi-Civita symbol with  $\epsilon_{tr\theta\phi} = 1$ . Equation (1.18) gives

$$8\pi\alpha M = 4\pi Q. \quad (1.20)$$

For  $Q = 0$ , the constant  $\alpha$  must be zero, so for the vector potential we have

$$A^\mu = \frac{B}{2} \xi_{(\phi)}^\mu. \quad (1.21)$$

In the next chapter, we study charged-particle motion around a weakly magnetized Schwarzschild black hole.

## 1.2 Emission spectra

In this section, we discuss the natural broadening of the Fe  $K\alpha$  spectral lines.

Nature has provided us with an extremely useful probe of the region very close to an accreting black hole - X-ray radiation of the matter in the vicinity of the black hole can imprint characteristic features into the X-ray spectra of black hole systems. The most prominent spectral feature is often the fluorescent  $K\alpha$  emission line of iron. Detailed X-ray spectroscopy of this feature can be used to study Doppler and gravitational redshifts, thus providing key information on the location and kinematics of the cold material. This is a powerful tool that allows one to probe within a few gravitational radii, or less, of the event horizon [74, 75, 76, 77]. (see, e.g., [81, 82, 83, 84] and references therein). This tool enables one to extract information for the accretion disk, the black hole and the interaction between them. The information that can be extracted for the accretion disk are the following features [74, 75, 77]: the size of the disk, the shape of the disk and the inclination angle of the disk with respect to the observer. About the black hole the following features may be determined: the physics that governs accreting matter, the mass of the black hole, the geometry of spacetime in the vicinity of the black hole and the value of the spin of the black hole. For example, the black hole's spin especially affects the red wing of the Fe  $K\alpha$  line, so the red wing is more extended towards lower energies for higher values of the spin [74].

Moreover, astrophysicists are able to identify what class of object we have.

For example, in quasars the strength of the iron line decreases with increasing luminosity. The X-ray radiation can provide information about the interaction between the black hole and the accretion disk. For example, the data suggest that the central regions of the accretion disk may be extracting the black hole spin energy.

Last but not least, one may use X-ray spectroscopy as a testing tool against other models especially regarding the disk. For example, it can show models for modified disk geometry instead of a simplified thin disk in the equatorial plane, models for more complex X-ray source geometry and models for a perturbed accretion flow (i.e., non-Keplerian flows) [77].

Before we continue to some simple examples of how the broadening impacts the emission spectrum, let us give a brief introduction about spectral lines, what kind of broadening one may observe in general and how the  $K\alpha$  emission line of iron is created.

A spectral line is a dark or bright line in a spectrum, resulting from a deficiency or excess of photons in a narrow frequency range, compared with the nearby frequencies. Spectral lines are a sort of “atomic fingerprint” as atoms emit light at very specific frequencies (because of the discrete energy levels) when exposed to electromagnetic waves. We have the production of two kinds of lines: emission and absorption lines. In the case of an emission line the detector sees photons emitted directly from atoms. In the case of an absorption line, the detector sees a decrease in the intensity of light (dark line) in the frequency that the photons are absorbed and then reemitted in random directions, which are mostly in directions different from the original one.

A spectral line extends over a range of frequencies, not a single frequency.

Moreover, the centre may be shifted from its nominal central wavelength. The reasons for such effects are divided in two categories. The first one is due to local conditions such as natural broadening, thermal Doppler broadening, pressure broadening and inhomogeneous broadening. Firstly, we have natural broadening. The uncertainty principle relates the lifetime of an excited state with the uncertainty of its energy. A short lifetime will have a large energy uncertainty and a broad emission spectrum. Later, we will talk about this kind of broadening in more detail. Secondly, we have thermal Doppler broadening, where the higher the temperature of the gas, the wider the distribution of velocities of the atoms in the gas. Therefore, because of the Doppler effect one ends up with a broadened spectrum. Thirdly, we have pressure broadening. There are many reasons for this kind of broadening. Two of them are associated with the presence of nearby particles that modify the radiation emitted by an individual particle. The rest of the reasons for the pressure broadening are associated with the nature of the perturbing force acting on an individual particle. Finally, we have inhomogeneous broadening, which is a general term for broadening because some emitting particles are in different local environments from others, and therefore emit at different frequencies.

The second category of causes for a shifted centre of a spectral line is due to nonlocal conditions such as opacity broadening, macroscopic Doppler broadening and gravitational redshift. Firstly, we have opacity broadening. Electromagnetic radiation emitted at a particular point in space can be absorbed as it travels through space. This absorption depends on the wavelength of the radiation. The line is broadened because photons at the line wings have a smaller reabsorption probability than the photons at the line centre. This process is also sometimes

called self-absorption. Secondly, we have the macroscopic Doppler broadening. Radiation emitted by a moving source is subject to Doppler shift due to a finite line-of-sight velocity projection. If different parts of the emitting body have different velocities (along the line of sight), the resulting line will be broadened, with the line width proportional to the width of the velocity distribution. Later we will see examples for this kind of broadening and we will generalize it in the relativistic case. Finally, we have the gravitational redshift. Electromagnetic radiation originating from an emitter that is in a gravitational field is redshifted when it is observed in a region of a weaker gravitational potential. This is a direct result of gravitational time dilation. As one moves away from a source of gravitational field, the rate at which time passes is increased relative to the case when one is near the source. We will discuss this kind of broadening in more detail. Moreover, gravitational redshift and the relativistic Doppler effect will be the main reasons for broadening in the examples that we are going to study in the rest of the thesis.

### 1.2.1 Natural broadening

In this subsection we discuss natural broadening. The uncertainty principle relates the lifetime of an excited state with the uncertainty of its energy. A short lifetime will have a large energy uncertainty and a broad emission.

The width of the spectral line of lifetime  $\tau$  will be

$$\Gamma \sim \frac{\hbar}{\tau}. \quad (1.22)$$

The wave function of an unstable state can be written as follows:

$$\psi(T) \propto \exp \left[ \frac{-i(2E_0 - i\Gamma)T}{2\hbar} \right]. \quad (1.23)$$

We make a Fourier transformation in order to get the wave-function in the energy representation [78],

$$\phi(\omega) \propto \int_0^\infty \exp[i\omega T] \psi(T) dT \propto \frac{\frac{\Gamma}{2\hbar}}{\frac{\Gamma^2}{4\hbar^2} + (\omega - \omega_0)^2} + i \frac{\omega - \omega_0}{\frac{\Gamma^2}{4\hbar^2} + (\omega - \omega_0)^2}. \quad (1.24)$$

Taking the square of this result we get,

$$|\phi(\omega)|^2 \propto \frac{1}{\frac{\Gamma^2}{4\hbar^2} + (\omega - \omega_0)^2}, \quad (1.25)$$

By normalizing this result such that the integral over all the frequencies and assuming that  $\omega_0 \gg \Gamma$  [79], we get the Breit-Wigner distribution<sup>3</sup>

$$\langle |\phi(\omega)|^2 \rangle = \frac{1}{\pi} \frac{\frac{\Gamma}{2\hbar}}{\frac{\Gamma^2}{4\hbar^2} + (\omega - \omega_0)^2}. \quad (1.26)$$

In the following graph 1.1, we can see a spectral line with large lifetime (the red curve, (2)) in comparison to the lifetime of a spectral line which is not affected by natural broadening (the black curve, (2).)

---

<sup>3</sup> The Breit-Wigner distribution, also known as the Lorentz distribution is a generalization of the Cauchy distribution,  $((1/\pi)/(1+x^2))$ , originally introduced to describe the cross section of the resonant nuclear scattering in the form

$$\sigma(E) = \frac{\Gamma}{2\pi [(E - E_0)^2 + \frac{\Gamma^2}{4}]}$$

which had been derived from the transition probability of a resonant state with known lifetime. This form can be read as the definition of the probability density as a function of the energy  $E$ , the integral over all energies is being 1. The distribution is fully defined by  $E_0$ , the position of the maximum, and by  $\Gamma$ , the full width at half maximum. For more details see [80].

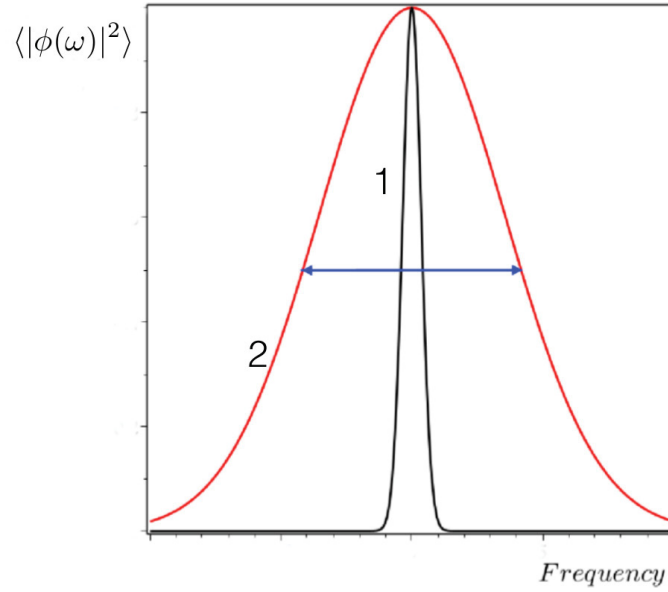


Figure 1.1: The black curve (1) shows the spectral line which is not affected by natural broadening. The red curve (2) represents a spectral line with large lifetime, due to natural broadening in comparison to the lifetime of the black curve.

As we see from Fig. 1.1, the number of particles or the intensity of the line or any other parameter that we want to study is a function of the frequency. However, when the emitter is moving, the frequency depends on time. Thus, the quantity that we want to study depends on time. Therefore, in order to see how the number of particles or the intensity or any other parameter that we want to study, depends on the frequency, one needs to average over time,

$$\tilde{F}(\tilde{\omega}) = \frac{1}{T} \int_0^T n(T) F(\omega, \omega_0(T)) dT, \quad (1.27)$$

where  $F(\omega, \omega_0(T))$  is the natural spectrum near the emission frequency  $\omega_0$ ,  $n(T)$  is the number of photons registered at time  $T$ , and  $\tilde{F}(\tilde{\omega})$  is the result of time averaging. If one is not interested in the time of arrival of the photons,  $\tilde{F}(\tilde{\omega})$  gives the effective broadening.

To sum up, natural broadening is one of the most important effects in physics. The uncertainty principle relates the lifetime of an excited state with the uncertainty of its energy. A short lifetime will have a large energy uncertainty and a broad emission. In the next section, it will be the spectrum or the number of particle per unit frequency (or, the ratio of frequencies) that we study. But, before we study the features of the line broadening let us explain what is the fluorescent  $K\alpha$  emission line of iron.

### 1.2.2 Fe $K\alpha$ spectral lines

One of the methods of study of black holes in astrophysics is based on broadening of the spectrum of radiation of ionized iron atoms. In our work, we analyze whether the change of the emission spectrum profiles can give us information about the magnetic field in the black hole vicinity. Here, we want to discuss what is the fluorescent  $K\alpha$  emission line of iron.

The fluorescent iron line is produced when one of the two K-shell (i.e.  $n = 1$ ) electrons of an iron atom (or ion) is ejected following the photoelectric effect of an X-ray. The threshold for the absorption by neutral iron is 7.1 keV. Following the photoelectric event, the resulting excited state decays. An L-shell ( $n = 2$ ) electron can then drop into the K-shell releasing 6.4 keV of energy as an emission line photon. In particular, the exact energy of the photon depends on the state of the ionization of the atom and is in the range of 6.40 – 6.97 keV. The broadening of the Fe  $K\alpha$  lines method is used in the study of accreting matter on stars, neutron stars and black holes.

This effect and the modifications of the emission line due to relativistic effects have been approached in several different ways: 1) Numerical computations for the

line profiles emitted by the accretion disk around black hole, for example in [85], by using direct integration of the photon trajectory in the Kerr metric. 2) Analytical calculations for the weak field limit we can find in [86, 87] for the Schwarzschild case in [88, 89, 90] and for the Kerr metric in [91]. 3) Numerical simulations based on ray-tracing method in the Kerr metric [92, 82, 93, 94], taking into account only photon trajectories reaching the observer's eye.

An example of the profile of the  $K\alpha$  line of iron ions is given in Fig. 1.2. Here we should note that our goal is to study the main features of the plot and not to reproduce the broadening as we see it in Fig. 1.2.

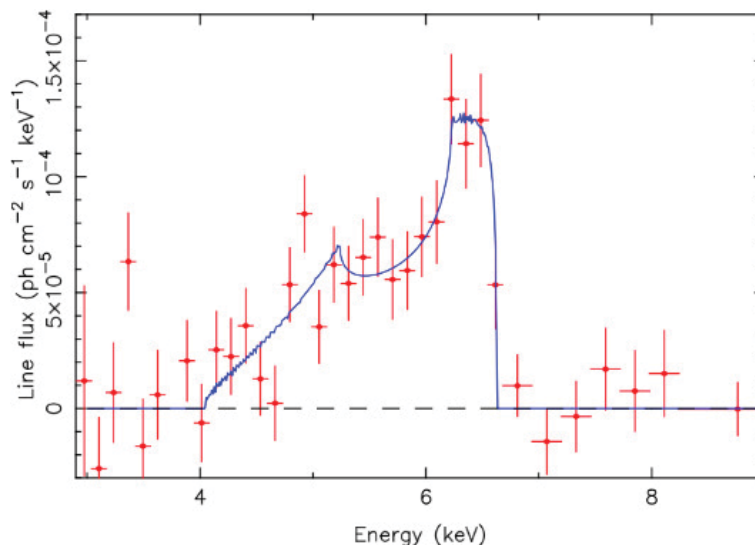


Figure 1.2: The profile of the Fe  $K\alpha$  line from Seyfert 1 galaxy MCG-6-30-15 observed by ASCA SIS detector. The figure is taken from [74].

### 1.3 Features of the line broadening

In this section, we will discuss the main features of the line broadening. We will start with the Newtonian case for a single emitter, and we will continue with the

finite ring case. We will close with the special relativistic case for a single emitter.

### 1.3.1 Newtonian case

Here, we will study a simple example demonstrating the modifications of the spectral line due to non local effects and especially due to the Doppler effect. Consider an emitter in a circular orbit around a Newtonian centre. Particle trajectories in a spherically symmetric spacetime are planar. By a rigid rotation one always can move this plane so that it coincides with the equatorial plane. In what follows we use this choice. Thus, at first, we assume that the particle (emitter) is revolving in the equatorial plane. Let us make the problem even simpler and consider that the orbital velocity  $\Omega$  and the radius of the orbit of the emitter  $r_e$  are independent of each other. Let us make the problem even more simple and set the observer in the equatorial plane as well but at a distance  $d \gg r_e$ , where  $r_e$  is the radius of the emitter's orbit.

If we assume that the emitter at rest emits monochromatic and isotropic radiation of angular frequency  $\omega_e$ , then at some distance  $d$  from the centre of the emitter's orbit, the number of photons ( $dN$ ) per unit time ( $dT$ ) per unit area ( $dA$ ) is given by the following equation,

$$\frac{dN}{dT dA} = \frac{\mathcal{N}}{4\pi d^2} , \quad (1.28)$$

where  $\mathcal{N}dT$  is the total number of photons emitted during time  $dT$ . Let us assume that the observer has a telescope with aperture area  $A$ . At distance  $d$  from the centre of the emitter's orbit the number of photons per unit time that are captured by the aperture area  $A$  is given by the following equation,

$$\frac{dN}{dT} = \frac{\mathcal{N}A}{4\pi d^2} . \quad (1.29)$$

We define the spectrum of the radiation ( $dN/dw$ ) as the number of photons per frequency ratio  $w$ ,

$$w \equiv \frac{\omega_o}{\omega_e} ,$$

where  $\omega_o$  is the observed frequency and  $\omega_e$  is the emitted frequency.

$$\frac{dN}{dT} = \frac{dN}{dw} \frac{dw}{dT} \Rightarrow \left| \frac{dN}{dw} \right| = \frac{\mathcal{N}A}{4\pi d^2} \left| \frac{dw}{dT} \right|^{-1} . \quad (1.30)$$

In this example we want to study the non-relativistic Doppler effect. Thus, the velocity of the emitter  $v$  with respect to the observer is much smaller than the speed of light,  $v \ll c$ . In this case the ratio of frequencies is given by

$$w \simeq \frac{1}{1 + \beta} \simeq 1 - \beta, \quad \beta = \frac{v}{c} . \quad (1.31)$$

In order to be precise  $v$  is the projection of the velocity of the emitter on the line of sight of the observer at some moment of time  $T$ . Thus, we have

$$v = \Omega r_e \sin \phi, \quad \phi = \Omega T . \quad (1.32)$$

Next, we calculate the derivative of the frequency with respect to the time,

$$\frac{dw}{dT} \simeq -\frac{\Omega^2 r_e}{c} \cos \phi . \quad (1.33)$$

From Eqs. (1.31) and (1.32) we get

$$\sin \phi \simeq (1 - w) \frac{c}{\Omega r_e}. \quad (1.34)$$

We can write  $\cos \phi$  as function of  $w$  in order to get the spectrum as a function of  $w$  only.

$$\cos \phi = \pm \sqrt{1 - \sin^2 \phi} \simeq \pm \sqrt{1 - (1 - w)^2 \frac{c^2}{\Omega^2 r_e^2}}. \quad (1.35)$$

Eq. (1.34) must give  $|\sin \phi| \leq 1$  or

$$\left| (1 - w) \frac{c}{\Omega r_e} \right| \leq 1. \quad (1.36)$$

The condition (1.36) imposes restrictions on the radii that contribute at a certain frequency. Later, we will see this in more detail.

From Eqs. (1.33) and (1.35) we get the final expression for the derivative of the ratio of the frequencies as a function of the ratio of the frequencies,

$$\left| \frac{dw}{dT} \right| \simeq \frac{\Omega^2 r_e}{c} \sqrt{1 - (1 - w)^2 \frac{c^2}{\Omega^2 r_e^2}}. \quad (1.37)$$

As we said before, we assume that the velocity of the particle is much smaller than the speed of light. In Fig. 1.3, we can see the spectrum as a function of the ratio of the frequencies. Moreover, we see the double peak because of the motion of the emitter around the Newtonian centre. The particle has maximum velocity for angles  $\phi = \pi/2$  and  $\phi = -\pi/2$ . Also, for  $v_{\max} = 0.1c$  these are the points that, we observe the minimum and maximum of the function  $w$  respectively, with the values to be  $w_{\min} = 0.9$  and  $w_{\max} = 1.1$ .

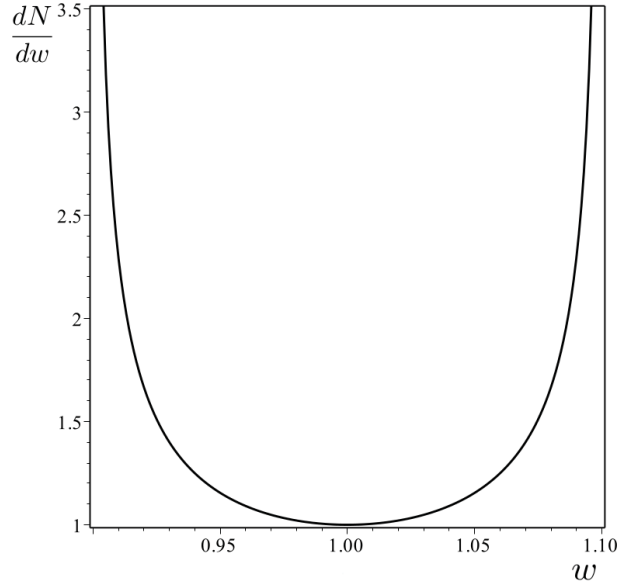


Figure 1.3: The modified spectrum as a function of the ratio of the frequencies due to the non-relativistic Doppler effect. Here,  $v_{\max} = 0.1c$ , and the dimensionless radius of the emitter is  $\rho = 2000$ .

### 1.3.2 Emission from a ring of finite width

Even though we will not consider this case in the rest of the thesis, it would be interesting to see what are the changes if we consider a narrow ring instead of just one orbit. In this case we will not have a single emitter anymore but many emitters in many orbits in the ring. We will make the following assumptions for simplicity. Firstly, we assume that, we have a uniform distribution for the emitters in the ring. Thus, a number of emitters for a given area element  $2\pi r dr$  is

$$dn = \Sigma 2\pi r dr, \quad (1.38)$$

where  $\Sigma$  is a constant (the number of emitters per area) that for simplicity we will consider to be equal to 1, and where  $r$ , the radius, is not a constant in this

case of study but is the second variable of the problem which can take different values. We recall that the first argument in the spectrum function is the ratio of the frequencies,  $w$ . Secondly, we assume that the ring and the observer are in the equatorial plane but with the observer at a distance  $d \gg r_e$ , where  $r_e$  is the maximum radius that we can have an emitter or is the outer radius of the ring. Thirdly, we assume that in the ring, we have Keplerian particles, which means that their orbital velocity  $\Omega$  is given as follows:

$$\Omega = \frac{\sqrt{GM}}{r^{3/2}}, \quad (1.39)$$

where  $G$  is the gravitational constant and  $M$  is the mass of the object in the centre. The last assumption is the same that was made earlier. Namely, we assume that the motion of the particles in the ring is non-relativistic. For example, choose  $v_{\max} = 0.1c$ . Then we have

$$v_{\max} = 0.1c \Rightarrow \frac{c}{\Omega r} = 10 \quad (1.40)$$

from Eqs. (1.40) and (1.39). In order to avoid relativistic effects in the particular case that  $v_{\max} = 0.1c$ , we have

$$r \geq 100 \frac{GM}{c^2} \Rightarrow \rho_{\min} \geq 50, \quad (1.41)$$

where  $\rho$  is the dimensionless radius,

$$\rho = \frac{rc^2}{2GM}.$$

From Eqs. (1.37) and (1.39) we obtain

$$\frac{dw}{dT} = -\frac{c^3}{4GM} \frac{1}{\rho^2} \sqrt{1 - (1-w)^2} 2\rho. \quad (1.42)$$

In order to get the spectrum as a function of the ratio of frequencies for the disk, we need to integrate the dimensionless radius  $\rho$  over the disk at fixed  $w$ , but we need to restrict the radii to those that for some angle  $\phi$  gives the desired value  $w$ . In Eq. (1.42) this is equivalent to integrating only over values of  $\rho$  that keep the quantity under the square root nonnegative. If for  $\rho = \rho_{\text{in}}$  (the inner radius of the disk) this quantity is negative for the chosen  $w$ , then no radii contribute to the integral, so there is no contribution from the ring to the spectrum at that value of  $w$ . If the quantity under the square root is positive for  $\rho = \rho_{\text{in}}$  but not for  $\rho = \rho_{\text{out}}$ , then the integral runs from  $\rho = \rho_{\text{in}}$  to  $\rho = \rho_{\text{max}}$  with in this case  $\rho_{\text{max}} = (1/2)/(1-w)^2$ , the value of  $\rho$  where the quantity goes to zero. Finally, if the quantity under the square root is nonnegative for  $\rho = \rho_{\text{out}}$  as well as for  $\rho = \rho_{\text{in}}$ , then one sets  $\rho_{\text{max}} = \rho_{\text{out}}$  and again integrates  $\rho$  from  $\rho_{\text{in}}$  to  $\rho_{\text{max}}$ .

$$\int \frac{dN}{dw} dn = \int_{\rho_{\text{in}}}^{\max(\rho_{\text{in}}, \min(\rho_{\text{out}}, \rho_{\text{max}}))} \frac{dN}{dw} \frac{dn}{d\rho} d\rho. \quad (1.43)$$

In Fig. 1.4, we can see the spectrum of a non-relativistic disk as a function of the ratio of the frequencies. For this figure  $\rho_{\text{in}} = 2000$  and  $\rho_{\text{out}} = 5000$ . We could have any value of  $\rho \gg 50$  (for the particular example in which we assume  $v_{\text{max}} = 0.1c$ ) in order to avoid the relativistic effects, but the qualitative features of the spectrum that we want to study do not change. Moreover, we see the double peak because of the motion of the emitter around the Newtonian centre. These peaks are smoothed as we were expecting because of the integration over the disk.

The main contribution of the peaks comes from the outer part of the disk. In

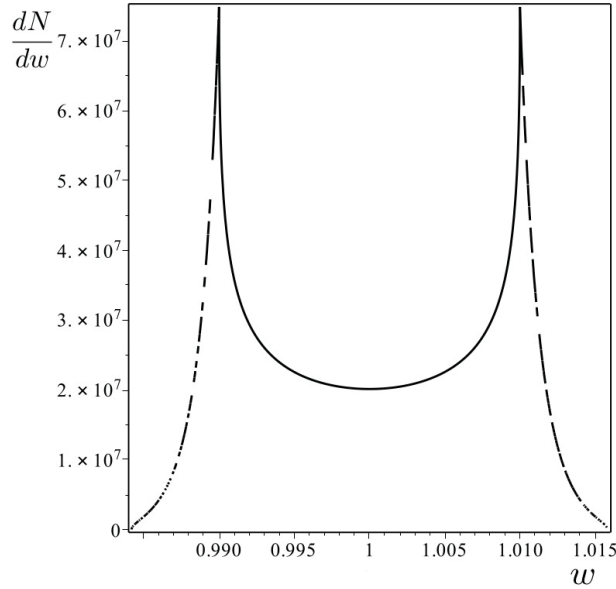


Figure 1.4: The modified spectrum of a disk as a function of the ratio of the frequencies due to the non-relativistic Doppler effect.

particular, if we plot the spectrum of a single orbit as we did in the previous subsection, but for  $\rho = \rho_{out} = 5000$ , we can see that the frequencies where the spectrum tends to infinity are the same frequencies that we observe the maximum number of photons in the finite ring case. In general, if we increase the outer radius of the ring, we would see the peaks of the spectrum come closer to each other. We can observe this in Fig. 1.5. Next consider the single orbit case, in which the number of photons between the peaks is always greater than zero. On the other hand, on the left side of the left peak and the right side of the right peak the number of photons is zero. Thus, when we sum over all the single orbits for radii that increase, we get the peaks to be in the same position as the peaks in the outermost orbit due to the fact that all the orbits giving those two frequencies

have number of photons greater than zero. This can be better understood by the Fig. 1.5 and 1.6.

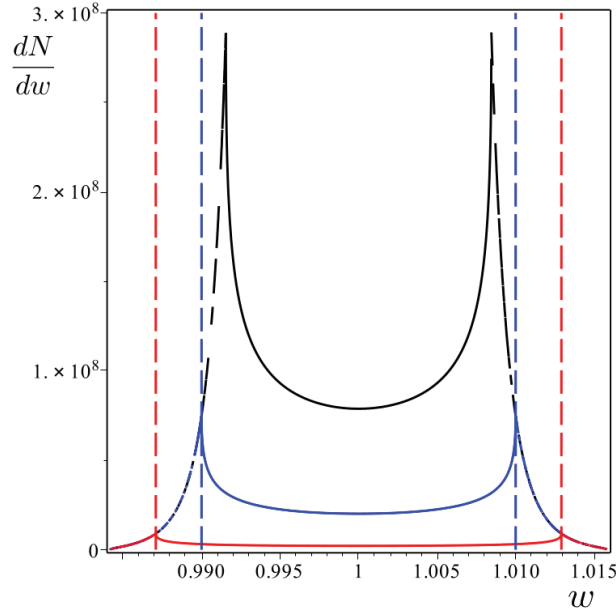


Figure 1.5: The modified spectrum of a disk as a function of the ratio of the frequencies due to the non-relativistic Doppler effect. The black curve is the spectrum of a disk with  $\rho_{in} = 2000$  and  $\rho_{out} = 7000$ . The blue curve is the spectrum of a disk with  $\rho_{in} = 2000$  and  $\rho_{out} = 5000$ . The red curve is the spectrum of a disk with  $\rho_{in} = 2000$  and  $\rho_{out} = 3000$ .

### 1.3.3 Relativistic case

The next step is to consider a particle which is revolving with a speed close to the speed of light. The main effects that we expect are the relativistic beaming effect<sup>1</sup> and the transverse Doppler effect<sup>2</sup>. In order to have the result of the “relativistic”

<sup>1</sup> Relativistic beaming is the process by which relativistic effects modify the luminosity of emitting matter that is moving at speeds close to the speed of light.

<sup>2</sup> The transverse Doppler effect is the nominal redshift or blueshift predicted by special relativity that occurs when the emitter and receiver are at the point of closest approach. Light emitted at closest approach in the source frame will be redshifted at the receiver. Light received at closest approach in the receiver frame will be blueshifted relative to its source frequency.

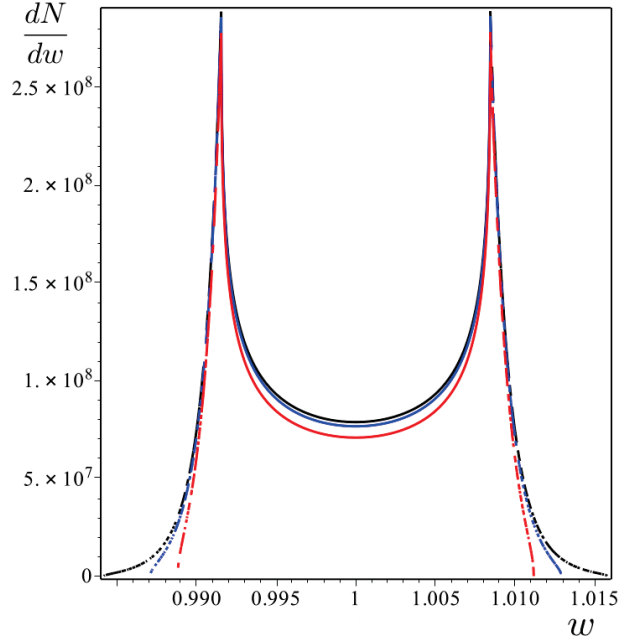


Figure 1.6: The modified spectrum of a disk as a function of the ratio of the frequencies due to the non-relativistic Doppler effect. The black curve is the spectrum of a disk with  $\rho_{in} = 2000$  and  $\rho_{out} = 7000$ . The blue curve is the spectrum of a disk with  $\rho_{in} = 3000$  and  $\rho_{out} = 7000$ . The red curve is the spectrum of a disk with  $\rho_{in} = 4000$  and  $\rho_{out} = 7000$ .

broadening, we will need to calculate the solid angle of the emitted photons that pass through the “telescope” aperture, since the relativistic effects change the angles as well.

The spacetime is flat and in spherical coordinates is given as follows:

$$ds^2 = -dT^2 + dr^2 + r^2 d\theta^2 + r^2 \sin^2 \theta d\phi^2. \quad (1.44)$$

We again assume that the emitter is in the equatorial plane. The four-velocity of the particle in terms of a local rest frame  $\{\mathbf{e}_T, \mathbf{e}_r, \mathbf{e}_\theta, \mathbf{e}_\phi\}$  is

$$u = \gamma (e_{(T)} + \beta e_{(\phi)}) , \quad (1.45)$$

where  $\beta = \Omega r$  with angular velocity  $\Omega$ . For simplicity we set  $c = 1$ . The factor  $\gamma$  is given as follows:

$$\gamma = \frac{1}{\sqrt{1 - \beta^2}} .$$

Moreover, the specific angular momentum  $\ell$  of a photon in flat space time is equal to the impact parameter<sup>1</sup>  $q$ , so

$$\ell = q , \quad (1.46)$$

where  $\ell = L/E$  with  $L$  the angular momentum and  $E$  the energy of the photon.

In Fig. 1.7, we see photon 2 with specific angular momentum  $\ell$  or  $q$  and photon 1 with specific angular momentum  $q + \delta q$ .  $\Phi$  is the angle between the radial direction  $r_e$  and the photon trajectory. From Fig. 1.7 we can see that

$$\ell = \frac{\sin(\Phi)}{\zeta} , \quad (1.47)$$

where  $\zeta$  is the inverse radius,  $\zeta = 1/r$ .

The number of photons per unit proper time  $\tau_e$  of the emitter emitted within solid angle  $\Delta\Omega_e$  in the emitter's frame is

$$\frac{dN}{d\tau_e} = \frac{\mathcal{N}}{4\pi} \Delta\Omega_e . \quad (1.48)$$

---

<sup>1</sup> The impact parameter in flat spacetime is defined as the perpendicular distance between the tangent to the path of a projectile when it is far away and the centre of a potential field created by an object that the projectile is approaching.



$$\frac{dN}{d\omega_o} = \frac{\mathcal{N}A}{4\pi d^2} \frac{dT_o}{d\omega_o} \frac{d\tau_e}{dT_o} w^2. \quad (1.52)$$

Second, we change from  $\frac{dN}{d\omega_o}$  to

$$\frac{dN}{dw} = \omega_e \frac{dN}{d\omega_o} = \frac{d\tau_e}{dw} \frac{\mathcal{N}A}{4\pi d^2} w^2. \quad (1.53)$$

Finally we get

$$\frac{dN}{dw} = \frac{\mathcal{N}A}{4\pi d^2} \left| \frac{d\alpha}{d\tau_e} \right|^{-1}, \quad (1.54)$$

where  $\alpha = 1/w$  and  $w$  the ratio of the frequencies is given as follows:

$$w = \frac{1}{\gamma(1 + \beta\ell\zeta)}. \quad (1.55)$$

Let us now obtain an expression for the time derivative of  $\alpha$ . First let us notice that when we compare the two times along null rays from the emission to the observation  $d/d\tau_e = (1/w)(d/dT_o)$ , so that one has

$$\frac{d\alpha}{d\tau_e} = \gamma^2 \beta \zeta \dot{\ell} (1 + \beta\ell\zeta), \quad (1.56)$$

where a dot denotes a derivative with respect to the coordinate time  $T$  at the orbit of the emitter. Moreover, we have  $\dot{\phi} = \Omega$  and

$$\dot{\ell} = \frac{\cos(\Phi)}{\zeta} \dot{\Phi}, \quad (1.57)$$

$$\dot{\Phi} = \dot{\phi} = \Omega. \quad (1.58)$$

To illustrate the role of the relativistic effects, we consider a particle revolving with

$\beta = 0.5$ , which means half of the speed of light. We could have any value of  $\beta$  as long as it is close to the speed of light, but the qualitative features of the spectrum that we want to study do not change.

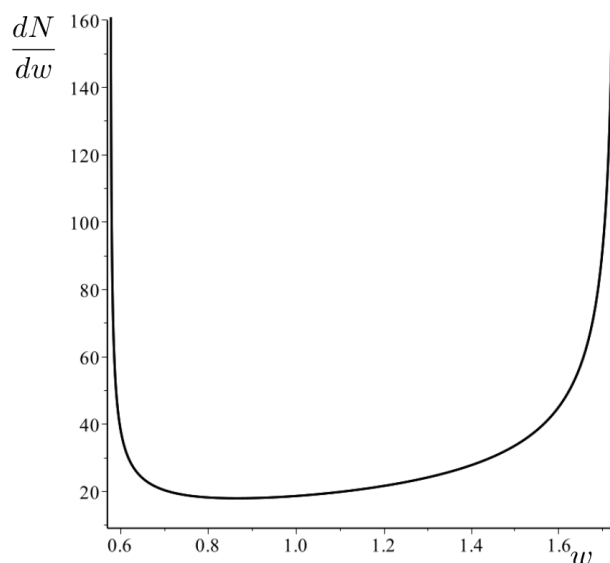


Figure 1.8: Spectrum in the relativistic case.

From Fig. 1.8 we can see that the spectrum is much more broadened because of the relativistic Doppler effect. Moreover, we see an asymmetry of the peaks. This is due to the special relativistic beaming effect which enhances the blue peak of the spectral line. In other words, when the emitter is moving toward the observer sees much more photons than the case that the emitter is moving away from the observer.

In the presence of a static gravitational field, one can expect an additional redshift of the spectrum. For example, this happens when an emitter is at rest with respect to a static black hole. In this case the number of the photons that we will observe is different because some of the emitted photons will be absorbed by the black hole. Another effect that we need to take into account is the bending

of light or gravitational lensing. The light follows the curvature of the spacetime. Therefore, when it passes near a black hole its trajectory is bent. The light from an emitter on the other side of the compact object will be bent towards an observer's eye.

The effects that we mentioned in the last paragraph and the addition of the magnetic field in the background of the Schwarzschild geometry will be the main effects that we will study in the following chapters. In particular, we will study how the emission spectrum is modified when the emitter is orbiting a weakly magnetized black hole.

## Chapter 2

# Motion of charged particles and null rays

In this chapter, we will present the main features of the motion of charged particles near a magnetized Schwarzschild black hole. We also recall properties of null rays in the Schwarzschild geometry. In this thesis, we study particles in circular orbits around a weakly magnetized black hole. However, first we need to show that radial oscillations disappear very fast. This justifies why we are considering circular orbits where the particles can live for long time in the same orbit. In Section 2.1, we derive the dimensionless form of the equations for charged particles in the equatorial plane, introduce the effective potential, present the main features of the effective potential and discuss possible orbits. Then we discuss the radial oscillations in the equatorial plane. We show that the radial oscillations disappear very quickly due to synchrotron radiation. We continue the chapter with a discussion in two separate subsections about the main features of the stable circular orbits and the innermost stable circular orbits. Finally, we will discuss the circular motion in

the rest frame basis (i.e., we use the rest frame which is a local basis along the trajectory). Then, we move to the motion of null rays. We will present the motion of null rays in the equatorial plane and introduce the impact parameters.

## 2.1 Charged particle

In this section, we will discuss motion in the equatorial plane, the effective potential and the classification of the orbits of charged particles. We will present the classes of stable circular orbits (SCO) and innermost stable circular orbits (ISCO). We will close the section with a discussion about the circular orbit in the rest frame.

The metric of the Schwarzschild spacetime is given by

$$dS^2 = -f dT^2 + \frac{dr^2}{f} + r^2 d\Omega^2, \quad f = 1 - \frac{r_g}{r}, \quad (2.1)$$

where  $r_g = 2M$  is the black hole's gravitational radius, and

$$d\Omega^2 = d\theta^2 + \sin^2 \theta d\phi^2 \quad (2.2)$$

is the metric on a unit sphere  $S^2$ . In our work, we assume the black hole is weakly magnetized and the electric charge is zero ( $Q = 0$ ). As we mentioned in the previous chapter, this means that the magnetic field is not strong enough to cause any back reaction to the metric. However, it is strong enough to modify the orbits of the charged particles. The vector potential (1.21) is given as follows,

$$A^\mu = \frac{B}{2} \xi_{(\phi)}^\mu, \quad (2.3)$$

where  $B = \text{const}$  is the asymptotic strength of the homogeneous magnetic field at infinity (see, e.g., [67, 72]). The magnetic field is static and axisymmetric and it is directed orthogonal to the equatorial plane  $\theta = \pi/2$ . The Killing vector  $\xi_{(\phi)}^\mu$  is associated with axial symmetry. In general, the Schwarzschild spacetime possesses four Killing vectors,

$$\xi_{(T)} = \partial_T, \quad \xi_{(\phi)} = \partial_\phi, \quad (2.4)$$

$$\xi_x = -\cos\phi\partial_\theta + \cot\theta\sin\phi\partial_\phi, \quad (2.5)$$

$$\xi_y = \sin\phi\partial_\theta + \cot\theta\cos\phi\partial_\phi. \quad (2.6)$$

The first one is the generator of time translations, while the other three are the generators of rotations. For the motion in the magnetized Schwarzschild black hole [67, 68, 95], there exist two conserved quantities associated with the Killing vectors: the energy  $E > 0$  and the azimuthal angular momentum  $L$ ,

$$E = -\xi_{(t)}^\mu P_\mu = \left(1 - \frac{2M}{r}\right)m\frac{dT}{d\sigma}, \quad (2.7)$$

$$L = \xi_{(\phi)}^\mu P_\mu = r^2 \sin^2\theta \left[ m\frac{d\phi}{d\sigma} + q\frac{B}{2} \right], \quad (2.8)$$

where  $P_\mu = mu_\mu + qA_\mu$ ,  $\sigma$  is the proper time,  $u_\mu$  is the 4-velocity and  $A_\mu$  the vector potential.

The spacetime (2.1) has only one dimensional parameter,  $r_g$ , and one can write the metric in the form

$$dS^2 = r_g^2 ds^2, \quad ds^2 = -f dt^2 + \frac{d\rho^2}{f} + \rho^2 d\Omega^2, \quad (2.9)$$

where  $t = T/r_g$  and  $\rho = r/r_g$  are the dimensionless time and radius, and  $f = 1 - 1/\rho$ . In what follows, we shall use this dimensionless form of the metric.

The electromagnetic field tensor can be written as follows,

$$\begin{aligned} F_{\mu\nu} &= 2A_{[\nu,\mu]} \\ &= 2Br \sin \theta \left( \sin \theta \delta_{[\mu}^r \delta_{\nu]}^\phi + r \cos \theta \delta_{[\mu}^\theta \delta_{\nu]}^\phi \right). \end{aligned} \quad (2.10)$$

A charged particle motion obeys the equation

$$\frac{Du^\mu}{d\tau} = \frac{q}{m} F^\mu{}_\nu u^\nu. \quad (2.11)$$

Here  $u^\mu = dx^\mu/d\tau$  is the particle 4-velocity,  $u^\mu u_\mu = -1$ ,  $\tau$  is its dimensionless proper time,  $q$  and  $m$  are its electric charge and mass, respectively.

By making the following transformations,

$$\begin{aligned} \mathcal{E} &= \frac{E}{m}, \quad l = \frac{L}{mr_g}, \\ r &= r_g \rho, \quad T = r_g t, \quad \sigma = r_g \tau, \\ b &= \frac{qB r_g}{2m}, \end{aligned} \quad (2.12)$$

we write (2.7 and 2.8) in the form,

$$\mathcal{E} = \left(1 - \frac{1}{\rho}\right) \frac{dt}{d\tau}, \quad (2.13)$$

$$l = \rho^2 \left[ \frac{d\phi}{d\tau} + b \right]. \quad (2.14)$$

The radial equation of motion in dimensionless form is

$$\left(\frac{d\rho}{d\tau}\right)^2 = \mathcal{E}^2 - U. \quad (2.15)$$

where the effective potential  $U$  is

$$U = \left(1 - \frac{1}{\rho}\right) \left[1 + \left(\frac{l - b\rho^2}{\rho}\right)^2\right]. \quad (2.16)$$

The equation of motion in the equatorial plane is invariant under the following transformations:

$$b \rightarrow -b, \quad l \rightarrow -l, \quad \phi \rightarrow -\phi. \quad (2.17)$$

Thus, without loss of the generality, one can assume that the charge  $q$  (and hence  $b$ ) is positive. For a particle with a negative charge it is sufficient to make the transformation Eq. (2.17). According to the adopted convention, we have  $b \geq 0$ . The parameter  $l$  can be either positive or negative. For  $l > 0$  (sign  $+$ ) and the motion in the  $\phi$ -direction is counter-clockwise, the Lorentz force acting on a charged particle is repulsive, i.e., it is directed outward from the black hole. Following the paper [67], we call such motion *anti-Larmor motion*. In the opposite case when  $l < 0$  (sign  $-$ ) and the motion in the  $\phi$ -direction is clockwise, the Lorentz force is attractive, i.e., it is directed toward the black hole. We call it *Larmor motion*. A circular orbit in which the angular momentum of the particle is positive,  $l > 0$ , and  $d\phi/d\tau < 0$ , is not allowed. Such motion requires  $b > l/\rho^2$ , but then in this case  $U_{,\rho} > 0$ , so the motion cannot be circular.

### 2.1.1 Effective potential

In this subsection, we will study some properties of the effective potential (2.16). Let us assume that the mass of the black hole  $M$  and the strength of the magnetic field  $B$  are fixed. Therefore, for a specific charged particle the parameter  $b$

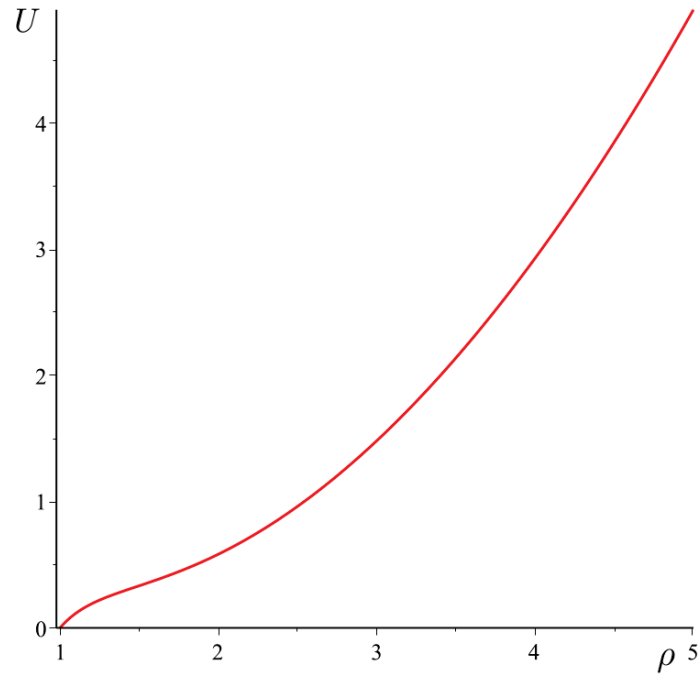


Figure 2.1: The effective potential for  $b = 0.5$  and  $l = 1.18$ .

is fixed as well. Then, the effective potential is a function of  $l$  and  $\rho$ . In the Schwarzschild spacetime the horizon of the black hole is located at  $r = r_g = 2M$  or in dimensionless units,  $\rho = 1$ . The variable  $\rho$  is measured in units of gravitational radius  $r_g$  so  $\rho \in (1, +\infty)$ . The effective potential is positive in this region (see equation (2.16)). For  $\rho = 1$  the effective potential (2.16) is equal to zero,  $U = 0$ . When  $\rho \rightarrow +\infty$  the effective potential grows as  $b^2\rho^2$ . This implies that in the weakly magnetized Schwarzschild geometry a particle never reaches spatial infinity.

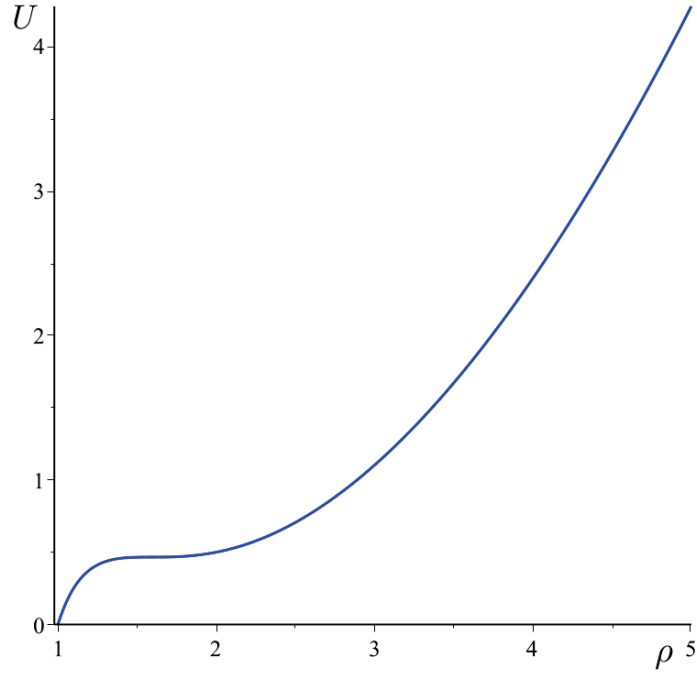


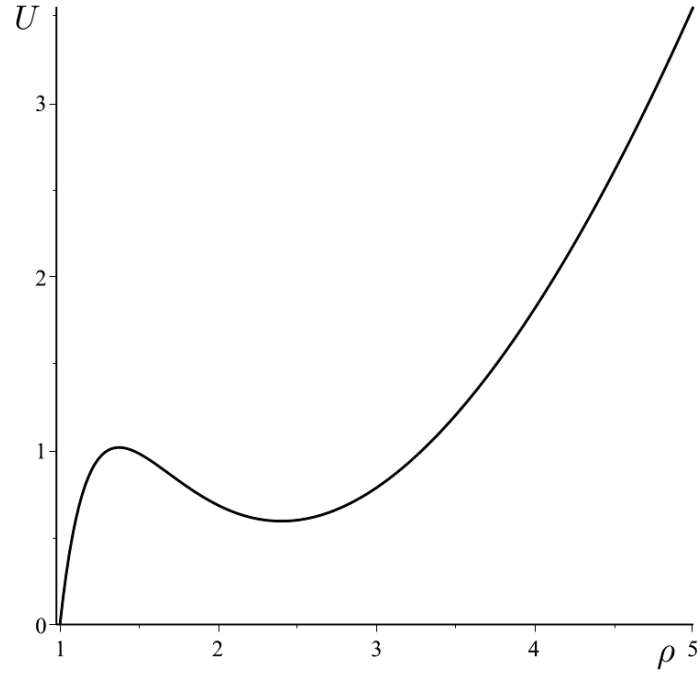
Figure 2.2: The effective potential for  $b = 0.5$  and  $l = 2.07$ .

Next, we would like to study possible orbits around the black hole. We start our analysis with finding the roots of the first and second derivative of the effective potential, since these roots determine where the effective potential has extrema and what kind of extrema these are. We take the first and second derivative of the effective potential with respect to the dimensionless radius  $\rho$ ,

$$U_{,\rho} = \frac{1}{\rho^2} \left[ 1 + \frac{(l - b\rho^2)^2}{\rho^2} \right] + \left( 1 - \frac{1}{\rho} \right) \left[ -\frac{4(l - b\rho^2)b}{\rho} - \frac{2(l - b\rho^2)^2}{\rho^3} \right]. \quad (2.18)$$

This relation can be rewritten as

$$U_{,\rho} = \frac{1}{\rho^4} [2b^2\rho^5 - b^2\rho^4 - 2lb\rho^2 + \rho^2 - 2l^2\rho + 3l^2]. \quad (2.19)$$


 Figure 2.3: The effective potential for  $b = 0.5$  and  $l = 3.22$ .

The second derivative is given as follows,

$$\begin{aligned}
 U_{,\rho\rho} &= -2 \frac{1 + \frac{(l-b\rho^2)^2}{\rho^2}}{\rho^3} - \frac{2}{\rho^2} \left[ \frac{4b(l-b\rho^2)}{\rho} + \frac{2(l-b\rho^2)^2}{\rho^3} \right] \\
 &+ \left( 1 - \frac{1}{\rho} \right) \left[ 8b^2 + \frac{12(l-b\rho^2)b}{\rho^2} + \frac{6(l-b\rho^2)^2}{\rho^4} \right]. \quad (2.20)
 \end{aligned}$$

This relation can be rewritten as

$$U_{,\rho\rho} = \frac{1}{\rho^5} [b^2\rho^5 - \rho^2 + 2lb\rho^2 + 3l^2\rho - 6l^2]. \quad (2.21)$$

A 5th-order polynomial expression such as the one in (2.19) may have as many as five real roots. However, it was shown in [68] in our case that  $U_{,\rho}$  has not more

than two real roots for  $\rho \in (1, +\infty)^1$ .

These two roots are at the points  $\rho = \rho_{max}$ , which is the point that the effective potential has a local maximum, and  $\rho = \rho_{min}$ , which is the point that the effective potential has a local minimum. At the radius  $\rho = \rho_{max}$  there is an unstable orbit, while at the radius  $\rho = \rho_{min}$  there is a stable circular orbit (SCO). If we impose the condition that  $U_{,\rho\rho} = 0$ , we will get the innermost stable circular orbit (ISCO).

The effective potential has different behaviour depending on the values of  $l$  and  $b$ . We can classify the particle's motion in the equatorial plane in the following manner. For  $l > 0$  and  $b > 0$  we can have three cases for the motion of a particle from the effective potential (2.16):

- there are no circular orbits,
- for fixed value of  $b$  there is a critical value of  $l$  where we have an innermost circular orbit. If for example  $b = 0.5$  then, we have an innermost circular orbit with  $l \simeq 2.07$  and  $\rho \simeq 1.59$
- we have both stable and unstable circular orbits. For  $\rho = \rho_{max}$  the orbit is unstable, and for  $\rho = \rho_{min}$  the orbit is stable. For more details see [68]. We are going to focus in this case.

Figures (2.1)-(2.3) illustrate the behaviour of the effective potential for three different cases. In Figure (2.1), the effective potential is plotted for  $b = 0.5$  and  $l = 1.18$ . As we see there are no circular orbits. Figure (2.2) corresponds to  $b = 0.5$  and  $l = 2.07$ . There is an innermost stable circular orbit with  $\rho = 1.59$ .

---

<sup>1</sup> An easy way to determine an upper bound on the number of real roots is the following. Let us start with the sign of the coefficient of the highest power. Next, count the number of sign changes as you proceed from the highest to the lowest power. Then, the number of sign changes is the maximum number of real roots [70, 71].

Figure (2.3) corresponds to  $b = 0.5$  and  $l = 3.22$ . There are unstable orbits where the effective potential is maximum. On the other hand, the stable circular orbits correspond to the minimum of the effective potential.

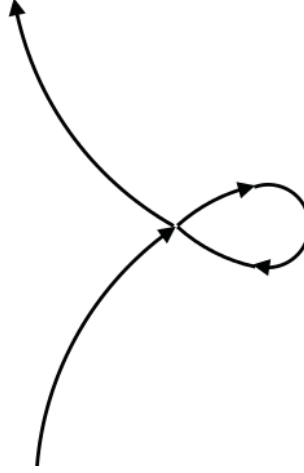


Figure 2.4: Type of a bounded trajectory with curls. Arrows illustrate the direction of motion of a charged particle.

Next, we focus on bounded trajectories that are not circular but are close to circular. Assume that, the radius of a charged particle oscillates between  $\rho = \rho_1$  and  $\rho = \rho_2$ , with

$$\rho_{max} \leq \rho_1 \leq \rho_{min} \leq \rho_2.$$

Then the radial motion of the particle is periodic. From the equation (2.15) we can calculate the period of the radial motion,

$$\frac{d\rho}{d\tau} = \pm [\mathcal{E}^2 - U]^{1/2} \Rightarrow \Delta\tau = \pm 2 \int_{\rho_1}^{\rho_2} \frac{d\rho}{[\mathcal{E}^2 - U]^{1/2}}. \quad (2.22)$$

From equation (2.14) we get

$$\frac{d\phi}{d\tau} = \frac{l}{\rho^2} - b. \quad (2.23)$$



Figure 2.5: Limiting case of bounded trajectory with curls. Arrows illustrate the direction of motion of a charged particle.

In the case of  $l < 0$  the motion in the  $\phi$ - direction is clockwise, the Lorentz force is attractive and the right hand side of this equation (2.23) is negative. This motion is modulated by the motion in the radial direction. In the case of  $l > 0$  the motion in the  $\phi$ - direction is counter-clockwise, and the Lorentz force is repulsive. If  $\rho_2 < \rho_*$ , (where  $\rho = \rho_* \equiv (l/b)^{1/2}$ ), the right hand side of equation (2.23) is positive and  $\phi$  grows monotonically with time. This motion is modulated by the radial motion as well. Such kind of motion does not have curls. See Figure (2.6). In the case  $\rho_2 > \rho_*$ , for the motion of the particle in the domain  $(\rho_1, \rho_*)$ , we have  $\phi$  increasing with time. On the other hand, in the domain  $(\rho_*, \rho_2)$ ,  $\phi$  is decreasing with time. The increase of  $\phi$  can not be compensated by the decrease, so there is a drift of the particle in the positive  $\phi$ - direction. Such motion has curls. See Figure (2.4). In the critical case - see figure (2.5) - when  $\rho_2 = \rho_*$ , the trajectory is similar to a

cycloid. For more details of the three different kind of trajectories (i.e., with curls, without curls and the critical case), see [68].

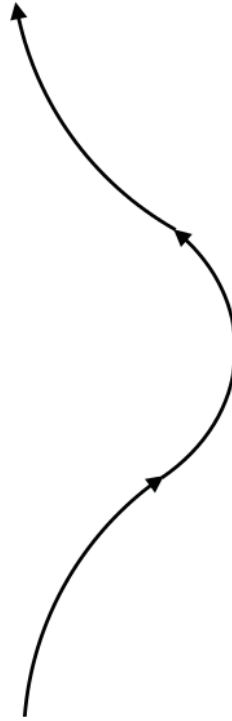


Figure 2.6: Type of a bounded trajectory without curls. Arrows illustrate the direction of motion of a charged particle.

In Appendix C, we discuss small oscillations about circular orbits. According to [101], because of the energy loss, the radial oscillations about a stable circular fiducial orbit decay. Therefore, we have a transition from a bound orbit, which has loops, to a circular bound orbit, due to synchrotron radiation. The transition time  $\Delta\tau$ , as measured with respect to a particle's proper time  $\tau$ , is ten orders of magnitude shorter for electrons than that for protons and heavy ions. In particular,

one can estimate  $\Delta\tau$  as follows,

$$\Delta\tau \sim \frac{\rho}{2\kappa(\rho - 1)}, \quad (2.24)$$

where  $\kappa$  is defined as

$$\kappa = \frac{8q^2b^2}{3mr_g}. \quad (2.25)$$

According to [102], the magnetic field  $B$  is of the order of  $10^8$  G near a stellar mass black hole,  $M \sim 10M_\odot$ , and is of the order of  $10^4$  G for a supermassive black hole,  $M \sim 10^9M_\odot$ . Therefore, for an electron revolving around a stellar mass or supermassive black hole, we have  $\kappa \sim 10^3$ , and for a proton  $\kappa \sim 10^{-7}$ . The dimensionless transition time for electrons is  $\Delta\tau_{\text{electron}} \sim 10^{-3}$ , whereas for the protons we have  $\Delta\tau_{\text{proton}} \sim 10^7$ . Therefore, the radial oscillations of electrons revolving around a black hole disappear faster than the radial oscillations of protons revolving a black hole.

Particles in circular orbits also lose energy because of synchrotron radiation. However, this process is extremely slow, so that they can live for a very long time in such orbits. In Appendix D, we present an estimation of this time that is required for a particle to move from one radius to another one due to energy loss because of synchrotron radiation.

In order to compare the time that particles stay in circular orbit with the time of decay of the radial oscillations we need first to calculate the dimensionless transition time  $\Delta t$  from the estimation of the particle's proper time given in [101]. Thus, we have

$$\Delta t = \Delta\tau\gamma, \quad (2.26)$$

where the factor  $\gamma$  comes from the normalization  $u^\mu u_\mu = -1$ . If we restrict ourselves to circular orbits, then  $u^\mu = \gamma(1, 0, 0, \Omega)$ , so we have

$$\gamma = \frac{1}{\sqrt{\left(1 - \frac{1}{\rho}\right) - \rho^2 \Omega^2}}. \quad (2.27)$$

Using equation (2.24) we get

$$\Delta t = \frac{\rho \gamma}{2(\rho - 1)} \frac{1}{\kappa}. \quad (2.28)$$

The factor  $(\rho \gamma)/(2(\rho - 1))$  for our estimation where  $b = 2.25$  and  $\rho = 1.3$  is almost equal to 4. We should note that the dependance of  $\Omega$  on  $l, b$  and  $\rho$  we will see in detail in the next subsection. Taking into account only the order of magnitude we have

$$\Delta t \sim \frac{1}{\kappa}, \quad (2.29)$$

so we have  $t_{electron} \sim 10^{-3}$  and  $t_{proton} \sim 10^7$ . This is the case for a magnetic field  $B \sim 10^8$  (for a stellar mass black hole). However, in our case the magnetic field that we consider is much smaller than that. In particular, in Appendix D our estimation is done for  $b = 2.25$ . In such a case we would have  $t_{electron} \sim 10^5$ . If we compare this result to the time that particles spend in circular orbit ( $t \sim 10^{17}$ ) we can say that the radial oscillations disappear very fast. Thus, for the rest of our work, we will stick to the circular orbits where the particles can live for a very long time in the same orbit.

### 2.1.2 Stable circular orbits (SCO's)

In general, the motion of charged particles around a weakly magnetized Schwarzschild black hole is chaotic [67, 95, 96]. The equations of motion appear to be separable in the equatorial plane only. In [97], it was shown that the motion near a Kerr black hole in the presence of a magnetic field generated by a current loop has chaotic character depending on the initial conditions. However, as it was shown in [98], that for an extremal Kerr black hole the chaotic behaviour weakens in particles trajectories. In [99], the chaotic nature of the dynamics near a Schwarzschild black hole in the presence of an axisymmetric magnetic field was studied. In [100], an analysis was made of the off-equatorial motion of charged particles in a Schwarzschild black hole with a dipole magnetic field and a Kerr black hole immersed in a uniform axisymmetric magnetic field. It was shown that the off-equatorial motion is regular until the particle energy is raised to the level at which trans-equatorial motion occurs.

In order to make things simpler, we will restrict ourselves by considering motion in the equatorial plane ( $\theta = \pi/2$ ). Let us focus on circular motion. In this case, the four-velocity of the particle in coordinates  $(t, \rho, \theta, \phi)$  is

$$w^\mu = \gamma (1, 0, 0, \Omega) . \quad (2.30)$$

From Eqs. (2.13) and (2.14), one can find the angular velocity of a particle in circular motion,

$$\Omega = \frac{d\phi}{dt} = \frac{\rho - 1}{\rho \mathcal{E}} \left( \frac{l}{\rho^2} - b \right) . \quad (2.31)$$

For Stable Circular Orbits (SCO), and for the anti-Lamor particles we have,

$$l = \frac{-b\rho^2 + \sqrt{4b^2\rho^4 + 4b^2\rho^6 - 8b^2\rho^5 + 2\rho^3 - 3\rho^2}}{2\rho - 3}. \quad (2.32)$$

The energy of such particles is

$$\mathcal{E} = \sqrt{1 - \frac{1}{\rho}} \sqrt{1 + \frac{(\ell - b\rho^2)^2}{\rho^2}}. \quad (2.33)$$

Figure 2.7 shows the angular velocity of the particle at a SCO as a function of  $\rho$  for different values of  $b$ . Similarly, for the Lamor particles we have

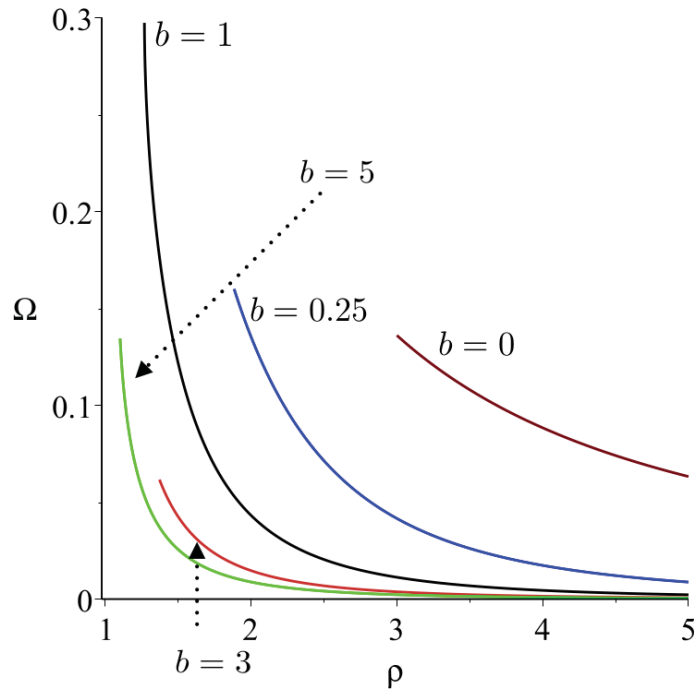


Figure 2.7: Angular velocity,  $\Omega$ , as a function of the radius,  $\rho$ , for different values of magnetic field,  $b$  for anti-Lamor particles. The dark red curve has  $b = 0$ , the blue curve has  $b = 0.25$ , the black curve has  $b = 1$ , the red curve has  $b = 3$ , and the green curve has  $b = 5$ .

$$l = \frac{-b\rho^2 - \sqrt{4b^2\rho^4 + 4b^2\rho^6 - 8b^2\rho^5 + 2\rho^3 - 3\rho^2}}{2\rho - 3}. \quad (2.34)$$

Figure (2.8) shows the angular velocity of the Lamor particle as a function of  $\rho$  for different values of  $b$ . Substituting expressions Eq. (2.32) or Eq. (2.34) and Eq.

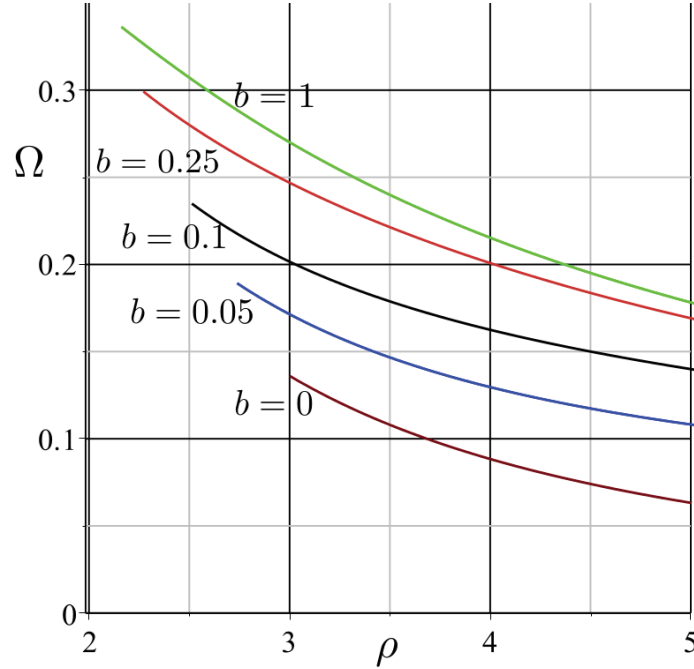


Figure 2.8: Angular velocity  $\Omega$  as a function of the radius,  $\rho$ , for different values of magnetic field,  $b$  for Lamor particles. The dark red curve has  $b = 0$ , the blue curve has  $b = 0.05$ , the black curve has  $b = 0.1$ , the red curve has  $b = 0.25$ , and the green curve has  $b = 1$ .

(2.33) into Eq. (2.31) we find the angular frequency  $\Omega$  as a function of  $\rho$  and  $b$ . In this expression, for a fixed value of the parameter  $b \geq 0$ , the specific energy  $\mathcal{E}$  and the parameter  $l$  are defined by the value of  $\rho$ , which corresponds to minimum of the effective potential.

For  $\rho$  greater than the ISCO radius this is a local minimum. If the specific energy is greater than the value of the potential at this minimum, the radial motion

is an oscillation between the minimal and maximal values of the radius. As a result the motion with negative  $l$  remains smooth, while for  $l > 0$  and large enough magnetic field  $b$  the particle trajectory becomes curly. One can describe such a trajectory as a result of superposition of cyclotron rotation along small cycles and a slow drift motion of the centre of the cycle around the black hole. As we explained earlier, one can expect that as a result of the synchrotron radiation such a trajectory would become more smooth and finally relax to a circular one. For more details concerning the general type of motion around magnetized black holes, see [68].

### 2.1.3 Innermost stable circular orbits (ISCO's)

The Innermost Stable Circular Orbit (ISCO) is defined by the condition that the first and second derivatives with respect to  $\rho$  of the effective potential are zero, ( $U_{,\rho} = 0$ ,  $U_{,\rho\rho} = 0$ ). Note that the lower sign below stands for Larmor particles and the upper sign stands for anti-Larmor particles. Moreover,  $\rho_+$  stands for anti-Larmor particles and  $\rho_-$  for the Larmor particles. From these two condition we can have the magnetic field as a function of radius,

$$b = \frac{(3 - \rho_{\pm})^{1/2}}{\sqrt{2}\rho_{\pm}H_{\pm}}, \quad (2.35)$$

where  $H_{\pm}$  is given as follows

$$H_{\pm} = \sqrt{4\rho_{\pm}^2 - 9\rho_{\pm} + 3 \pm \sqrt{(3\rho_{\pm} - 1)(3 - \rho_{\pm})}}. \quad (2.36)$$

Then, the angular momentum  $l$ , the energy  $\mathcal{E}$  and angular velocity  $\Omega$  are

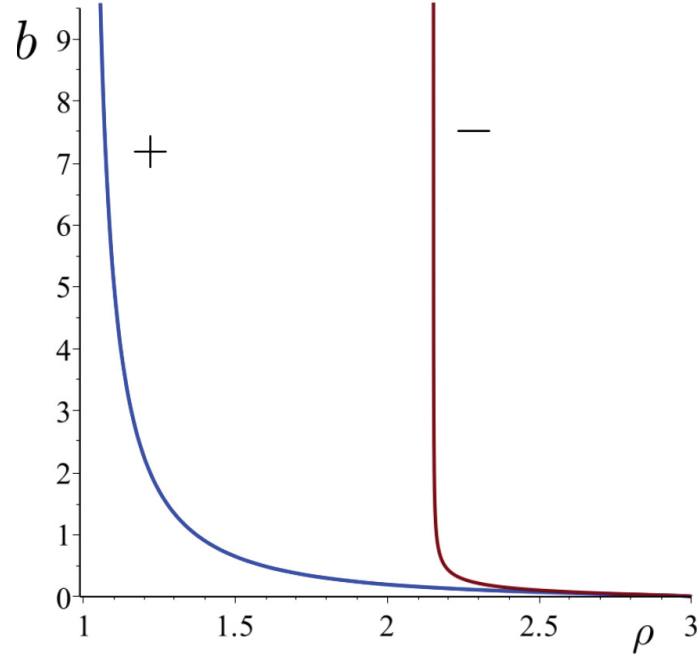


Figure 2.9: Magnetic field  $b$  of a magnetized black hole as a function of the ISCO radius  $\rho$ . Labels  $+$  and  $-$  stand for the anti-Larmor and Larmor orbit branches, respectively.

$$l_{\pm} = \pm \frac{\rho_{\pm}(3\rho_{\pm} - 1)^{1/2}}{\sqrt{2}H_{\pm}}, \quad (2.37)$$

$$\Omega_{\pm} = \pm \frac{\sqrt{2}}{2} \frac{\sqrt{3\rho_{\pm} - 1} \mp \sqrt{3 - \rho_{\pm}}}{J_{\pm}}, \quad (2.38)$$

$$\mathcal{E}_{\pm} = \sqrt{\frac{\rho_{\pm} - 1}{\rho_{\pm}} \frac{J_{\pm}}{H_{\pm}}}, \quad (2.39)$$

where

$$J_{\pm} = \sqrt{H_{\pm}^2 + \rho_{\pm} + 1 \mp \sqrt{3\rho_{\pm} - 1}\sqrt{3 - \rho_{\pm}}}. \quad (2.40)$$

Note that  $(5 + \sqrt{13})/4 < \rho_- \leq 3$  and  $1 < \rho_+ \leq 3$ . For  $b \geq 0$  and  $l \geq 0$ , the Lorentz force is toward the black hole, so we call this kind of motion Larmor motion. For

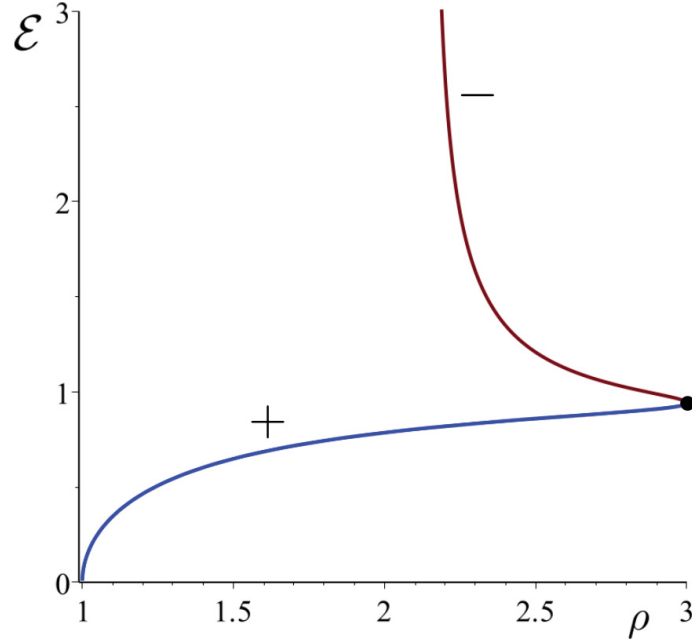


Figure 2.10: Specific energy  $\mathcal{E}$  of a charged particle at ISCO in a magnetized black hole as a function of the ISCO radius  $\rho$ . Labels + and - stand for the anti-Larmor and Larmor orbit branches, respectively.

$b \geq 0$  and  $l \leq 0$ , the Lorentz force is away from the black hole, so we call this kind of motion anti-Larmor motion. Figure 2.9 shows a relation between the value of the magnetic field and the radius  $\rho$  of the corresponding ISCO. Labels + and - stand for anti-Larmor and Larmor orbits, respectively. As we can see from the Figure 2.9 the anti-Larmor ISCO approaches the horizon of the black hole while energy is released. On the other hand, if one adds energy to a Larmor particle, then its radius is shifted to a smaller value. One might have expected that for the Larmor ISCO the radius would be shifted to a larger value, because the Lorentz force is attractive. However, from equation (2.31) we can see that in the case of Larmor particles  $l < 0$ , and since  $b > 0$  the expression inside the parenthesis is negative. Therefore, while we increase the magnetic field the angular velocity  $\Omega$  is

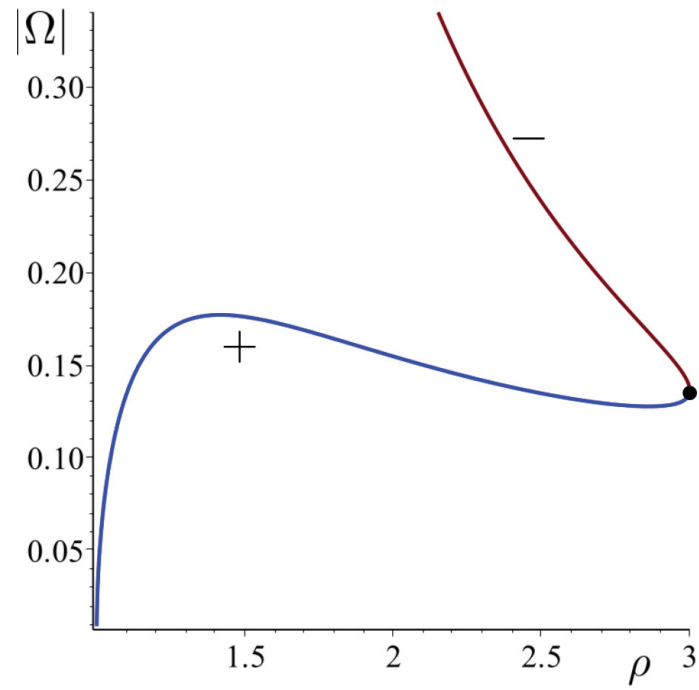


Figure 2.11: Angular velocity  $|\Omega|$  as a function of the ISCO radius in a magnetized black hole. Labels + and - stand for the anti-Larmor and Larmor orbit branches, respectively.

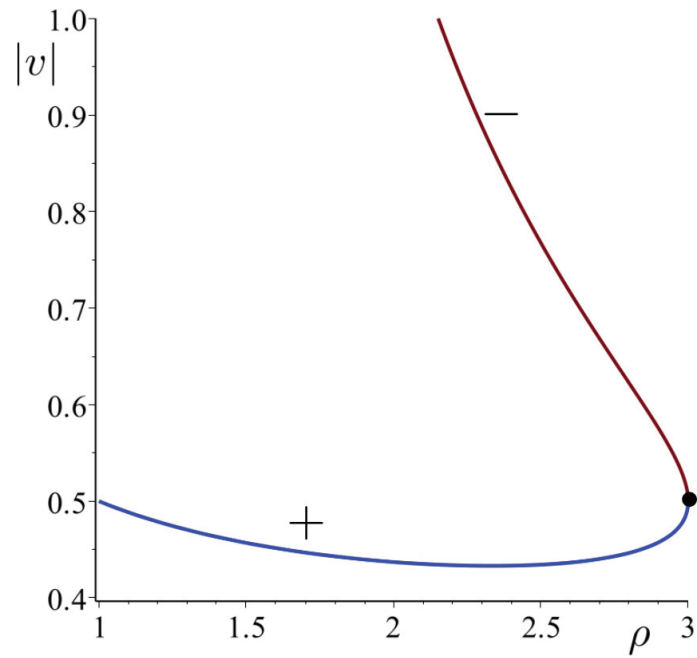


Figure 2.12: Velocity  $v$  of a charged particle at the ISCO in a magnetized black hole as a function of the ISCO radius  $\rho$ . Labels + and - stand for the anti-Larmor and Larmor orbit branches, respectively.

increasing. So, the Larmor particles come closer to the horizon of the black hole than the ISCO of Schwarzschild with no magnetic field.

The specific energy at the ISCO orbits as a function of the ISCO radius for both types (anti-Larmor and Larmor) of motion is presented in Figure 2.10. The next plot (Figure 2.11) shows the angular velocity at the ISCO,  $|\Omega|$ , as a function of its radius  $\rho$ . For small  $b$  ( $\rho \approx 3$ ) both branches  $+$  and  $-$  approach the same value  $\Omega_{\text{ISCO},b=0} = 1/\sqrt{54} \approx 0.136$ , which is the Keplerian ISCO angular velocity for a non-magnetized black hole.

The asymptotics of these functions for anti-Larmor ISCO and large  $b$  are

$$(\rho_+ - 1)|_{b \gg 1} = \frac{1}{\sqrt{3}b} + \dots, \quad (2.41)$$

$$\Omega_+|_{b \gg 1} = \frac{3^{3/4}}{6\sqrt{b}} + \dots, \quad (2.42)$$

$$\mathcal{E}_+|_{b \gg 1} = \frac{2}{3^{3/4}\sqrt{b}} - \frac{2}{3^{5/4}b^{3/2}} + \dots. \quad (2.43)$$

In the limit of a strong magnetic field ( $b \gg 1$ ),  $\Omega_+ \rightarrow 0$  (branch  $+$ ) and  $-\Omega_- \rightarrow 0.34$  (branch  $-$ ). Similar expressions can be easily obtained in the large  $b$  limit for Larmor orbits. For example, one has

$$\Omega_-|_{b \gg 1} = \Omega_-^{(0)} + \frac{\Omega_-^{(2)}}{b^2} + \mathcal{O}(b^{-4}), \quad (2.44)$$

$$\Omega_-^{(0)} = -\frac{\sqrt{6}}{18} \sqrt{3 + \sqrt{13}} (19 - 5\sqrt{13}) \approx -0.34, \quad (2.45)$$

$$\Omega_-^{(2)} = \frac{\sqrt{6}}{108} \sqrt{\frac{3 + \sqrt{13}}{13}} (7\sqrt{13} - 25) \approx 0.41. \quad (2.46)$$

### 2.1.4 Circular motion in the rest frame basis

Next, let us introduce a local rest frame  $\{\mathbf{e}_t, \mathbf{e}_\rho, \mathbf{e}_\theta, \mathbf{e}_\phi\}$

$$\mathbf{e}_t = |\xi_t^2|^{-1/2} \xi_t = f^{-1/2} \partial_t, \quad \mathbf{e}_\rho = f^{1/2} \partial_\rho, \quad (2.47)$$

$$\mathbf{e}_\theta = \rho^{-1} \partial_\theta, \quad \mathbf{e}_\phi = |\xi_\phi^2|^{-1/2} \xi_\phi = \frac{1}{\rho \sin \theta} \partial_\phi. \quad (2.48)$$

The four-vector of velocity for the circular motion, (2.30), with (dimensionless) angular velocity  $\Omega$  can be written as follows

$$u^\mu = \gamma \left( \xi_{(t)}^\mu + \Omega \xi_{(\phi)}^\mu \right) = \tilde{\gamma} (e_{(t)}^\mu + v e_{(\phi)}^\mu), \quad (2.49)$$

$$\gamma = \frac{1}{\sqrt{f - \Omega^2 \rho^2}}, \quad v = \frac{\Omega \rho}{\sqrt{f}}, \quad \tilde{\gamma} = \frac{\sqrt{f}}{\sqrt{f - \Omega^2 \rho^2}}. \quad (2.50)$$

Here  $v$  (which can be either positive or negative) is the velocity of the particle with respect to a rest frame, and  $\tilde{\gamma} = (1 - v^2)^{-1/2}$  is the corresponding Lorentz gamma factor. Moreover, we should recall that  $f = 1 - 1/\rho$ . A simple analysis shows that the velocity  $v$  at the anti-Larmor ISCO remains close to 1/2 in the entire interval (1, 3) of ISCO radii and, hence, this motion is not very relativistic. For the opposite direction of motion, the velocity for the ISCO changes from 1/2, in the absence of the magnetic field, up to 1 for a very large magnetic field (see Figure 2.12). For more details see [69].

## 2.2 Null rays in the Schwarzschild geometry

### 2.2.1 Conserved quantities and equations of motion

A distant observer receives information from an emitter revolving around the black hole by observing its radiation. Two different types of the observations are of the most interest: (1) Study of the images of the emitter orbits and (2) Study of the spectral properties of the observed radiation. The theoretical techniques required for these two problems are slightly different. However, in both cases one needs at first to perform similar calculations. Namely, one needs to integrate equations for the light propagation in the Schwarzschild geometry. This is a well studied problem. Many results concerning ray tracing as well as the study of the narrow spectral line broadening in the Schwarzschild spacetime can be found in the literature (see, e.g. [26] and references therein). Since the magnetic field does not affect the photon propagation, one can use similar techniques for our problem. However, there are two new features of the problem. Namely, (1) the radius of the emitter can be less than  $6M$ , the ISCO radius for a neutral particle, and (2) even if the charged emitter is at the same orbit as a neutral one, its angular velocity differs from the Keplerian velocity. For this reason one should perform the required calculations and adapt them to a new set-up of the problem.

The geodesic equation for a null ray is

$$\frac{Dp^\mu}{d\lambda} = 0, \quad g_{\mu\nu}p^\mu p^\nu = 0, \quad (2.51)$$

where  $p^\mu = dx^\mu/d\lambda \equiv \dot{x}^\mu$  and  $\lambda$  is an affine parameter. For the symmetries Eq.

(2.4-2.6) there exist three commuting integrals of motion

$$E = -p_\mu \xi_{(t)}^\mu = -p_t = f\dot{t}, \quad (2.52)$$

$$L_z = p_\mu \xi_{(\phi)}^\mu = p_\phi = \rho^2 \sin^2 \theta \dot{\phi}, \quad (2.53)$$

$$\begin{aligned} L^2 &= [p_\mu \xi_{(\phi)}^\mu]^2 + [p_\mu \xi_x^\mu]^2 + [p_\mu \xi_y^\mu]^2 \\ &= p_\theta^2 + \frac{p_\phi^2}{\sin^2 \theta} = \rho^4 (\dot{\theta}^2 + \sin^2 \theta \dot{\phi}^2). \end{aligned} \quad (2.54)$$

Let us recall that we use the dimensionless quantities. We choose the normalization of the affine parameter  $\lambda$  such that the “physical” energy is  $r_g E$ . In what follows, it is convenient to use the following quantities:

$$\zeta = \rho^{-1}, \quad \ell_z = \frac{L_z}{E}, \quad \ell = \frac{L}{E}, \quad \sigma = E\lambda. \quad (2.55)$$

### 2.2.2 Motion in the equatorial plane

The motion of a ray (as well as the motion of any particle) in the Schwarzschild geometry is planar. One can always choose this plane to coincide with the equatorial plane. For such a choice  $p_\theta = 0$  and  $L = |L_z|$ . Thus, the photon trajectory depends on only one conserved quantity,  $\ell_z = \ell$ . The equation of motion in the equatorial plane can be written in the following first order form:

$$\zeta' = -\epsilon \zeta^2 \mathcal{P}, \quad \mathcal{P} = \sqrt{1 - \ell^2 (1 - \zeta) \zeta^2}, \quad (2.56)$$

$$t' = 1/(1 - \zeta), \quad \phi' = \ell \zeta^2, \quad (\dots)' = d(\dots)/d\sigma. \quad (2.57)$$

For outgoing rays, when  $r$  increases along the trajectory,  $\epsilon = +1$ , and  $\epsilon = -1$  for incoming rays. For fixed value of the impact parameter  $\ell$ , the radial turning point

$\zeta_m$  (if it exists) is determined by the condition

$$(1 - \zeta_m)\zeta_m^2 = \ell^{-2}. \quad (2.58)$$

The evolution of the angle  $\phi$  along the trajectory can be found from the following equation:

$$\frac{d\phi}{d\zeta} = -\epsilon \frac{\ell}{\mathcal{P}}. \quad (2.59)$$

In what follows, we shall use the following function:

$$B(\ell; \zeta) = \int_0^\zeta \frac{d\zeta'}{\sqrt{\ell^{-2} - (1 - \zeta')\zeta'^2}}. \quad (2.60)$$

The integral Eq.(2.60) can be written in terms of the elliptic function of the first kind<sup>1</sup>  $F(x, \alpha)$ . One has

$$B(\ell, \zeta) = \frac{2\sqrt{2}\ell^{1/3}}{k_+} F\left(X(\zeta), \frac{k_-}{k_+}\right) \Big|_0^\zeta, \quad (2.61)$$

where

$$X(\zeta) = \frac{\sqrt{6}\sqrt{\ell^{2/3}(3\zeta - 1) + \sqrt{3}(c_+ + c_-)}}{3k_-}, \quad (2.62)$$

$$k_\pm = \sqrt{\sqrt{3}(c_+ + c_-) \pm i(c_+ - c_-)}, \quad (2.63)$$

$$c_\pm = \left[ \frac{\sqrt{3}(\frac{27}{2} - \ell^2)}{9} \pm \frac{\sqrt{27 - 4\ell^2}}{2} \right]^{1/3}. \quad (2.64)$$

---

<sup>1</sup> Here we use the definition

$$F(x, \alpha) = \int_0^x \frac{d\zeta}{\sqrt{1 - \zeta^2}\sqrt{1 - \alpha^2\zeta^2}}.$$

Consider a ray emitted at the radius  $r_e = r_g/\zeta_e$  that reaches infinity. Denote by  $\Phi$  the angle between the radial direction to the point of emission and the radial direction to the point of observation. It is easy to show that a null ray can have no more than one radial turning point since the effective potential<sup>1</sup> for null rays in Schwarzschild spacetime has only a local maximum and not a local minimum. The emitted ray either propagates to infinity with monotonic increase of  $\rho$ , or it at first moves to a smaller value of  $\rho$  and only after that goes to infinity. In the former case the bending angle is

$$\Phi = B(\ell, \zeta_e). \quad (2.67)$$

In the latter case one has

$$\Phi = 2B(\ell, \zeta_m) - B(\ell, \zeta_e). \quad (2.68)$$

Here  $\rho_m = \zeta_m^{-1}$  is the dimensionless radius of the radial turning point.

### 2.2.3 Integrals of motion and impact parameters

We are interested in the study of the propagation of photons emitted by an object revolving around a magnetized black hole in the plane orthogonal to the magnetic

---

<sup>1</sup> Let us rewrite the radial equation Eq. (2.69) of motion of null rays in Schwarzschild spacetime in terms of  $\rho$ :

$$\left(\frac{d\rho}{d\lambda}\right)^2 = E^2 - L^2 \frac{\rho - 1}{\rho^3} = E^2 - V^2(\rho), \quad (2.65)$$

so we define the effective potential for null rays in Schwarzschild spacetime as follows

$$V(\rho) = \sqrt{L^2 \frac{\rho - 1}{\rho^3}}. \quad (2.66)$$

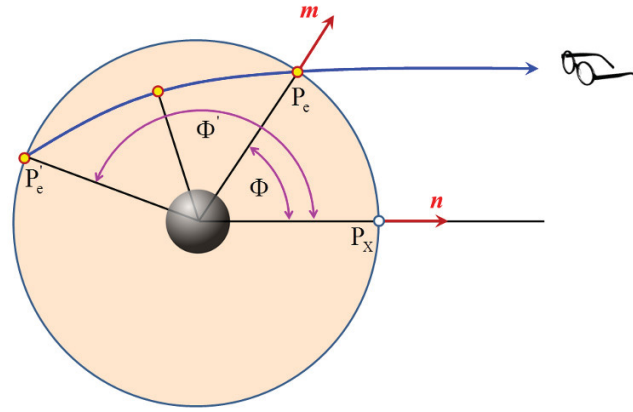


Figure 2.13: Motion of a photon in the equatorial plane. The photon emitted at  $P_e$  propagates to a distant observer along a trajectory without radial turning points (a direct ray). The ray emitted at  $P'_e$  is indirect. It at first moves toward the black hole, and only after it passes through a radial turning point does it propagate outward to the distant observer. The image is from [27]

field. Using the freedom in the rigid rotations, it is convenient to choose the spherical coordinates so that this plane coincides with the equatorial plane  $\theta = \pi/2$ . For such a choice, in the general case, the plane determined by the trajectory of the emitted photon will be tilted with respect to the equatorial one. There still remains freedom in rotation in the  $\phi$ -direction, preserving the plane connected with the charged particle motion, which we shall fix later.

To derive properties of such photons we write the corresponding equations

$$\zeta' = -\epsilon\zeta^2\mathcal{P}, \quad (2.69)$$

$$\theta' = \epsilon_\theta\zeta^2\sqrt{\ell^2 - \frac{\ell_z^2}{\sin^2\theta}}, \quad (2.70)$$

$$\phi' = \frac{\ell_z\zeta^2}{\sin^2\theta}, \quad t' = \frac{1}{1-\zeta}. \quad (2.71)$$

The turning points of the  $\theta$ -motion, where  $\theta' = 0$ , are determined by the condition  $\sin \theta = |\ell_z|/\ell$ . Denote these angles by  $0 < \theta_* \leq \pi/2$  and  $\pi - \theta_*$ . Denote by  $\iota$  the angle between the normal to the tilted plane and the normal to the equatorial plane. One has  $\iota = \pi/2 - \theta_*$ , so that  $0 \leq \iota < \pi/2$  and

$$\cos \iota = \frac{|\ell_z|}{\ell}. \quad (2.72)$$

In what follows, we will consider rays emitted by a revolving body which propagate to infinity, where an observer is located. In order to characterize the asymptotic properties of these rays which are directly connected with observations, one can proceed as follows. Denote by  $\theta_o$  and  $\phi_o$  the asymptotic angles for the ray trajectory. The angles of displacement of the photon in the  $\theta$  and  $\phi$  directions are  $\rho d\theta/dt$  and  $\rho \sin \theta d\phi/dt$  with respect to a photon in the radial direction and they give the angle of the photon as it reaches the distant observer. Multiplying them by  $\rho$  and taking the limit  $\rho \rightarrow \infty$ , one obtains the dimensionless impact parameters

$$\begin{aligned} \xi^\theta &= \lim_{\rho \rightarrow \infty} \left[ \rho^2 \frac{p^\theta}{p^t} \right] = \lim_{\zeta \rightarrow 0} \left[ \zeta^{-2} \frac{\theta'}{t'} \right] \\ &= \epsilon_\theta \sqrt{\ell^2 - \frac{\ell_z^2}{\sin^2 \theta_o}}, \end{aligned} \quad (2.73)$$

$$\begin{aligned} \xi^\phi &= - \lim_{\rho \rightarrow \infty} \left[ \rho^2 \sin \theta \frac{p^\phi}{p^t} \right] = - \lim_{\zeta \rightarrow 0} \left[ \zeta^{-2} \sin \theta \frac{\phi'}{t'} \right] \\ &= - \frac{\ell_z}{\sin \theta_o}. \end{aligned} \quad (2.74)$$

Consider a unit sphere with the coordinates  $(\theta, \phi)$  and denote a plane tangent to it at the point  $(\theta_o, \phi_o)$  by  $\Pi$ . We call it the *impact plane*. Denote by  $\mathbf{e}_\theta$  and  $\mathbf{e}_\phi$  unit vectors in  $\Pi$  directed along the coordinate lines of  $\theta$  and  $\phi$ , correspondingly.

We call the vector

$$\boldsymbol{\xi} = \xi^\theta \mathbf{e}_\theta + \xi^\phi \mathbf{e}_\phi \quad (2.75)$$

the *impact vector*. Its norm is

$$|\boldsymbol{\xi}| = \sqrt{(\xi^\theta)^2 + (\xi^\phi)^2} = \ell. \quad (2.76)$$

One also has

$$\tan \eta \equiv \xi^\phi / \xi^\theta = \frac{\epsilon_\theta \cos \iota \operatorname{sign}(\ell_z)}{\sqrt{\sin^2 \theta_o - \cos^2 \iota}}. \quad (2.77)$$

#### 2.2.4 Asymptotic data for null rays

For studying outgoing null rays it is convenient to rewrite the Schwarzschild metric Eq. (2.2) in the retarded time coordinates

$$ds^2 = \zeta^{-2} d\tilde{s}^2, \quad (2.78)$$

$$d\tilde{s}^2 = -\zeta^2 f du^2 + 2dud\zeta + d\Omega^2, \quad (2.79)$$

where  $du = dt - d\rho/f$ . The conformal metric, Eq. (2.79), is especially convenient for describing the asymptotic properties of null rays as  $r \rightarrow \infty$ . This metric is regular at infinity,  $\zeta = 0$ , so that the 3D surface  $\zeta = 0$  with the coordinates  $(u, \theta, \phi)$  is nothing but the future null infinity  $\mathcal{J}^+$  for our spacetime. Rays with the same asymptotic parameters  $(u_o, \theta_o, \phi_o)$  are asymptotically parallel in the ‘physical’ spacetime with the metric Eq. (2.78). To fix a ray in such a beam one needs two additional parameters, namely the impact vector Eq.(2.75). Thus, a point  $(u_o, \theta_o, \phi_o)$  at  $\mathcal{J}^+$  together with the impact vector  $\boldsymbol{\xi}$  uniquely specify a null ray which reaches infinity. We call these five parameters the *asymptotic data*.

Equations (2.69)-(2.71) are equivalent to the following set of equations:

$$\frac{d\theta}{d\zeta} = -\frac{\epsilon\epsilon_\theta}{\mathcal{P}} \sqrt{\ell^2 - \frac{\ell_z^2}{\sin^2 \theta}}, \quad (2.80)$$

$$\frac{d\phi}{d\zeta} = -\frac{\epsilon\ell_z}{\mathcal{P} \sin^2 \theta}, \quad (2.81)$$

$$\frac{du}{d\zeta} = -\frac{\epsilon\ell^2}{\mathcal{P}(1 + \epsilon\mathcal{P})}. \quad (2.82)$$

We recall that for the outgoing ray  $\epsilon = +1$ . For given position at  $\mathcal{J}^+$  and a given impact vector  $\boldsymbol{\xi}$ , one can determine the integrals of motion  $\ell_z$  and  $\ell$ . For given asymptotic data one can integrate equations (2.80)–(2.82) back in time, from the starting point  $\zeta = 0$ , and restore the complete null ray trajectory.

## Chapter 3

# Imaging the radiation

In chapter two we discussed how the magnetic field changes the orbits of charged particles. In this chapter we will present the implications of such modifications. We start by imaging the modified orbits of the charged particle around a weakly magnetized black hole. We will study the angular relations and the map between the equatorial and the impact planes. We close the section 3.1 of this chapter with a classification of rays as direct or indirect. In section 3.2, we study the effect of the magnetic field on the spectral broadening starting with the momentum of the photons and the conserved quantities, the redshift factor that we take into account in our case. We will continue our study with the calculation of the solid angle of the emitted photons that pass through the “telescope” aperture of the observer and the study of the spectral broadening for a single emitter. We are not discussing the finite ring case in this thesis because that would require the choice of a specific model for charged particles distribution around the black hole. We close the chapter with a discussion of the general properties of the spectral function.

## 3.1 Orbit images

In this section, we study the imaging of the modified orbits of the charged particle around a weakly magnetized black hole. We will start by studying the angular relations and the map between the equatorial and the impact planes. We close section 3.1 with the classification of rays into those with or without a radial turning points (i.e., direct and indirect rays).

### 3.1.1 Angular relations

Denote by  $P_e = (t_e, \rho_e, \theta = \pi/2, \phi = \varphi(t_e))$ ,  $\varphi \in (-\pi, \pi]$ , an event of the radiation of a quantum by the emitter revolving around the black hole. This quantum is registered by a distant observer (at  $\mathcal{J}^+$ ) with location  $P_o = (u_o, \zeta_o = 0, \theta_o, \phi_o)$ . Here  $u_o$  is the moment of the retarded time when the ray arrives at the observer, and  $\theta_o$  is the angle between his/her position and the direction orthogonal to the plane  $\theta = \pi/2$ . We use the freedom of rigid rotations around the  $Z$ -axis to put the angle  $\phi_o$  at the point of observations equal to zero.

For a discussion of the photons trajectories, it is convenient to use a unit round sphere shown in Figure 3.1, which allows one to represent the motion of photons and the emitter in the 2D  $(\theta, \phi)$ -sector. We embed this sphere in a flat 3D Euclidean space, so that a point on the surface of the sphere is uniquely determined by a unit vector with the origin at the centre of the sphere. We call this 2D space the *angular space*. The motion of the emitter is represented by the equator of the sphere, while orbits of photons, since they are planar, are represented by great circles. We use the same letters  $P_e$  and  $P_o$  as earlier to denote the positions of the emission and of the observer location in the angular space.

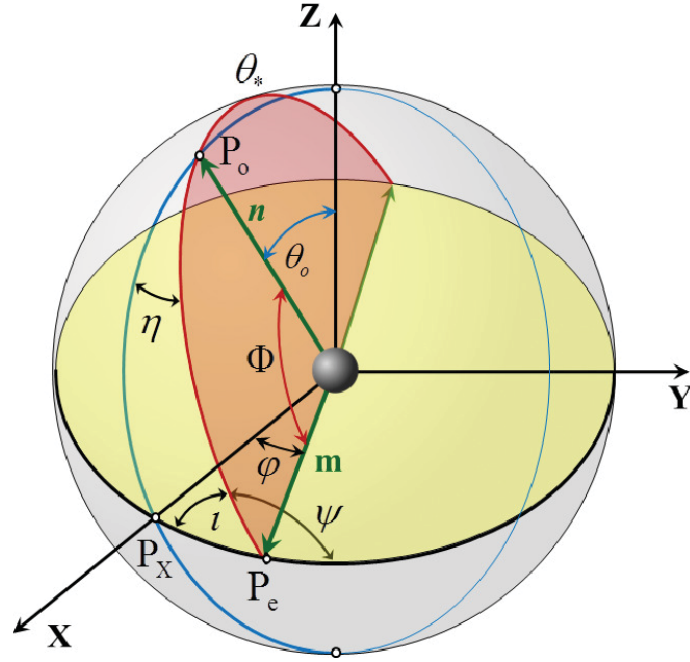


Figure 3.1: Angular definitions. The image is from [27]

A trajectory of the photon emitted at  $P_e$  and arriving to the observer  $P_o$  is represented by a great circle passing through these two points (see Figure 3.1). We denote by  $\Phi$  the angle between the vectors  $\vec{n}$  and  $\vec{m}$  from the centre of the unit sphere to the points  $P_o$  and  $P_e$ , respectively. We call  $\Phi$  the *bending angle*. It varies from  $\pi/2 - \theta_o$  when  $\varphi = 0$  to  $\pi/2 + \theta_o$  when  $\varphi = \pi$ . We call such rays with  $\Phi \in [\pi/2 - \theta_o, \pi/2 + \theta_o]$  *primary* to distinguish them from *secondary* rays, which make one or more turns around the black hole before they reach the observer. The characteristic property of these rays is that after the emission they move at first below the equatorial plane. The brightness of the secondary images generated by such rays is greatly suppressed. That is why we do not consider them here.

As one can see from Figure 3.1, the angle  $\theta$  for the primary rays emitted in the interval  $\varphi \in [-\pi/2, \pi/2]$  monotonically decreases from the point of emission

to  $P_o$ . For the rays emitted from the other part of the circle the angle  $\theta$  at first decreases. It increases after passing through its minimal value (an angular turning point  $\theta_*$ ). Equation (2.73) implies that in the former case the coordinate of the image on the impact plane is  $\xi^\theta \leq 0$ , while for the latter one  $\xi^\theta > 0$ . This means that the image of the part of the emitter trajectory lying in the half-plane with positive  $X$  is located in the lower half of the impact plane  $\xi^\theta < 0$ , while the part with  $X < 0$  has the image in the upper half of the impact plane  $\xi^\theta > 0$ . Two points with  $\xi^\theta = 0$  are images of the radiation sent by the emitter when it crosses the  $Y$ -axis, where  $\varphi = \pm\pi/2$ . We denote by  $\psi$  the angle between the direction of the non-radial part of the initial photon direction and the 3-velocity of the emitter in the static frame of the black hole. The angle  $\psi$  is connected with the angle  $\iota$  [see Eq.(2.72)] as follows:  $\iota = \pi - \psi$ .

A simple way to find relations between angles which will be used later is to consider a spherical triangle on a unit sphere. Denote by  $A$ ,  $B$  and  $C$  its angles, and by  $a$ ,  $b$  and  $c$  the length of the sides of the triangle, opposite to  $A$ ,  $B$  and  $C$ , respectively. Then, one has

$$\frac{\sin A}{\sin a} = \frac{\sin B}{\sin b} = \frac{\sin C}{\sin c}, \quad (3.1)$$

$$\cos a = \cos b \cos c + \sin b \sin c \cos A. \quad (3.2)$$

For example, consider the spherical triangle  $P_X P_e P_o$  (see Figure 3.1). It has the angles  $\pi/2$  (at  $P_X$ ),  $\pi - \psi$  (at  $P_e$ ) and  $\eta$  (at  $P_o$ ). The length of the sides opposite to the apexes  $P_X$ ,  $P_o$ , and  $P_e$  of this triangle are  $\Phi$ ,  $\pi/2 - \theta_o$ , and  $\varphi$ , respectively.

Using Eq.(3.1) and Eq.(3.2), one obtains

$$\cos \Phi = \cos \varphi \sin \theta_o, \quad \sin \psi = \frac{\cos \theta_o}{\sin \Phi}, \quad \sin \eta = \frac{\sin \varphi}{\sin \Phi}. \quad (3.3)$$

These equations together with the expressions Eq.(2.73)–Eq.(2.75) allow one to determine the impact vector  $\vec{\xi}$  in terms of the total angular momentum  $\ell$ , the inclination angle  $\theta_o$  and the position angle  $\varphi$  of the emitter:

$$\xi^\phi = \frac{\ell \sin \varphi}{\sin \Phi}, \quad (3.4)$$

$$\xi^\theta = \frac{\ell \cos \varphi \cos \theta_o}{\sin \Phi}. \quad (3.5)$$

One also has

$$\ell_z = -\frac{\ell \sin \theta_o \sin \varphi}{\sin \Phi}, \quad (3.6)$$

$$\sin \Phi = \sqrt{\sin^2 \varphi + \cos^2 \theta_o \cos^2 \varphi}. \quad (3.7)$$

These relations, besides the inclination angle  $\theta_o$  of the orbit and the angular position of the emitter,  $\varphi$ , contain only one unspecified parameter  $\ell$ .

### 3.1.2 Map between equatorial and impact planes

Consider a ray connecting a point  $P_e$  on the equatorial plane and a distant observer  $P_o$ . If such a ray does not have a radial turning point between the point of emission and the point of observation we call it *direct*. In the opposite case we call it an *indirect* ray (see Figure 2.13). Now we can make a classification of four classes or domains of null rays (photon trajectories) that reach  $\mathcal{J}^+$  (future null infinity).

The first class of rays (domain  $I$  in Figure 3.2) have sufficiently small angular momentum parameters  $\ell$  and  $\ell_z$  (depending on  $\theta_o$ ) that, when traced backward in time from the observer whose location  $P_o$  is idealized to be  $\mathcal{J}^+$ , do not cross the equatorial plane at all before they approach very close to the horizon of the black hole. Since the emitters are assumed to be on the equatorial plane, none of the rays to  $P_o$  from an emitter can be in domain  $I$ . (They are thus neither direct rays nor indirect rays, since those are defined to be rays from the emitter on the equatorial plane to the distant observer.)

The second class of rays (domain  $II$  in Figure 3.2) have somewhat greater angular momentum parameters  $\ell$  and  $\ell_z$ , so that when traced backward in time from  $P_o$ , they do intersect the equatorial plane, but they have  $\ell < \ell_* = 3\sqrt{3}/2$ , so that they approach very near to the black hole horizon without any radial turning points. Since these rays have  $\rho$  increasing monotonically (in the forward direction of time), they are one of two classes of direct rays.

The third class of rays (domain  $III$ ) have  $\ell > \ell_* = 3\sqrt{3}/2$  but no turning points between the emitter and the observer, so they are the second class of the direct rays. However, the fact that  $\ell > \ell_*$  means that if one traces these rays backward in time from the emitter, they do have a turning point and eventually go to  $\mathcal{J}^-$  (past null infinity). (These rays might also cross the equatorial plane another time, but here we shall assume that when tracing a ray backward in time from the observer, the emitter is on the first crossing of the equatorial plane.)

The fourth class of rays (domain  $IV$ ) also have  $\ell > \ell_* = 3\sqrt{3}/2$  but do have turning points between the emitter and the observer, so that they are indirect rays. That is, when one of these rays is traced backward in time from the observer, at first  $\rho$  decreases, but then at the turning point  $\rho$  begins increasing before the ray

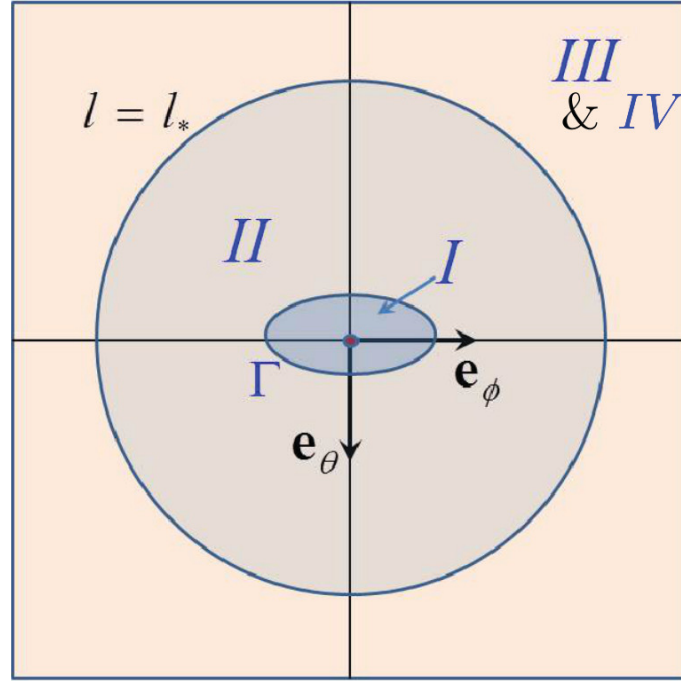


Figure 3.2: Schematic diagram of the impact plane. The horizontal axis corresponds to the  $\phi$  coordinate and the vertical axis corresponds to the  $\theta$  coordinate. The image does not distinguish between the domain *III* and *IV*. The image is from [27]

reaches the emitter. In the forward direction of time, when a photon is emitted by the emitter, it initially has  $\rho$  decreasing, so  $\epsilon = -1$  there in the radial equation (2.69). (In contrast, at emission  $\epsilon = +1$  for photons in domain *III*.)

The combined region with  $\ell > \ell_* = 3\sqrt{3}/2$ , domain *III* and *IV*, is what is depicted without distinction by the outer region of Figure 3.2.

Using Eq. (2.67) one can find the boundary between the regions *I* and *II* from the following relation:

$$B(\ell, 1) = \Phi(\varphi, \theta_o) = \arccos(\cos \varphi \sin \theta_o). \quad (3.8)$$

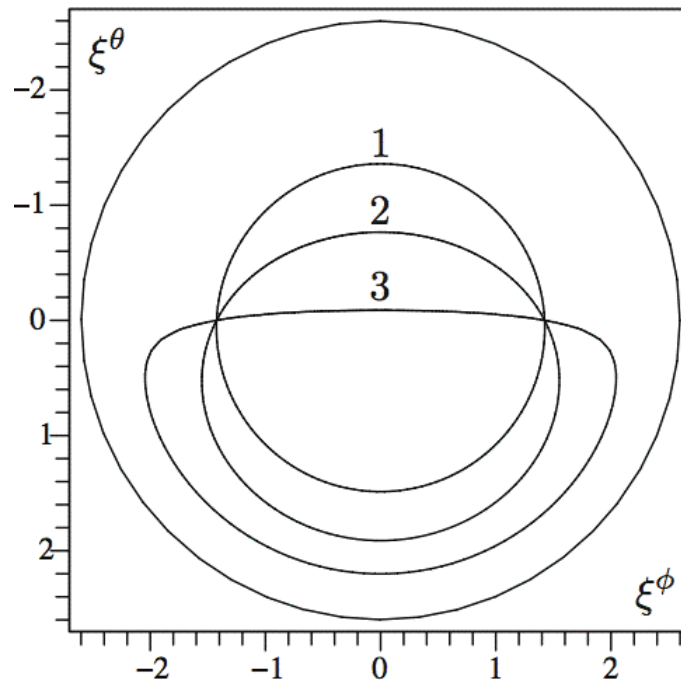


Figure 3.3: The boundary  $\Gamma$  between the regions  $I$  and  $II$  for different values of the observer's angle  $\theta_o$ : Curve 1:  $\theta_o = 5^\circ$ ; Curve 2:  $\theta_o = 45^\circ$ ; Curve 3:  $\theta_o = 85^\circ$ . A great circle is a curve  $|\xi| = \ell_* = 3\sqrt{3}/2$ .

(Let us recall that the rays in this domain do not have a radial turning point.) Figure 3.3 presents solutions of this equation for different values of the inclination angle  $\theta_o$ .

Let us summarize this part. For a fixed position of the observer at infinity ( $\theta_o, \phi_o = 0$ ) and a fixed moment of arrival of the rays  $u_o$  there exist a one-to-one correspondence between the region  $II \cup III \cup IV$  of the impact plane and the region of the equatorial plane, located outside the black hole. We call this map  $\Psi$

$$\Psi : \xi \rightarrow (\zeta < 1, \theta = \pi/2, \phi). \quad (3.9)$$

### 3.1.3 Direct and indirect rays

If the radius of an emitter is  $\rho \leq 3/2$ , all the rays from it to the distant observer are direct, with  $\rho$  increasing monotonically. For an emitter with any  $\rho > 3/2$ , there are indirect rays from it which initially have  $\rho$  decreasing but then have a turning point at a smaller  $\rho$  (but still greater than  $3/2$ ) before traveling to arbitrarily large  $\rho$ . However, for a range of  $\rho$  outside of  $3/2$ , all of the indirect rays from a particular emitter on the equatorial plane to a particular distant observer cross the equatorial plane at another location after leaving the emitter. If there is an optically thick accretion disk on the equatorial plane, these indirect rays will be absorbed and not reach the observer. And even if the disk is optically thin, the fact that these indirect rays bend around the black hole by a greater angle before reaching the observer than the direct rays do means that they have a greater divergence and hence contribute less to the flux received by the observer. Therefore, we shall henceforth exclude the indirect rays that after leaving the equatorial plane reach it again and cross it before traveling to the distant observer.

If the radius of the emitter orbit is small enough all the rays from it to the distant observer are direct. For a dimensionless radius  $\rho$  larger than the critical radius  $\rho_* = 1/\zeta_*$  there exists a value  $|\varphi_*| \geq \pi/2$  of the angle  $\varphi$  such that for  $-\varphi_* < \varphi < \varphi_*$  one has only direct rays, while for  $\pi > \varphi > \varphi_*$  and  $-\pi < \varphi < -\varphi_*$  the rays are indirect. We denote the critical inverse radius which separates these two cases by  $\zeta_*$ . For  $\zeta_e = \zeta_*$  a radial turning point is located at  $\varphi_* = \pi$  on the equatorial plane. For this case one has

$$\Phi = \Phi_*(\theta_o) = \pi/2 + \theta_o. \quad (3.10)$$

The critical value  $\zeta_*$  is a function of the inclination angle  $\theta_o$ . To find it let us first replace in Eq. (2.60)  $\ell^{-2}$  by  $(1-z)z^2$ . Then we denote by  $C(z)$  the following integral

$$C(z) = \int_0^z \frac{d\zeta}{\sqrt{(1-z)z^2 - (1-\zeta)\zeta^2}}. \quad (3.11)$$

By change of the variable  $\zeta = z(1-y^2)$  this integral can be rewritten in the form

$$C(z) = 2 \int_0^1 \frac{dy}{\sqrt{Z}}, \quad Z = 2 - y^2 - 3z + 3zy^2 - zy^4. \quad (3.12)$$

Figure 3.4 shows a plot of this function.

The function  $\zeta_*(\theta_o)$  is determined by the relation

$$C(\zeta_*) = \Phi_* = \pi/2 + \theta_o. \quad (3.13)$$

From the Eqs. (2.60), (2.67) and (3.13) we can find the relation between  $\ell$  and  $\theta_o$ . The plot of  $\zeta_*(\theta_o)$  is shown in Figure 3.5.  $\zeta_*$  monotonically increases from 0

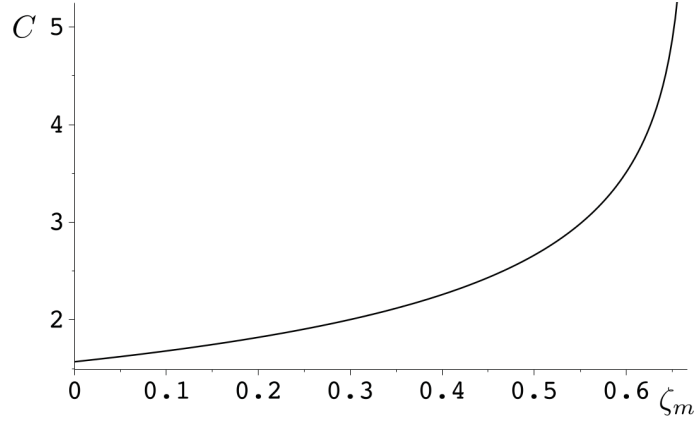


Figure 3.4: Function  $C(z)$ . It monotonically grows with  $z$  from  $\pi/2$  at  $z = 0$  and becomes infinite at  $z = 2/3$ .

(at  $\theta_o = 0$ ) to its maximal value at  $\theta_o = \pi/2$  equal to

$$\zeta_{*,max} \approx 0.5680820870. \quad (3.14)$$

Consider now a circular orbit with  $\zeta_e < \zeta_*$ . The following equation determines an angle  $\varphi_*$  on such an orbit which separates its two parts (with direct and indirect rays):

$$\varphi_* = \arccos \left( \frac{\cos(C(\zeta_e))}{\sin \theta_o} \right). \quad (3.15)$$

It is convenient to combine the relations Eq. (2.67) and Eq. (2.68). We introduce the functions  $B_{\pm}(\ell, \zeta_e)$  which are defined as follows:

$$B_+(\ell, \zeta_e) = B(\ell, \zeta_e), \quad B_-(\ell, \zeta_e) = 2C(\zeta_m(\ell)) - B(\ell, \zeta_e), \quad (3.16)$$

where  $\zeta_m$  is defined by Eq. (2.58),  $(1 - \zeta_m)\zeta_m^2 = \ell^{-2}$ , and the function  $C$  is defined by Eq. (3.12). Note that for numerical computations of  $B_-(\ell, \zeta_e)$  it is more convenient

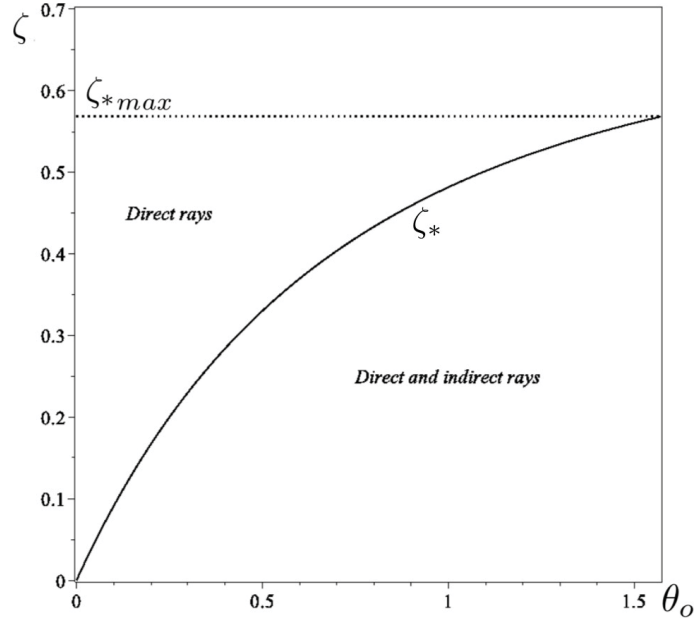


Figure 3.5: The critical inverse radius  $\zeta_*$  as a function of the inclination angle  $\theta_o$ .

to consider  $\zeta_m$  as a parameter.

The following equation,

$$B_{\pm}(\ell, \zeta_e) = \Phi \equiv \arccos(\cos \varphi \sin \theta_o), \quad (3.17)$$

establishes a relation between the position (angle  $\varphi$ ) of the emitter on the orbit with the inverse radius  $\zeta_e$  and the angular momentum  $\ell$  of the photon that reaches a distant observer with the inclination angle  $\theta_o$ . In this relation one needs to choose the sign  $+$  for a direct trajectory and  $-$  for an indirect one.

The corresponding image on the impact plane can be found by using Eq. (3.4) and Eq. (3.5). By integrating Eq. (2.82), one obtains a relation between the time of emission,  $t_e$ , and the retarded time of observation,  $u_o$ , at  $\mathcal{J}^+$ .

In the conclusion of this section let us give examples of the images of orbits on

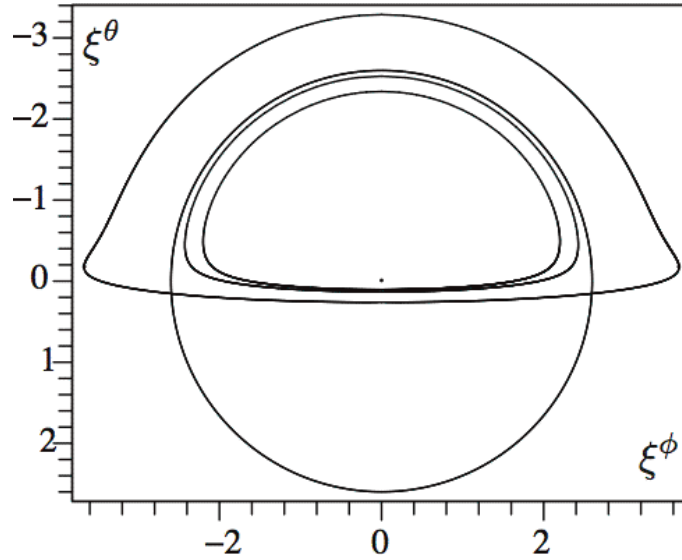


Figure 3.6: Images of some orbits corresponding to  $\theta_o = 85^\circ$ . The innermost curve is the image of the  $\zeta_e = 5/6$  orbit. The next curve is the image of the  $\zeta_e = 2/3$  orbit. And the outermost curve is the image of the  $\zeta_e = 1/3$  orbit. The circle represents the rim of the black hole shadow. Note that the angle  $\theta_o$  is increasing from the axis of the black hole to the equatorial plane.

the impact plane. These images for the inclination angles  $\theta_o = 5^\circ$ ,  $\theta_o = 45^\circ$  and  $\theta_o = 85^\circ$  and the inverse radius of the orbit equal to  $\zeta_e = 5/6, 1/3$  are shown in Figures 3.6, 3.7, 3.8, 3.9 and 3.10. In the figures 3.6 we have an extra case where the inverse radius of the orbit equal to  $\zeta_e = 2/3$ .

By comparing Figures 3.7-3.10 with Figure 3.6 one can see that while the inclination angle is getting smaller the images of the orbit become more circular. In Figures 3.6-3.10 the circle of radius 2.598 represents the rim of the black hole shadow. Counter-intuitively we see images of the orbit from inside the circle of radius 2.598. The rim of the black hole shadow is the light rays that barely escape the black hole. On the other hand, the light rays that come from the emitter (revolving near the black hole) due to the bending of light appear that they are

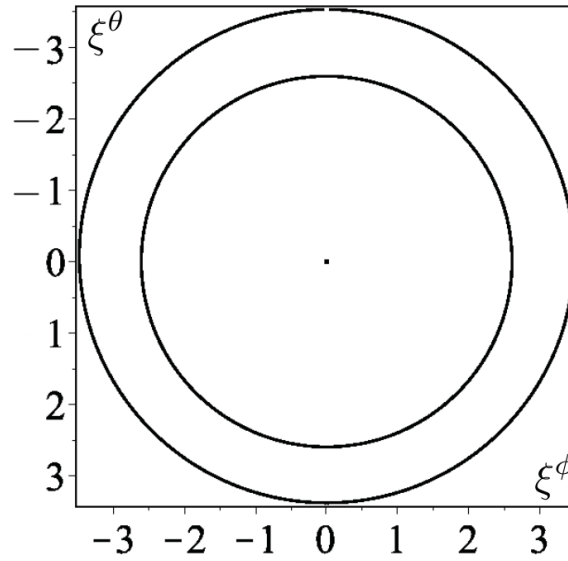


Figure 3.7: Image corresponds to  $\theta_o = 5^\circ$ . The inner circle represents the rim of the black hole shadow. The outer circle is the image of the  $\zeta_e = 1/3$  orbit.

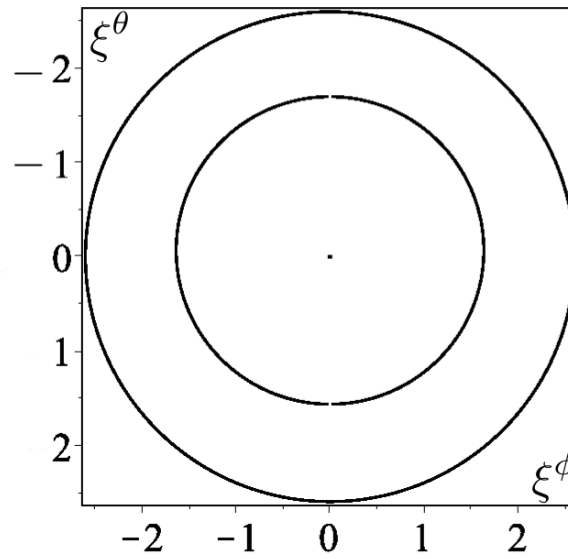


Figure 3.8: Image corresponds to  $\theta_o = 5^\circ$ . The outer circle represents the rim of the black hole shadow. The inner circle is the image of the  $\zeta_e = 5/6$  orbit.

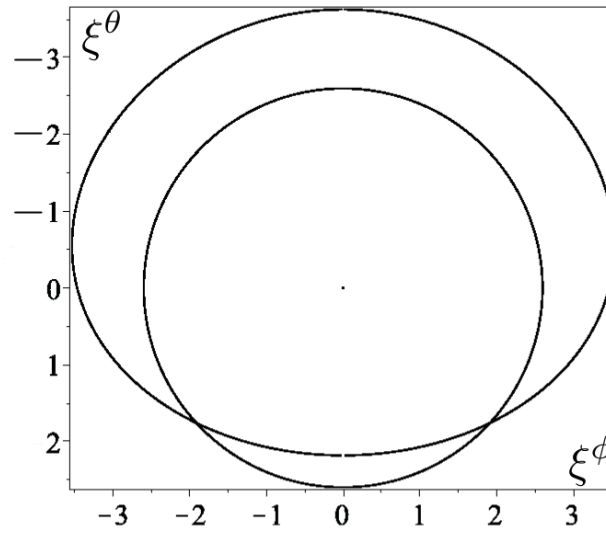


Figure 3.9: Image corresponds to  $\theta_o = 45^\circ$ . The circle represents the rim of the black hole shadow. The deformed curve is the image of the  $\zeta_e = 1/3$  orbit.

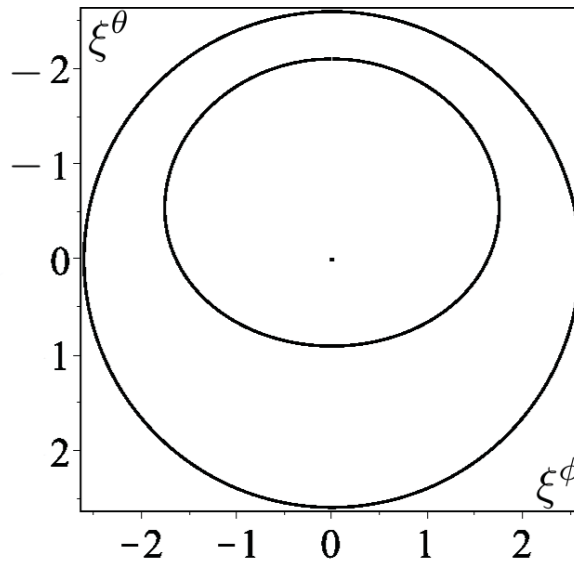


Figure 3.10: Image corresponds to  $\theta_o = 45^\circ$ . The circle represents the rim of the black hole shadow. The deformed curve is the image of the  $\zeta_e = 5/6$  orbit.

coming from the black hole and they create a circle (or in general shapes) with radius smaller than the black hole shadow.

## 3.2 Spectral broadening

In this section, we study the effect of the magnetic field on the spectral broadening of the radiation from a charged emitter revolving around the black hole. We close the chapter with a discussion of the general properties of the spectral function.

### 3.2.1 Photon momentum and conserved quantities

In what follows, we use the following orthonormal tetrad at rest at the point of emission  $P_e$ :

$$\{\mathbf{e}_t, \mathbf{e}_\rho, \mathbf{e}_\Phi, \hat{\mathbf{e}}\}. \quad (3.18)$$

The first of the vectors,  $\mathbf{e}_t$ , is in the direction of the Killing vector  $\xi_{(t)}$ . The second vector  $\mathbf{e}_\rho$  is along the radial direction, while the last two vectors are tangent to the surface  $t = \text{const}$  and  $\rho = \text{const}$ . We choose  $\mathbf{e}_\Phi$  to lie in the photon orbit plane and directed from the point of emission  $P_e$  to the point of observation  $P_o$ . The last vector  $\hat{\mathbf{e}}$  is uniquely defined by the condition that the tetrad Eq.(3.18) is right-hand oriented. The unit vector  $\mathbf{e}_\phi$  in the equatorial plane and tangent to the orbit of the emitter can be written in the form

$$\mathbf{e}_\phi = -\frac{1}{\sin \Phi} (\sin \theta_o \sin \varphi \mathbf{e}_\Phi + \cos \theta_o \hat{\mathbf{e}}), \quad (3.19)$$

where

$$\hat{\mathbf{e}} = \frac{1}{\sin \Phi} (\sin \varphi \cos \theta_o, -\cos \varphi \cos \theta_o, -\sin \varphi \sin \theta_o). \quad (3.20)$$

Consider a photon with the impact parameter  $\ell$ . Denote by  $\Gamma$  the plane of its orbit, and by  $\boldsymbol{\xi}_{(\Phi)}$  the Killing vector generating rotations preserving  $\Gamma$ . Then the momentum of the photon at the moment when it passes the radius  $\rho$  can be written in the form

$$\mathbf{p} = \nu(\boldsymbol{\xi}_{(t)} + a\mathbf{e}_\rho + b\boldsymbol{\xi}_{(\Phi)}). \quad (3.21)$$

One has

$$\omega_o = -(\mathbf{p}, \boldsymbol{\xi}_{(t)}) = \nu f, \quad (3.22)$$

$$L = (\mathbf{p}, \boldsymbol{\xi}_{(\Phi)}) = \nu b \zeta^{-2}. \quad (3.23)$$

Thus, one has

$$\ell = \frac{L}{\omega_o} = \frac{b}{\zeta^2 f}. \quad (3.24)$$

The quantity  $\omega_o$  is the frequency of the photon at infinity, measured in  $r_g^{-1}$  units.

Using these relations and the property  $\mathbf{p}^2 = 0$  one finds

$$\mathbf{p} = \omega_o \left( \frac{1}{\sqrt{f}} \mathbf{e}_t + \frac{1}{\sqrt{f}} \mathcal{P} \mathbf{e}_\rho + \ell \zeta \mathbf{e}_\Phi \right), \quad (3.25)$$

where, as earlier,  $\mathcal{P} = \sqrt{1 - \ell^2 \zeta^2 f}$ .

### 3.2.2 Photon beam from the emitter

Using Eq. (3.25), one finds the emitted frequency is

$$\omega_e = -p_\mu u^\mu = \gamma_e \omega_o \left[ \frac{1}{\sqrt{f}} - v \ell \zeta (\mathbf{e}_\phi, \mathbf{e}_\Phi) \right], \quad (3.26)$$

where  $\omega_o = -p_\mu \xi_{(t)}^\mu$  is the observer frequency and where  $\gamma_e$  is  $\gamma$  defined by Eq. (2.50) with  $f = f_e = 1 - 1/\rho_e$ . Using Eq. (3.19), one can write

$$(\mathbf{e}_\phi, \mathbf{e}_\Phi) = -\frac{\sin \varphi \sin \theta_o}{\sin \Phi}. \quad (3.27)$$

Combining these results we obtain the following relation between the emitted frequency  $\omega_e$  and the frequency  $\omega_o$  registered by a distant observer:

$$\omega_o = \omega_e \frac{\sin \Phi \sqrt{f_e - \Omega^2 \rho_e^2}}{(\sin \Phi + \ell \Omega \sin \theta_o \sin \varphi)}. \quad (3.28)$$

We denote the ratio  $\omega_e/\omega_o$  by

$$\alpha = \gamma_e \left( 1 + \frac{\ell \Omega \sin \varphi \sin \theta_o}{\sin \Phi} \right). \quad (3.29)$$

### 3.2.3 Solid angle at the emitter

We recall that the photon orbit is planar. We call the corresponding plane the *photon plane*. We choose a reference photon emitted to the distant observer. In order to find the solid angle of the emitted photons that pass through the ‘telescope’ aperture we fix the position of the emitter and consider a bundle of emitted photons with momenta that slightly differ from the momentum  $\mathbf{p}$  of the reference photon. To determine the bundle we consider two types of variations, which do not involve the trivial conformal variation of  $\omega_o$ . The first one is the variation  $\delta \ell$  of the angular momentum  $\ell$  which does not change the photon plane,

$$\delta_\ell \mathbf{p} = \omega_o \delta \ell \mathbf{Z}, \quad \mathbf{Z} = -\frac{\ell \zeta^2 \sqrt{f}}{\mathcal{P}} \mathbf{e}_\rho + \zeta \mathbf{e}_\Phi. \quad (3.30)$$

The second variation  $\delta\psi$  changes the position of the photon plane and slightly rotates it around the direction to the emitter by an angle  $\delta\psi$ . As a result of this rotation, the vectors  $\mathbf{e}_\Phi$  and  $\hat{\mathbf{e}}$  are transformed as follows:

$$\delta_\psi \mathbf{e}_\Phi = \hat{\mathbf{e}} \delta\psi, \quad \delta_\psi \hat{\mathbf{e}} = -\mathbf{e}_\Phi \delta\psi. \quad (3.31)$$

Hence

$$\delta_\psi \mathbf{p} = \omega_o \ell \zeta_e \hat{\mathbf{e}} \delta\psi. \quad (3.32)$$

To find the solid angle  $\Delta\Omega_e$  for such a beam we shall use the relation (B.7) and write it in the form

$$\mathcal{A} = \pm \Delta\Omega_e \mathbf{E}, \quad (3.33)$$

where  $\mathbf{E}$  is the Levi-Civita tensor, the unit rank-4 totally skew-symmetric tensor, and

$$\mathcal{A} = \omega_e^{-3} \mathbf{u} \wedge \mathbf{p} \wedge \delta_\ell \mathbf{p} \wedge \delta_\psi \mathbf{p}. \quad (3.34)$$

Using equations (3.30), (3.31) and (3.34) one obtains

$$\mathcal{A} = \gamma \ell \zeta_e \left( \frac{\omega_o}{\omega_e} \right)^3 \delta \ell \delta \psi (\mathcal{B} + v \mathcal{C}), \quad (3.35)$$

$$\mathcal{B} = \omega_o^{-1} \mathbf{e}_t \wedge \mathbf{p} \wedge \mathbf{Z} \wedge \hat{\mathbf{e}}, \quad (3.36)$$

$$\mathcal{C} = \omega_o^{-1} \mathbf{e}_\varphi \wedge \mathbf{p} \wedge \mathbf{Z} \wedge \hat{\mathbf{e}}. \quad (3.37)$$

Calculations give

$$\mathcal{B} = \frac{\zeta_e}{\sqrt{f_e} \mathcal{P}} \mathbf{E}, \quad \mathcal{C} = \frac{\ell \zeta_e^2 \sin \theta_o \sin \varphi}{\mathcal{P} \sin \Phi} \mathbf{E}, \quad (3.38)$$

where

$$\mathbf{E} = \mathbf{e}_t \wedge \mathbf{e}_\rho \wedge \mathbf{e}_\Phi \wedge \hat{\mathbf{e}}. \quad (3.39)$$

Thus one has

$$\Delta\Omega_e = \frac{\ell\zeta_e^2}{\alpha^2\mathcal{P}}\delta\ell\delta\psi. \quad (3.40)$$

### 3.2.4 Spectral broadening

If there are no caustics, all the photons of the bundle emitted in the solid angle  $\Delta\Omega_e$  propagate until they meet the observer's device, which we call a 'telescope'. We assume that it is located at the radius  $\rho_o$ , its aperture is  $A$  and it is oriented orthogonal to the bundle of photons. The variation  $\delta\ell$  changes the angle  $\Phi$  at the point of observation by the value

$$\delta_\ell\Phi = \Phi'\delta\ell, \quad \Phi' \equiv \frac{dB_\pm(\ell; \zeta_e)}{d\ell}. \quad (3.41)$$

The other variation is the rotation of the photon's plane around the direction to the emitter by the angle  $\delta\psi$ . Under this transformation a point with a fixed value  $\Phi$  on the photon's plane is shifted by the angle

$$\delta\chi = \sin\Phi\delta\psi \quad (3.42)$$

in the direction orthogonal to it. Thus, the area of the bundle of the photons emitted in the solid angle Eq. (3.40) on the "screen" orthogonal to the bundle and located at the radius  $\rho_o$  is

$$A = \rho_o^2\delta_\ell\Phi\delta\chi = \rho_o^2\Phi'\sin\Phi\delta\ell\delta\psi. \quad (3.43)$$

If instead of the ‘screen’ one uses a “telescope”, one can identify  $A$  with its aperture.

We denote by  $\mathcal{N}\Delta\tau_e$  the total number of the photons emitted during the proper time  $\Delta\tau_e$ . A fraction of these photons  $\Delta_e/(4\pi)$ , which is emitted in the solid angle  $\Delta_e$ , reaches the aperture of the ‘telescope’ during the corresponding time interval  $\Delta t_o$  at the point of the observation. Thus, one has

$$\frac{dN_o}{dt_o} = \frac{d\tau_e}{dt_o} \mathcal{N} \frac{\Delta_e}{4\pi} = \mathcal{C} \frac{d\tau_e}{dt_o} \frac{\ell\zeta_e^2}{\alpha^2 \mathcal{P} \Phi' \sin \Phi}, \quad (3.44)$$

$$\mathcal{C} = \frac{\mathcal{N}A}{4\pi\rho_o^2}. \quad (3.45)$$

$dN_o/dt_o$  is the number of registered photons per a unit time at the point of observation. The quantity  $\mathcal{C}$ , which enters Eq. (3.44) has a simple meaning. Consider a flat spacetime and an emitter at rest. Then  $\mathcal{C}$  is the number of particles registered per unit time by the observer located at the distance  $\rho_o$  from the emitter, provided the aperture of his/her ‘telescope’ is  $A$ . This quantity for a fixed distance  $\rho_o$  is just a common factor in Eq. (3.44) and similar expressions and does not depend on details of the emitter’s motion. For this reason it is convenient to define new quantities, such as

$$n_{t_o} = \mathcal{C}^{-1} \frac{dN_o}{dt_o}, \quad n_{t_e} = \mathcal{C}^{-1} \frac{dN_e}{dt_e}, \quad (3.46)$$

where  $d/dt_e$  is the derivative with respect to the Schwarzschild time coordinate of the emitter. In such a case we say that we are using the *Newtonian normalization*.

The above equations allow one to find how the number of the observed quanta depends on the time  $t_o$ . Instead of this one may ask how observed quanta are distributed over the observed frequency  $\omega_o$ . In the latter case it is convenient to introduce the spectral distribution of the observed quanta<sup>1</sup>,

---

<sup>1</sup> One can arrive to the same spectral function by assuming that instead of a single ion, there

$$n_{\omega_o} = \frac{\Omega}{2\pi} \frac{n_{t_o}}{|d\omega_o/dt_o|}. \quad (3.47)$$

Here we introduce an additional factor  $\Omega/2\pi$  which requires an explanation. The observed frequency  $\omega_o$  is a periodic function of  $t_o$  with the period  $T_o = 2\pi/\Omega$ . This is a time of the complete revolution of the emitter as measured at infinity. As we shall see later, the frequency  $\omega_o$  changes in some interval  $[\omega_{min}, \omega_{max}]$ , and in this interval there exist two branches of the function  $\omega_o(t_o)$ : in the first branch  $d\omega_o/dt_o > 0$ , while in the second one  $d\omega_o/dt_o < 0$ . Denote by  $N_o$  the following quantity:

$$N_o = \oint_{\omega_o} n_{\omega_o} |d\omega_o|, \quad (3.48)$$

where the integral is taken over both the branches. This gives the total number of photons received by the observer during one period of revolution of the emitter divided by the period  $T_o$ . In order to provide this useful normalization we included the factor  $\Omega/2\pi$  in Eq. (3.47).

Using Eq. (3.44), one obtains

$$n_w \equiv \omega_e n_{\omega_o} = \frac{\Omega}{2\pi} \left| \frac{d\alpha}{d\tau_e} \right|^{-1} \frac{\ell \zeta_e^2}{\Phi' \mathcal{P} \sin \Phi}. \quad (3.49)$$

Let us now obtain an expression for the time derivative of  $\alpha$  which enters Eq. (3.49). First let us notice that  $d/d\tau_e = \gamma(d/dt_e)$ , so that one has

$$\frac{d\alpha}{d\tau_e} = \gamma^2 \Omega \sin \theta_o \dot{Q}, \quad (3.50)$$

---

exist many of such ions at the circular orbit of the same radius  $\rho_e$ . In such a case, an averaging over the angle  $\varphi_e$  is effectively equivalent to the integrating (averaging) over the arrival time  $u_o$ . One again arrives at the same spectral function  $n_{\omega_o}$ .

where a dot denotes a derivative with respect to time  $t_e$ , and

$$Q = \frac{\ell \sin \varphi}{\sin \Phi}, \quad (3.51)$$

Simple calculations give  $\dot{\varphi} = \Omega$  and

$$\dot{Q} = \frac{\dot{\ell} \sin \varphi}{\sin \Phi} + \frac{\ell \cos \varphi}{\sin \Phi} \dot{\varphi} - \frac{\ell \sin \varphi \cos \Phi}{\sin^2 \Phi} \dot{\Phi}, \quad (3.52)$$

$$\dot{\ell} = \frac{\sin \varphi \sin \theta_o}{\Phi' \sin \Phi} \dot{\varphi}, \quad (3.53)$$

$$\dot{\Phi} = \frac{\sin \varphi \sin \theta_o}{\sin \Phi} \dot{\varphi}. \quad (3.54)$$

Thus one obtains

$$\dot{Q} = \Omega \left( \frac{\ell \cos \varphi \cos^2 \theta_o}{\sin^3 \Phi} + \frac{\sin^2 \varphi \sin \theta_o}{\Phi' \sin^2 \Phi} \right). \quad (3.55)$$

and

$$\frac{d\alpha}{d\tau_e} = \frac{\Omega^2 \sin \theta_o \zeta_e^2}{([1 - \zeta_e] \zeta_e^2 - \Omega^2)} \left( \frac{\ell \cos \varphi \cos^2 \theta_o}{\sin^3 \Phi} + \frac{\sin^2 \varphi \sin \theta_o}{\Phi' \sin^2 \Phi} \right). \quad (3.56)$$

Let us recall that we use the dimensionless quantities obtained by the rescaling which involves the gravitational radius  $r_g$  of the black hole. However, the quantity  $\mathcal{C}\omega_e^{-1}$  is scale invariant. We denote by  $w = \omega_o/\omega_e = \alpha^{-1}$ . Then  $n_w$  given by Eq. (3.49) is a scale invariant quantity. We call it a *spectral function*. The total number of quanta  $N_o$  (in the Newtonian normalization) defined by Eq. (3.48) is

$$N_o = \oint_w n_w |dw|. \quad (3.57)$$

### 3.2.5 General properties of spectral functions

Before presenting the results of numerical calculations, let us discuss some general expected properties of the spectral function  $n_w$  given by Eqs. (3.49) and (3.56).

We rewrite the expression Eq.(3.29) in the form

$$\alpha = \gamma[1 + \Omega Z(\varphi)], \quad Z(\varphi) = \ell(\varphi)\hat{Z}, \quad (3.58)$$

$$\hat{Z} = \pm \frac{\sqrt{\sin^2 \theta_o - \cos^2 \Phi}}{\sin \Phi}. \quad (3.59)$$

$\hat{Z}(\varphi)$  is a periodic function of the angle  $\varphi$  with period  $2\pi$ . At the points  $\varphi = 0$  and  $\pm\pi$  one has  $|\cos \Phi| = \sin \theta_o$ , so that  $Z$  vanishes at these points. Moreover, the function  $\hat{Z}$  is antisymmetric with respect to the reflection at  $\varphi = 0$ . Since  $\ell$  is a symmetric function of  $\varphi$  with respect to the reflection  $\varphi \rightarrow -\varphi$ , the function  $Z(\varphi)$  has the maximum  $Z_m$  at  $\varphi_m \in (0, \pi)$ , and the minimum  $-Z_m$  at  $\varphi_m$ . Near these points, assuming that the function  $\ell(\varphi)$  is smooth, one has ( $\beta > 0$ )

$$Z \sim \pm(Z_m - \frac{1}{2}\beta(\varphi \mp \varphi_m)^2). \quad (3.60)$$

Since  $\varphi = \Omega t_e$  one also has

$$\frac{dZ}{dt_e} \sim \mp \beta \Omega (\varphi \mp \varphi_m). \quad (3.61)$$

Consider now  $w = \alpha^{-1}$ . This quantity is a periodic function of  $\varphi$ . Denote

$$w_{\pm} = \gamma^{-1} \frac{1}{1 \mp \Omega Z_m}. \quad (3.62)$$

$w_+$  is the maximal observed frequency of photons. Such photons come from the

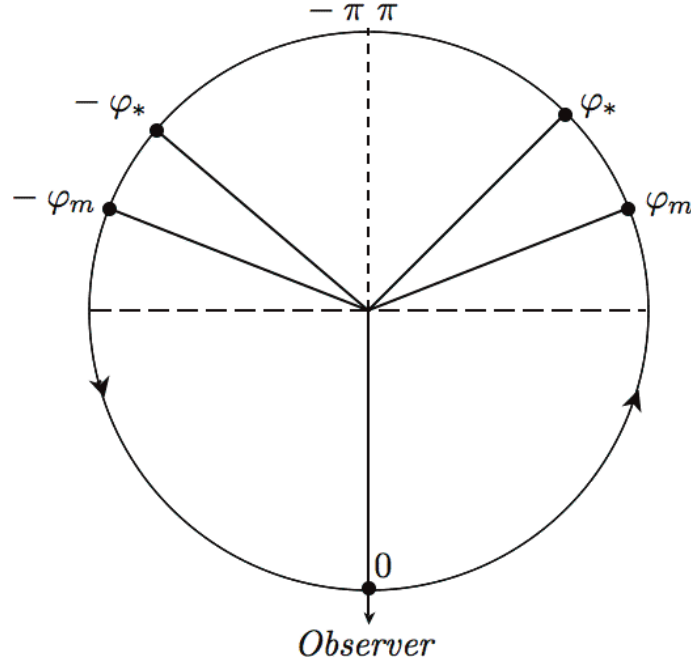


Figure 3.11: Diagram illustrating orbit of the emitter. The arrows show the direction of the emitter's motion ( $\Omega > 0$ ). For the emitter located in the right semicircle,  $\varphi \in [0, \pi]$ , photons have Doppler redshift, and for the emitter located in the left semicircle,  $\varphi \in (-\pi, 0]$ , photons have Doppler blueshift. The spectral function diverges at  $\varphi = \varphi_m$  and  $\varphi = -\varphi_m$ , where  $|\varphi_m| > \pi/2$ . The portion of the orbit corresponding to indirect null rays is defined by the angle  $|\varphi| > \varphi_*$ . There is a nonzero Doppler shift at  $\varphi = 0$  and  $\varphi = \pm\pi$ ; it is with respect to this Doppler shift that we define which photons are redshifted and blueshifted.

emitter when it is at  $-\varphi_m$ . Similarly,  $w_-$  is the minimal observed frequency and the corresponding photons are emitted at  $\varphi_m$  (see Figure 3.11). At these frequencies the spectral function has peaks. The position of the emitter  $\varphi = \Omega t_e$  is a regular (linear) function of time everywhere, including the points where the frequency  $w$  reaches its extrema, and hence  $dw/dt_e = 0$  at these points. When one transforms the rate of emission to the spectrum, one multiplies the former by the factor  $(d\alpha/d\tau_e)^{-1}$ . This is the origin of the spectrum peaks. Using Eq. (3.61) it is easy to see that  $|d\alpha/d\tau_e| \sim |w - w_{\pm}|^{1/2}$  near these points. So the spectral divergence at

the peaks is evidently integrable. It should be so since the total number of photons emitted during one period of the revolution is finite.

It is convenient to introduce a parameter

$$\Delta = \frac{2(w_+ - w_-)}{(w_+ + w_-)} = 2\Omega Z_m \quad (3.63)$$

which determines the dimensionless width of the spectrum. Figure 2.11 shows that  $\Omega$  at the ISCO for the anti-Larmor motion decreases when the magnetic field grows, and  $\Omega \rightarrow 0$  when  $b \rightarrow \infty$ . Thus one can expect that in the presence of the magnetic field the width parameter decreases. One can also conclude from Eq. (3.62) that the parameter  $\gamma^{-1}$  controls the general redshift of the spectra. Let us make one more remark concerning the properties of the spectral functions. The radiation from the emitter at  $-\varphi_m$  has the maximal Doppler blueshift, while at  $\varphi_m$  it has maximal redshift. One can expect that because of the relativistic beaming effect the number of particles with the frequency  $w_+$  should be larger than with the frequency  $w_-$ . This implies that the spectral function should be asymmetric with respect to its minimum, and the peak at  $w_+$  must be more profound than the peak at  $w_-$ . To characterize the asymmetry of the spectral function with respect to its minima we introduce the *asymmetry parameter*:

$$\delta = \frac{w_+ + w_- - 2w_0}{(w_+ - w_-)}, \quad (3.64)$$

where  $w_0$  corresponds to the minima of a spectral function.

Let us recall also that the obtained spectrum was calculated for a single orbit with a fixed radius. If a radiating domain is a ring of a finite width, one should integrate the spectrum over the radius  $\rho_e$  with a weight proportional to the density

of the matter of iron ions in such a ring. After this the infinite peaks disappear and the spectrum would be regularized.

## Chapter 4

# Spectral function plots and common features

After the general remarks of the properties of the spectral functions that we studied in Chapter 3, let us present concrete examples of the spectral function plots obtained by numerical calculation. To illustrate important features of the spectral functions, we present results here for three different types of the circular motion of the emitter: (1)  $\rho_e = 3$ ,  $b = 0$ ; (2)  $\rho_e = 3$ ,  $b = 2.251$ ; and (3)  $\rho_e = 1.2$ ,  $b = 2.251$ . In the first case the orbit is the ISCO in the absence of the magnetic field. In the second one it is a SCO with the same radius  $\rho_e = 3$  as in (1) but in the presence of the magnetic field  $b$ . The last case is the anti-Larmor ISCO for the same value as in (2) of the magnetic field. These choices of the emitter's orbit parameters allow one to demonstrate the dependence of the spectral functions on the magnetic field. For each of these cases we constructed three different plots corresponding to three different values,  $30^\circ$ ,  $60^\circ$  and  $85^\circ$ , of the inclination angle  $\theta_o$ . These plots allow one to discuss the dependence of the spectral functions on the angular position of the

distant observer with respect to the emitter's orbit. Figures 4.1–4.3 present spectral functions for the case (1) and three chosen inclination angles. Figures 4.4–4.6 present similar spectral functions for the case (2) and three chosen inclination angles. The spectral functions for the case (3) and three inclination angles are shown in Figures 4.7–4.9. By comparing the figures for the same inclination angle one can see that if one increases the magnetic field keeping the other parameters ( $\rho_e$  and  $\theta_o$ ) fixed, then the spectral profiles get more narrow. One can see this from the values of the parameter  $\Delta$  [see Eq.(3.63)]. Namely, for the ISCO at  $\rho_e = 3$ ,  $b = 0$ , and the inclination angle values  $30^\circ$ ,  $60^\circ$  and  $85^\circ$ , we have  $\Delta = 0.476$ ,  $0.845$ ,  $0.995$ , respectively, while for the SCO at  $\rho_e = 3$ ,  $b = 2.251$ , we have  $\Delta = 0.018$ ,  $0.031$ ,  $0.037$ . This narrowing is accompanied by a general redshift of the spectral function.

To summarize, the common features of the spectrum plots are: (1) the existence of the two sharp peaks at the frequencies  $w_\pm$ ; (2) the existence of two branches of the spectrum; (3) the increase of the average redshift of the spectral frequencies for the anti-Larmor ISCO with the increase of the magnetic field; (4) the narrowing of the frequency bands with the increase of the magnetic field; (5) the asymmetry of the spectrum.

The discussion in the end of chapter 3 gives simple qualitative explanations of the properties (1)-(3). Let us briefly discuss the properties (4) and (5). The larger value of the magnetic field, the closer to the horizon is the corresponding anti-Larmor ISCO and the greater is the redshift. Numerical calculations confirm also that the width Eq. (3.63) decreases with the increase of  $b$  (property (4)). The asymmetry (5) of the spectrum is a generic property of the broadening of the sharp spectral lines for the emitters moving near black holes. It is a result of the relativistic (Doppler) beaming effect. The calculations show that the asymmetry

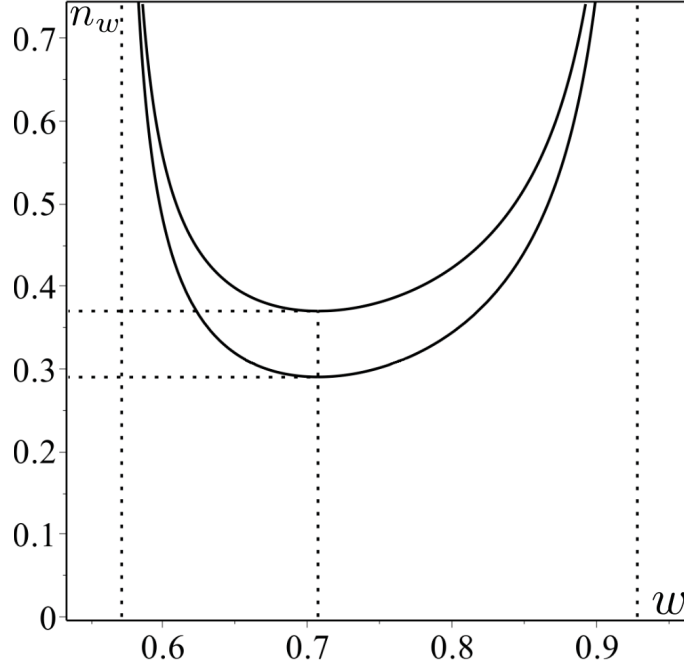


Figure 4.1: Spectral function for the anti-Larmor ISCO,  $b = 0$ , at  $\zeta_e = 1/3$ . The inclination angle is  $\theta_o = 30^\circ$ . The angular velocity of the emitter is  $\Omega = 0.136$ , and its specific energy is  $\mathcal{E} = 0.943$ . The spectrum has peaks at  $w_- = 0.571$  ( $\varphi_m = 97^\circ 85'$ ) and at  $w_+ = 0.928$  (at  $-\varphi_m$ ). The minimal values (0.290 and 0.370) of  $n_w$  for the two spectral branches are at  $w_0 = 0.707$ . The width parameter is  $\Delta = 0.476$ , and the asymmetry parameter is  $\delta = 0.236$ . One also has  $N_o = 0.285$ .

effect becomes more profound when the inclination angle becomes larger. The asymmetry parameter, as well as the width parameter for the spectral functions presented in the Figures 4.1–4.9, can be found in the corresponding captures.

Let us emphasize that all these spectral functions were calculated for an emitter at a given radius in circular orbit. Infinite sharp peaks in the plots are the result of this assumptions. As we discussed in the Introduction, these peaks are smeared when emitters are distributed over the disk of finite width. In the model that we described earlier one can expect that corresponding charged disk is located at smaller radius than the ISCO for neutral particles. However, the distribution of

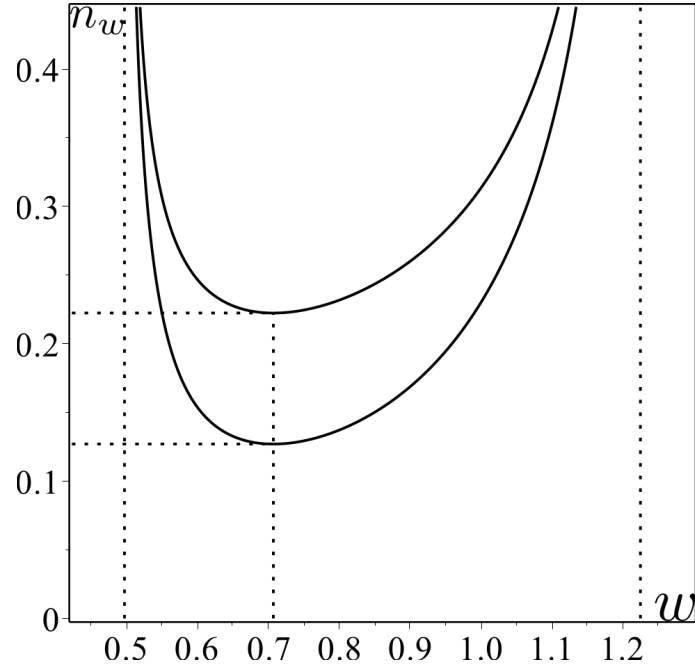


Figure 4.2: Spectral function for the anti-Larmor ISCO,  $b = 0$ , at  $\zeta_e = 1/3$ . The inclination angle is  $\theta_o = 60^\circ$ . The angular velocity of the emitter is  $\Omega = 0.136$ , and its specific energy is  $\mathcal{E} = 0.943$ . The spectrum has peaks at  $w_- = 0.497$  ( $\varphi_m = 107^\circ 9'$ ) and at  $w_+ = 1.224$  (at  $-\varphi_m$ ). The minimal values (0.127 and 0.222) of  $n_w$  for two spectral branches are at  $w_0 = 0.707$ . The width parameter is  $\Delta = 0.845$ , and the asymmetry parameter is  $\delta = 0.423$ . One also has  $N_o = 0.356$ .

charged emitters in the inner “charged” ring is not known. For this reason we did not make the corresponding averaging of the obtained spectral functions, which might be sensitive to the additional assumptions.

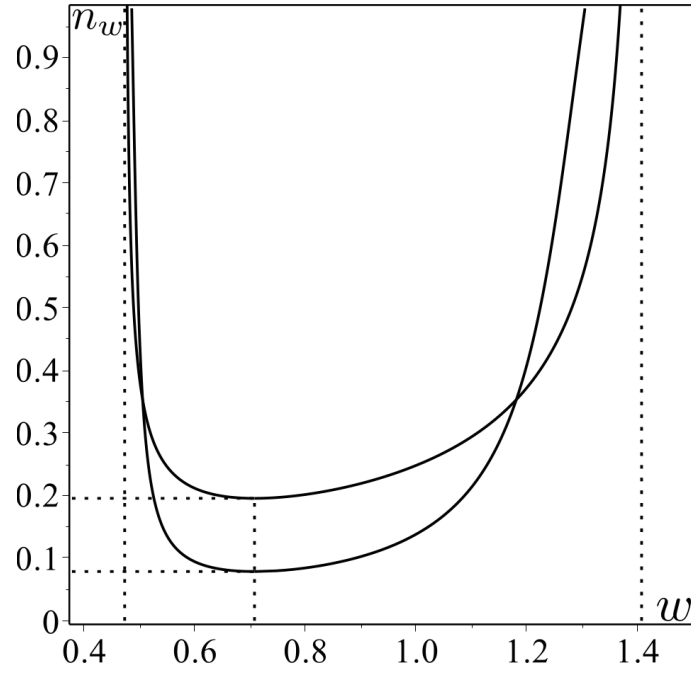


Figure 4.3: Spectral function for the anti-Larmor ISCO,  $b = 0$ , at  $\zeta_e = 1/3$ . The inclination angle is  $\theta_o = 85^\circ$ . The angular velocity of the emitter is  $\Omega = 0.136$ , and its specific energy is  $\mathcal{E} = 0.943$ . The spectrum has peaks at  $w_- = 0.472$  ( $\varphi_m = 118^\circ 4'$ ) and at  $w_+ = 1.407$  (at  $-\varphi_m$ ). The minimal values (0.079 and 0.196) of  $n_w$  for two spectral branches are at  $w_0 = 0.707$ . The width parameter is  $\Delta = 0.995$ , and the asymmetry parameter is  $\delta = 0.498$ . One also has  $N_o = 0.397$ .

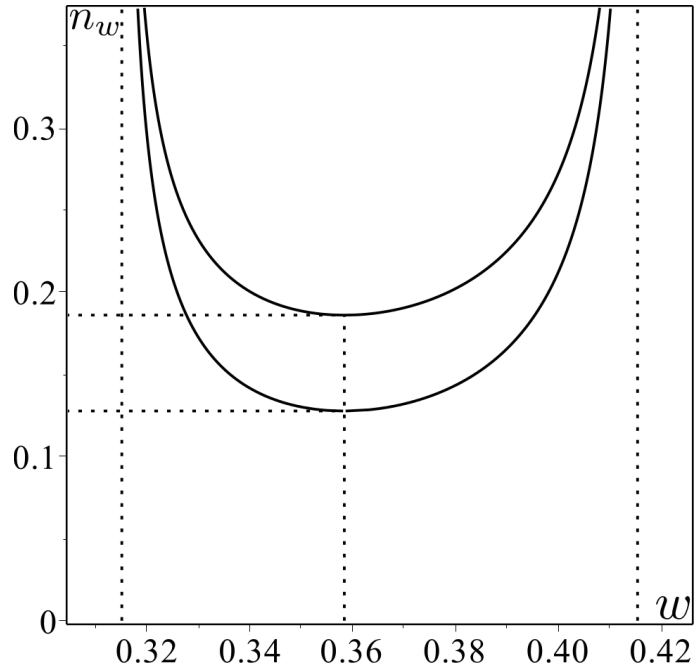


Figure 4.4: Spectral function for the anti-Larmor ISCO,  $b = 2.251$ , at  $\zeta_e = 5/6$ . The inclination angle is  $\theta_o = 30^\circ$ . The angular velocity of the emitter is  $\Omega = 0.162$ , and its specific energy is  $\mathcal{E} = 0.465$ . The spectrum has peaks at  $w_- = 0.315$  ( $\varphi_m = 104^\circ 7'$ ) and at  $w_+ = 0.415$  (at  $-\varphi_m$ ). The minimal values (0.128 and 0.186) of  $n_w$  for two spectral branches are at  $w_0 = 0.358$ . The width parameter is  $\Delta = 0.274$ , and the asymmetry parameter is  $\delta = 0.137$ . One also has  $N_o = 0.050$ .

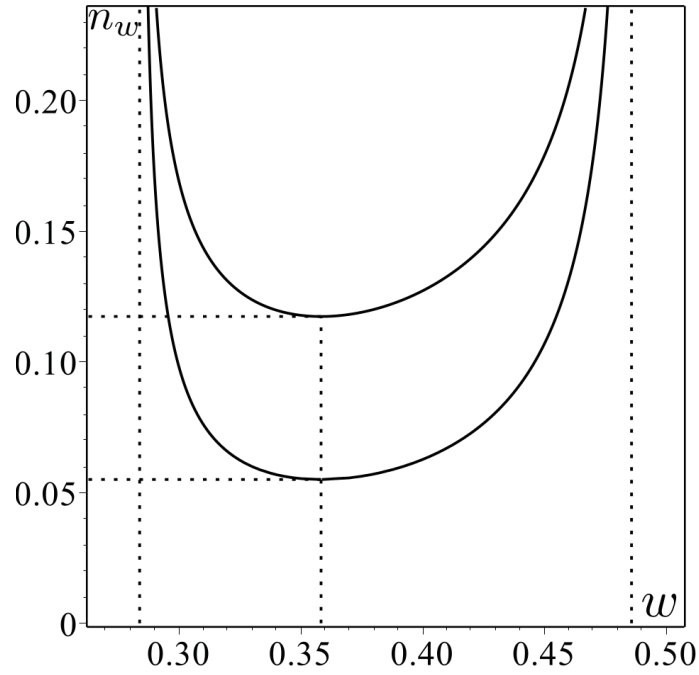


Figure 4.5: Spectral function for the anti-Larmor ISCO,  $b = 2.251$ , at  $\zeta_e = 5/6$ . The inclination angle is  $\theta_o = 60^\circ$ . The angular velocity of the emitter is  $\Omega = 0.162$ , and its specific energy is  $\mathcal{E} = 0.465$ . The spectrum has peaks at  $w_- = 0.284$  ( $\varphi_m = 124^\circ 6'$ ) and at  $w_+ = 0.486$  (at  $-\varphi_m$ ). The minimal values (0.055 and 0.117) of  $n_w$  for two spectral branches are at  $w_0 = 0.358$ . The width parameter is  $\Delta = 0.525$ , and the asymmetry parameter is  $\delta = 0.262$ . One also has  $N_o = 0.058$ .

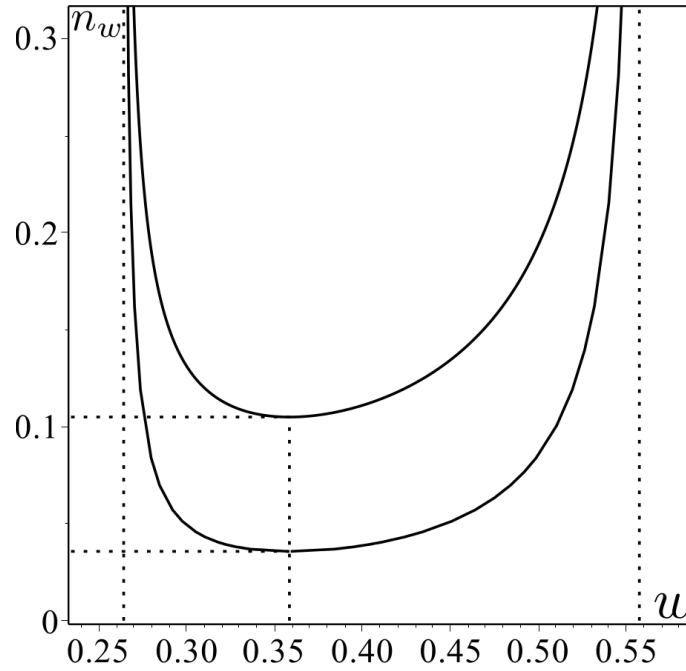


Figure 4.6: Spectral function for the anti-Larmor ISCO,  $b = 2.251$ , at  $\zeta_e = 5/6$ . The inclination angle is  $\theta_o = 85^\circ$ . The angular velocity of the emitter is  $\Omega = 0.162$ , and its specific energy is  $\mathcal{E} = 0.465$ . The spectrum has peaks at  $w_- = 0.264$  ( $\varphi_m = 158^\circ 6'$ ) and at  $w_+ = 0.558$  (at  $-\varphi_m$ ). The minimal values (0.036 and 0.105) of  $n_w$  for two spectral branches are at  $w_0 = 0.358$ . The width parameter is  $\Delta = 0.714$ , and the asymmetry parameter is  $\delta = 0.357$ . One also has  $N_o = 0.085$ .

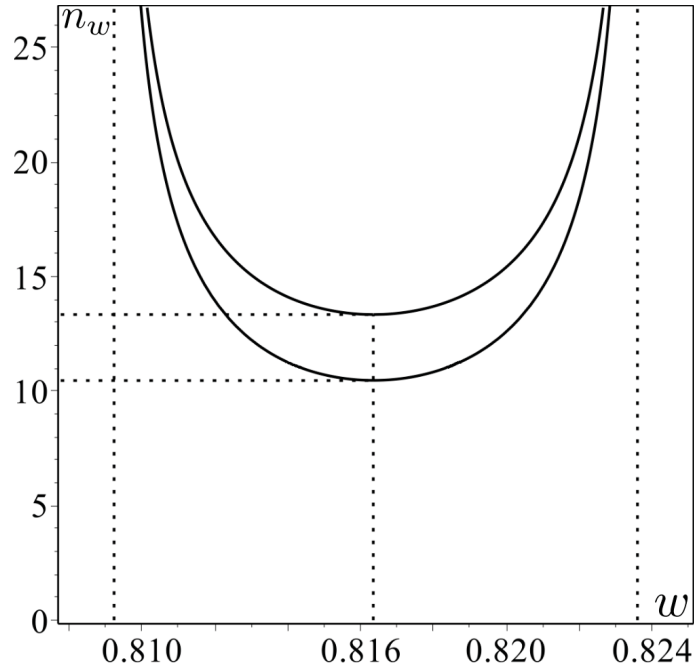


Figure 4.7: Spectral function for an anti-Larmor SCO,  $b = 2.251$ , at  $\zeta_e = 1/3$ . The inclination angle is  $\theta_o = 30^\circ$ . The angular velocity of the emitter is  $\Omega = 0.005$ , and its specific energy is  $\mathcal{E} = 0.817$ . The spectrum has peaks at  $w_- = 0.809$  ( $\varphi_m = 97^\circ 85'$ ) and at  $w_+ = 0.823$  (at  $-\varphi_m$ ). The minimal values (10.46 and 13.35) of  $n_w$  for two spectral branches are at  $w_0 = 0.816$ . The width parameter is  $\Delta = 0.018$ , and the asymmetry parameter is  $\delta = 0.009$ . One also has  $N_o = 0.390$ .

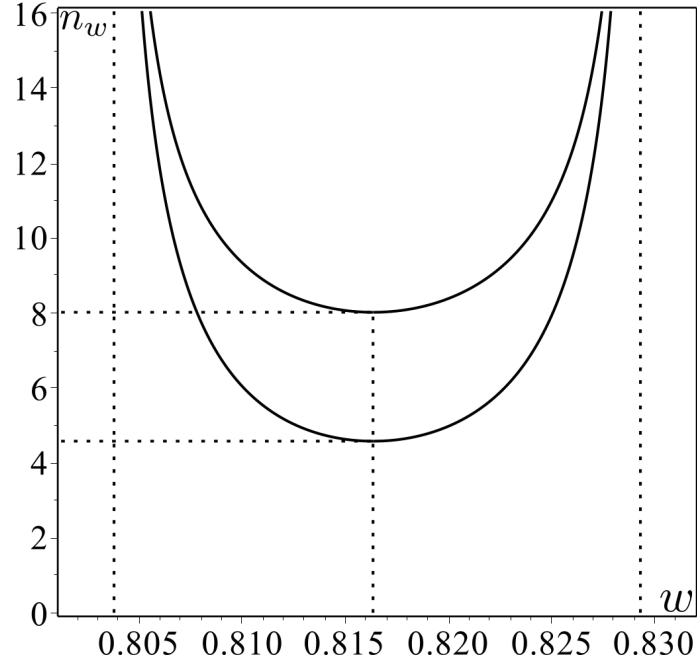


Figure 4.8: Spectral function for an anti-Larmor SCO,  $b = 2.251$ , at  $\zeta_e = 1/3$ . The inclination angle is  $\theta_o = 60^\circ$ . The angular velocity of the emitter is  $\Omega = 0.005$ , and its specific energy is  $\mathcal{E} = 0.817$ . The spectrum has peaks at  $w_- = 0.804$  ( $\varphi_m = 107^\circ 9'$ ) and at  $w_+ = 0.829$  (at  $-\varphi_m$ ). The minimal values (4.578 and 8.018) of  $n_w$  for two spectral branches are at  $w_0 = 0.816$ . The width parameter is  $\Delta = 0.031$ , and the asymmetry parameter is  $\delta = 0.016$ . One also has  $N_o = 0.382$ .

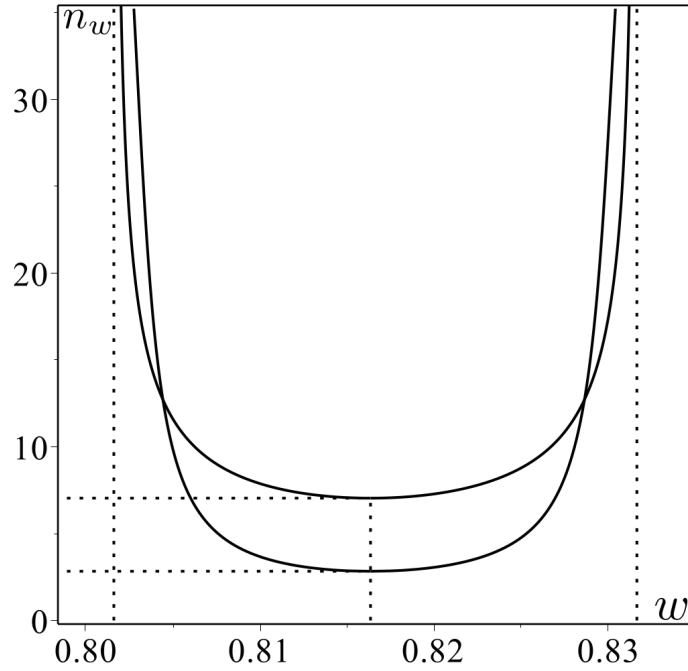


Figure 4.9: Spectral function for an anti-Larmor SCO,  $b = 2.251$ , at  $\zeta_e = 1/3$ . The inclination angle is  $\theta_o = 85^\circ$ . The angular velocity of the emitter is  $\Omega = 0.005$ , and its specific energy is  $\mathcal{E} = 0.817$ . The spectrum has peaks at  $w_- = 0.802$  ( $\varphi_m = 118^\circ 4'$ ) and at  $w_+ = 0.832$  (at  $-\varphi_m$ ). The minimal values (2.836 and 7.051) of  $n_w$  for two spectral branches are at  $w_0 = 0.816$ . The width parameter is  $\Delta = 0.037$ , and the asymmetry parameter is  $\delta = 0.019$ . One also has  $N_o = 0.388$ .

# Chapter 5

## Conclusion

With most physicists and astrophysicists in agreement that black holes do exist, the focus of black hole research is shifted to exploring the detailed properties of these systems. Nature has provided us with an extremely useful probe of the region very close to an accreting black hole, i.e., X-ray radiation of the matter in the vicinity of the black hole can imprint characteristic features into the X-ray spectra of black hole systems. The most prominent spectral feature is often the fluorescent  $K\alpha$  emission line of iron. Detailed X-ray spectroscopy of these features can be used to study Doppler and gravitational redshifts, thus providing key information on the location and kinematics of the cold material. This is a powerful tool that allows one to probe within a few gravitational radii, or less, of the event horizon. This tool enables one to extract information about the accretion disk, the black hole, and their interaction, such as the shape and size of the disk or the mass and spin of the black hole.

As we mentioned in Chapter 1 (see section 1.1), magnetic fields play an important role in black hole physics. In the presence of a magnetic field the motion of

plasma and charged particles is modified. We exploit the simplest model in which a non-rotating black hole is surrounded by a magnetic field which is homogeneous at infinity. In this thesis we studied the action of such a magnetic field in the vicinity of a black hole on the bound circular orbits of charged particles. As we saw in Chapter 2, the main new effect is that the position of the innermost stable circular orbit (ISCO) can be closer than for an uncharged particle. This effect is quite similar to the action of the angular momentum of rotating black holes on the ISCO positions. This observation raises an interesting opportunity to study of a regular magnetic field near a black hole by observing the radiation emitted by charged particles motion around the black hole.

As we discussed in Section 1.2, the iron  $K\alpha$  line is intrinsically a rather narrow line. However, when the iron ions are revolving around a Newtonian centre or a black hole the situation is quite different. In that case the iron  $K\alpha$  line is broadened. One can use broadening of the line to study the main features of the accretion disk, of the geometry of space-time, and of the interaction between the accretion disk and the black hole. In this thesis we studied the main features of the broadened emission spectrum of the  $K\alpha$  line of ionized iron for magnetized black holes. The main reasons of the broadening are the relativistic Doppler effect and the gravitational redshift.

In Section 1.3, we discussed the non-relativistic case of an emitter revolving a Newtonian centre. We can see a symmetric double peak corresponding to emission from material on both the approaching (blueshifted) and receding (redshifted) side. When we consider a non-relativistic disk, each radius of the disk produces a symmetric double-horned line profile. Taking into account all these line profiles we see the peaks to be smoothed. When the emitter is revolving with velocities close

to the speed of light or at least comparable to it, the special relativistic beaming enhances the blue peak (i.e., the peak which appears in the side of high frequencies of the spectrum), which is why we see the asymmetry in the Figure 1.8. Finally, when we have a non-moving particle near a black hole the gravitational redshift shifts the spectrum to lower energy. By taking all these effects and parameters into account one ends up to a result similar to the plot in the Figure 1.2.

In this thesis, we discussed the radiation from emitters revolving around a magnetized non-rotating black hole. As we discussed in Chapter 2 of this thesis, charged particle orbits near such black holes are strongly affected by the magnetic field when the dimensionless field parameter  $b$  becomes of the order of one or greater. The effect of the magnetic field depends on the direction of motion of the particle. For anti-Larmor orbits the Lorentz force is directed outwards from the black hole. The ISCO radius for the anti-Larmor particles can be close to the event horizon. Such particles on circular orbits, after passing the ISCO limit for neutral particles at  $6M$ , continue their motion at a sequence of SCOs until they reach the critical (ISCO) radius corresponding to the given value of  $b$ . During this process their specific energy  $\mathcal{E}$  decreases, so that in such process they lose slowly their energy and angular momentum (for example, as a result of synchrotron radiation). The maximal energy release in this process reaches 100% in the limit  $b \rightarrow \infty$ .

The behaviour of the Larmor particles is quite different. For  $b > 0$  their circular orbits can also have radius less than  $6M$ . However, in order to move on such orbits they need to receive some additional energy. This means that one can expect that either such particles are accumulated during some period of time near  $6M$  orbits, or they simply fall directly into the black hole, similarly to neutral particles. This might have a quite interesting consequence: the spatial separation of charge. We

do not discuss this effect here. In Chapter 3, we focused on the radiation emitted by anti-Larmor particles moving close to the black hole in the presence of the magnetic field. Namely, we analyzed two problems: (1) images of such orbits, and (2) spectral broadening of the emission received from a moving emitter by a distant observer. The results of the second problem can be found in Chapter 4. Both of these problems require ray-tracing of photons in the Schwarzschild metric, a problem which is well known and discussed in detail in the literature. However, we apply this ray-tracing to orbits which are closer than  $6M$  to the black hole horizon. These orbits are interesting for magnetized black holes. Similar remarks can be made for the spectral broadening problem. In magnetized black holes both the position of the circular orbits and the angular velocity of the evolution are different from the Keplerian case.

Images of the anti-Larmor orbits close to the horizon of the magnetized black holes are presented in Figures 3.6-3.10. The main conclusion is that in the limit of large magnetic field  $b$  the ISCO image structure is simplified. In this limit for  $\theta_o$  near  $\pi/2$  the image basically consists of two parts: (1) a semicircle inside the shadow domain region, and (2) a practically straight line in the equatorial plane. The first part of the image is generated by rays from the part of the orbit “behind” the black hole, while the latter part is formed by direct rays emitted “in front” of the black hole.

We discussed and compared the spectral functions for sharp line broadening. The  $\delta$ -function-like radiation spectrum for the monochromatic radiation of the charged anti-Larmor emitter is registered by a distant observer as a broadened spectral line. This is the result of two effects: the Doppler effect and the gravitational redshift. The width of the spectral function is determined by the periodic

Doppler blueshift and redshift. It is proportional to the angular velocity  $\Omega$  of the emitter, and it vanishes in the limit  $b \rightarrow \infty$ . The closer the orbit of the emitter is to the horizon, the larger is the influence of the gravitational field on the spectrum. This effect results in the total redshift of the spectral frequencies. One can summarize the generic properties of spectral broadening for magnetized black hole as follows: when the magnetic field  $b$  increases, both the width of the spectrum and its average frequency decrease.

In the present work we made two simplifying assumptions. We used a special ansatz for the form of the magnetic field. The magnetic field is uniform and aligned along the axis of symmetry of the black hole. In realistic black holes, one cannot expect that the magnetic field is homogeneous and extends to infinity. However, for the motion of a charged particle in the equatorial plane and in the black hole vicinity this approximation might be reasonable. It is easy to extend the results to other types of a regular magnetic field, e.g., for a dipolar magnetic field around a static black hole (see, e.g., [103]). Moreover, a model of the homogeneous magnetic field is a good approximation for more realistic magnetic fields generated by currents in a conducting accretion disk, provided the size of the black hole is much smaller than the size of the disk (see, e.g., the discussion in [95]).

Another assumption was that the radiating particles are localized in an infinitely thin ring of a fixed radius. In reality, one can expect that there exists some distribution of anti-Larmor emitters extended from  $6M$  to their ISCO radius. In order to obtain the emission spectrum from such a ring of finite size, one needs to perform an additional integration of the obtained spectra with some weight function which describes the distribution of emitters within this ring. Such an averaging would smear infinite peaks and make them finite.

Because of the assumptions made, the main conclusions of the present work seem to be quite robust. Namely, for anti-Larmor emitters in magnetized black holes with sufficiently strong magnetic fields, ISCO's are close to the horizon, and the dominant effects for this inner domain of radiation result in a greater redshift and narrowing of the spectrum. This allows one to hope that observations of the broadening in the iron  $K\alpha$  lines in magnetized black holes can provide us with direct information about the magnetic field in the black hole vicinity.

An interesting open problem for study in the future is the comparison of the spectral broadening in magnetized black holes with similar effects in rotating black holes. The dragging effect of the black hole on neutral particles is similar to the effect of a magnetic field on charged particles. In both cases, ISCO's for (1) co-rotating particles in the Kerr metric and (2) anti-Larmor particles in the magnetic field around a Schwarzschild black hole can be located arbitrarily close to the horizon (at least in the  $r$ -coordinate in Kerr, though not in proper distance). However, there is a big difference between these two cases. A particle close to the Kerr black hole is co-rotating with the black hole. Its angular velocity which is nonzero tends to the black hole angular velocity. In the magnetized black holes for anti-Larmor orbits close to the horizon of a Schwarzschild black hole, the angular velocity also tends to the black hole angular velocity, but in this case the angular velocity is zero. Hence, one can expect that the width of the spectra for the radiation emitted by anti-Larmor particles moving close to the horizon of magnetized black holes must be smaller than the corresponding width for neutral particles in rotating black holes. It would be interesting to perform the calculation of spectral function broadening for a general case of a magnetized rotating black hole.

For both cases of rotating and non rotating black holes the out-of-equatorial-

plane motion of the emitter is chaotic. Therefore, it is impossible to perform analytic calculations of the spectral function broadening. The only way would be by numerical calculations with unknown results, since it is hard to predict how chaos is going to effect the spectral function broadening. However, one may try to calculate analytically or maybe semi-analytically the spectral function broadening for the case that we have small oscillation about a circular orbit. Moreover, this could be the first step for the study of the spectral function broadening in the case of out-of-equatorial-plane motion of the emitter.

# Bibliography

- [1] D. M. Eardley, A. P. Lightman, N. I. Shakura, S. L. Shapiro, and R. A. Sunyaev, "A status report on Cygnus X-1," *Comments Astrophys.* 7, 151, 1978.
- [2] A. P. Cowley, D. Crampton, J. B. Hutchings, *et al.*, "Discovery of a massive unseen star in LMC X-3", *Astrophys. J.* 272, 118, 1983.
- [3] J. B. Hutchings, D. Crampton, and A. P. Cowley, "LMC X-1: Another massive binary?," *IAU Circ. No.* 3791, 1983.
- [4] N. E. White, "The X-ray properties of accreting black holes," *Adv. Space Res.* 3, 9, 1984.
- [5] M. G. Watson, "Astrophysics: The most reliable black hole yet," *Nature* 321, 16, 1986.
- [6] J. E. McClintock and R. A. Remillard, "The black hole binary A0620-00," *Astrophys. J.* 308, 110, 1986.
- [7] P. A. Caraveo, G. F. Bignami, L. Vigroux, J. A. Paul and R. C. Lamb, "An identification for Geminga: A review of all the available data," *Adv. Space Res.* 3, 77, 1994.

- [8] G. S. Bisnovaty-Kogan, “Model of the object Geminga: Degenerate dwarf rotating around a black hole,” *Astrophysics* 22, 222, 1985.
- [9] B. Margon, “Observations of SS 433,” *Ann. Rev. Astron. Astrophys.* 22, 507, 1984.
- [10] Z. Yu. Metlitskaya, A. V. Goncharskil, and A. M. Cherepashchuk, “Characteristics of the object SS 433 (V 1343 Aql) as a massive eclipsing binary system,” *Astron. Zh.* 61, 124, 1984.
- [11] E. A. Antokhina and A. M. Cherepashchuk, “SS433 as a black-hole candidate,” *Pis'ma Astron. Zh.* 11, 10, 1985.
- [12] R. D. Blandford and K. S. Thorne, *General Theory of Relativity: An Einstein Centenary Survey* (Eds.) S. W. Hawking and W. Israel, Cambridge Univ. Press, 1979.
- [13] M. C. Begelman, R. D. Blandford, and M. J. Rees, “Theory of extragalactic radio sources,” *Rev. Mod. Phys.* 56, 255, 1984.
- [14] M. J. Rees, “Black hole models for active galactic nuclei,” *Ann. Rev. Astron. Astrophys.* 22, 471, 1984.
- [15] W. L. Young *et al.*, “Evidence for a supermassive object in the nucleus of the galaxy M87 from SIT and CCD area photometry”, *Astrophys. J.* 221, 721 (1978).
- [16] B. P. Abbott *et al.* [LIGO Scientific and Virgo Collaborations], “Observation of gravitational waves from a binary black hole merger,” *Phys. Rev. Lett.* 116, no. 6, 061102, 2016.

- [17] B. P. Abbott *et al.* [LIGO Scientific and Virgo Collaborations], “GW151226: Observation of gravitational waves from a 22-solar-mass binary black hole coalescence,” *Phys. Rev. Lett.* 116, no. 24, 241103, 2016.
- [18] S. Doeleman *et al.*, “Event-horizon-scale structure in the supermassive black hole candidate at the Galactic Centre,” *Nature* 455, 78, 2008.
- [19] R. Narayan, “Black holes in astrophysics,” *New J. Phys.* 7, 199, 2005.
- [20] S. A. Balbus and J. F. Hawley, “Instability, turbulence, and enhanced transport in accretion disks,” *Rev. Mod. Phys.* 70, 1, 1998.
- [21] J. H. Krolik, “Magnetic stresses at the inner edges of accretion disks around black holes,” *AIP Conf. Proc.* 586, 674, 2001.
- [22] R. P. Eatough *et al.*, “A strong magnetic field around the supermassive black hole at the centre of the Galaxy,” *Nature* 501, 391, 2013.
- [23] H. Falcke and S. Markoff, “The jet model for Sgr A\*: radio and x-ray spectrum,” *Astron. Astrophys.* 362, 113 (2000) [astro-ph/0102186].
- [24] M. Moscibrodzka, C. F. Gammie, J. C. Dolence, H. Shiokawa, and P. K. Leung, “Radiative models of Sgr A\* from GRMHD simulations,” *Astrophys. J.* 706, 497, 2009.
- [25] J. Dexter, E. Agol, P. C. Fragile and J. C. McKinney, “The submillimeter bump in Sgr A\* from relativistic MHD simulations,” *Astrophys. J.* 717, 1092, 2010.
- [26] V.P. Frolov and A. Zelnikov, *Introduction to Black Hole Physics*, Oxford University Press, 2011.

- [27] V. P. Frolov, A. A. Shoom, and C. Tzounis, “Radiation from an emitter revolving around a magnetized nonrotating black hole,” *Phys. Rev. D* 90, no. 2, 024027, 2014.
- [28] V. P. Frolov, A. A. Shoom, and C. Tzounis, “Spectral line broadening in magnetized black holes,” *JCAP* 1407, 059, 2014.
- [29] S. Abdolrahimi and C. Tzounis, “Production of black holes and string balls in a two-dimensional split-fermion model,” *JHEP* 1409, 061, 2014.
- [30] S. Abdolrahimi, R. B. Mann, and C. Tzounis, “Distorted local shadows,” *Phys. Rev. D* 91, no. 8, 084052, 2015.
- [31] S. Abdolrahimi, R. B. Mann, and C. Tzounis, “Double images from a single black hole,” *Phys. Rev. D* 92, 124011, 2015.
- [32] S. Abdolrahimi, J. Kunz, P. Nedkova, and C. Tzounis, “Properties of the distorted Kerr black hole,” *JCAP* 1512, 009, 2015.
- [33] S. Abdolrahimi, D. N. Page and C. Tzounis, “Ingoing Eddington-Finkelstein metric of an evaporating black hole,” arXiv:1607.05280 [hep-th].
- [34] D. Grasso and H. R. Rubinstein, “Magnetic fields in the early universe,” *Phys. Rept.* 348, 163, 2001.
- [35] M. Shibata and K. Taniguchi, “Coalescence of black hole-neutron star binaries,” *Living Rev. Rel.* 14, 6, 2011.
- [36] G. Romero and G. Vila, *Introduction to Black Hole Astrophysics*, Springer-Verlag, Berlin, 2013.

- [37] B. Punsky, *Black Hole Gravitohydrodynamics*, 2nd Edition Springer-Verlag, Berlin, 2008.
- [38] D. Price and S. Rosswog, “Producing ultra-strong magnetic fields in neutron star mergers,” *Science* 312, 719, 2006.
- [39] C. Kouveliotou *et al.*, “An X-ray pulsar with a superstrong magnetic field in the soft gamma-ray repeater SGR 1806-20,” *Nature* 393, 235, 1998.
- [40] A. I. Ibrahim, S. Safi-Harb, J. H. Swank, W. Parke, and S. Zane, “Discovery of cyclotron resonance features in the soft gamma repeater SGR 1806-20,” *Astrophys. J.* 574, L51, 2002.
- [41] J. M. Miller, J. Raymond, A. C. Fabian, D. Steeghs, J. Homan, C. S. Reynolds, M. van der Klis, and R. Wijnands, “The magnetic nature of disk accretion onto black holes,” *Nature* 441, 953, 2006.
- [42] R. D. Blandford and R. L. Znajek, “Electromagnetic extractions of energy from Kerr black holes,” *Mon. Not. Roy. Astron. Soc.* 179, 433, 1977.
- [43] R. Znajek, “On being close to a black hole without falling in,” *Nature* 262, 270, 1976.
- [44] S. Koide, K. Shibata, T. Kudoh, and D.L. Meier, “Extraction of black hole rotational energy by a magnetic field and the formation of relativistic jets,” *Science* 295, 1688, 2002.
- [45] S. Koide, “Relativistic outflow magnetically driven by black hole rotation,” *Astrophys. J.* 606, L45 2004.

- [46] M. Camenzind, *Compact Objects in Astrophysics: White Dwarfs, Neutron Stars and Black Holes*, Springer-Verlag, Berlin, 2013.
- [47] K. S. Thorne, R. H. Price, and D. A. MacDonald, *Black Holes: The Membrane Paradigm*, Yale University Press, 1986
- [48] N. A. Silant'ev, M. Y. Piotrovich, Y. N. Gnedin and T. M. Natsvlishvili, "Magnetic fields of AGNs and standard accretion disk model: Testing by optical polarimetry," *Astron. Astrophys.* 507, 171, 2009
- [49] M. Y. Piotrovich, Y. N. Gnedin, T. M. Natsvlishvili, and N. A. Silant'ev, "Magnetic fields of active galactic nuclei and quasars from the SDSS catalog," *Astronomy Letters* , 36, 389, 2010.
- [50] N. A. Silant'ev, Y. N. Gnedin, S. D. Buliga, M. Y. Piotrovich, and T. M. Natsvlishvili, "Magnetic fields of active galactic nuclei and quasars with polarized broad H-alpha lines," *Astrophys. Bull.* 68, 14, 2013
- [51] J. A. Kennea *et al.*, "Swift discovery of a new soft gamma repeater, SGR J1745-29, near Sagittarius A\*," *Astrophys. J.* 770, L24, 2013.
- [52] K. Mori *et al.*, "NuSTAR discovery of a 3.76-second transient magnetar near Sagittarius A\*," *Astrophys. J.* 770, L23, 2013.
- [53] R. P. Eatough *et al.*. "Detection of radio pulsations from the direction of the NuSTAR 3.76 second X-ray pulsar at 8.35 GHz," *The Astronomer's Telegram* 5040, 1, 2013.

- [54] R. M. Shannon and S. Johnston, “Radio properties of the magnetar near Sagittarius A\* from observations with the Australia Telescope Compact Array,” *Mon. Not. Roy. Astron. Soc.* 435, 29, 2013.
- [55] K. J. Lee *et al.*, “Polarisation profiles and rotation measure of PSR J1745-2900 measured at Effelsberg,” *The Astronomer’s Telegram* 5064, 1, 2013.
- [56] M. A. Brentjens and A. G. De Bruyn, “Faraday rotation measure synthesis,” *Astronomy & Astrophysics* 441.3, 1217, 2005.
- [57] R. P. Eatough *et al.*, “A strong magnetic field around the supermassive black hole at the centre of the Galaxy,” *Nature* 501, 391, 2013.
- [58] G. C. Bower, H. Falcke, M. C. H. Wright, and D. C. Backer, “Variable linear polarization from Sagittarius A\*: Evidence for a hot turbulent accretion flow,” *Astrophys. J.* 618, L29, 2004.
- [59] D. P. Marrone, J. M. Moran, J.-H. Zhao, and R. Rao, “An unambiguous detection of Faraday rotation in Sagittarius A\*,” *Astrophys. J.* 654, L57, 2006
- [60] C. J. Law, M. A. Brentjens, and G. Novak, “A constraint on the organization of the Galactic Center magnetic field using Faraday rotation,” *The Astrophysical Journal* 731.1, 36, 2011.
- [61] G. C. Bower, D. C. Backer, J. H. Zhao, W. M. Goss, and H. Falcke, “The linear polarization of Sagittarius A\*. 1. VLA Spectro-polarimetry at 4.8 and 8.4-GHz,” *Astrophys. J.* 521, 582, 1999.

- [62] O. Kopáček, “Asymptotically uniform electromagnetic test fields around a drifting Kerr black hole,” WDS Vol. 08 Proceedings of Contributed Papers Part III, 198, 2008.
- [63] J. Bicák and L. Dvorák, “Stationary electromagnetic fields around black holes. II. General solutions and the fields of some special sources near a Kerr black hole,” *Gen. Relativ. Gravit.* 7, 959, 1976.
- [64] J. Bicák and L. Dvorák, “Stationary electromagnetic fields around black holes,” *Czech. J. Phys. B* 27, 127, 1977.
- [65] J. Bicák and L. Dvorák, “Stationary electromagnetic fields around black holes. III. General solutions and the fields of current loops near the Reissner-Nordström black hole,” *Phys. Rev. D* 22, 2933, 1980.
- [66] A. F. Zakharov, N. S. Kardashev, V. N. Lukash, and S. V. Repin, “Magnetic fields in AGNs and microquasars,” *Mon. Not. Roy. Astron. Soc.* 342, 1325, 2003.
- [67] A. N. Aliev and D. V. Galtsov, “Magnetized black holes,” *Sov. Phys. Usp.* 32, 75, 1989.
- [68] V. P. Frolov and A. A. Shoom, “Motion of charged particles near weakly magnetized Schwarzschild black hole,” *Phys. Rev. D* 82, 084034, 2010.
- [69] V. P. Frolov, “Weakly magnetized black holes as particle accelerators,” *Phys. Rev. D* 85, 024020 (2012).
- [70] <http://mathworld.wolfram.com/DescartesSignRule.html>
- [71] [https://en.wikipedia.org/wiki/Routh-Hurwitz\\_theorem](https://en.wikipedia.org/wiki/Routh-Hurwitz_theorem)

- [72] R. M. Wald, “Black hole in a uniform magnetic field,” *Phys. Rev. D* 10, 1680, 1974.
- [73] A. Papapetrou, “Champs gravitationnels stationnaires a symetrie axiale,” *Ann. Inst. H. Poincare Phys. Theor. IV* 4.2, 83, 1966.
- [74] P. Jovanovic, “The broad Fe K- $\alpha$  line and supermassive black holes,” *New Astron. Rev.* 56, 37, 2012.
- [75] A. C. Fabian, K. Iwasawa, C. S. Reynolds and A. J. Young, “Broad iron lines in active galactic nuclei,” *Publ. Astron. Soc. Pac.* 112, 1145, 2000.
- [76] C. S. Reynolds and M. A. Nowak, “Fluorescent iron lines as a probe of astrophysical black hole systems,” *Phys. Rept.* 377, 389, 2003.
- [77] K. Fukumura and S. Tsuruta, “Iron K- $\alpha$  fluorescent line profiles from spiral accretion flows in AGNs,” *Astrophys. J.* 613, 700, 2004.
- [78] H. Bateman, *Tables of Integral Transforms*, McGraw-Hill, 1954
- [79] M. Fox, *Quantum Optics: An Introduction*, Springer, Oxford University Press, 2006
- [80] R. K. Bock and W. Krischer, *The Data Analysis Brief Book*, Springer, 1998
- [81] C. S. Reynolds and M. C. Begelman, “Iron fluorescence from within the innermost stable orbit of black hole accretion disks,” *Astrophys. J.* 488, 109, 1997.
- [82] B. C. Bromley, K. Chen, and W. A. Miller, “Line emission from an accretion disk around a rotating black hole: toward a measurement of frame dragging,” *Astrophys. J.* 475, 57, 1997.

- [83] A. F. Zakharov, A. A. Nucita, F. DePaolis, and G. Ingrosso, “Observational features of black holes,” gr-qc/0507118.
- [84] A. F. Zakharov, “Shapes of Fe  $K\alpha$  lines from annuli near black holes,” *Physics of Atomic Nuclei* 70.1, 159, 2007.
- [85] V. Karas, D. Vokrouhlicky, and A. G. Polnarev, “In the vicinity of a rotating black hole: A fast numerical code for computing observational effects,” *Monthly Notices of the Royal Astronomical Society* 259.3, 569, 1992.
- [86] K. Chen and J. P. Halpern. “Structure of line-emitting accretion disks in active galactic nuclei-ARP 102B,” *The Astrophysical Journal* 344, 115, 1989.
- [87] K. Chen, J. P. Halpern, and A. V. Filippenko. “Kinematic evidence for a relativistic Keplerian disk-ARP 102B,” *The Astrophysical Journal* 339, 742, 1989.
- [88] A. C. Fabian, M. J. Rees, L. Stella, and N. E. White, “X-ray fluorescence from the inner disc in Cygnus X-1,” *Mon. Not. Roy. Astron. Soc.* 238, 729, 1989.
- [89] L. Stella, “Measuring black hole mass through variable line profiles from accretion disks,” *Nature* 344, 747, 1990.
- [90] G. Matt, G. C. Perola, L. Piro, and L. Stella, “Iron K-alpha line from X-ray illuminated relativistic disks,” *A&A* 257, 63, 1992.
- [91] C. T. Cunningham, “The effects of redshifts and focusing on the spectrum of an accretion disk around a Kerr black hole,” *Astrophys. J.* 202, 788, 1975.

- [92] G. Bao, P. Hadrava, and E. Ostgaard, "Emission-line profiles from a relativistic accretion disk and the role of its multiple images," *ApJ* 435, 55, 1994.
- [93] C. Fanton, M. Calivani, F. Felice, and A. Cadez, "Detecting accretion disks in active galactic nuclei," *PASJ* 49, 159, 1997.
- [94] A. Cadez, C. Fanton, and M. Calvani, "Line emission from accretion discs around black holes: the analytic approach," *New Astronomy* 3, 647, 1998.
- [95] J. A. Petterson, "Magnetic field of a current loop around a Schwarzschild black hole," *Phys. Rev. D* 10, 3166, 1974.
- [96] A. M. A. Zahrani, V. P. Frolov, and A. A. Shoom, "Critical escape velocity for a charged particle moving around a weakly magnetized Schwarzschild black hole," *Phys. Rev. D* 87, no. 8, 084043, 2013.
- [97] Y. Nakamura and T. Ishizuka, "Motion of a charged particle around a black hole permeated by magnetic field and its chaotic characters," *Astrophys. Space Sci.* 210, 105, 1993.
- [98] M. Takahashi and H. Koyama, "Chaotic motion of charged particles in an electromagnetic field surrounding a rotating black hole," *Astrophys. J.* 693, 472, 2009.
- [99] M. Santoprete and G. Cicogna, "Chaos in black holes surrounded by electromagnetic fields," *Gen. Rel. Grav.* 34, 1107, 2002
- [100] O. Kopacek, V. Karas, J. Kovar, and Z. Stuchlik, "Transition from regular to chaotic circulation in magnetized coronae near compact objects," *Astrophys. J.* 722, 1240, 2010.

- [101] A. A. Shoom, “Synchrotron radiation from a weakly magnetized Schwarzschild black hole,” *Phys. Rev. D* 92, no. 12, 124066, 2015.
- [102] M. Yu. Piotrovich, N. A. Silantév, Yu. N. Gnedin, and T. M. Natsvlishvili, “Magnetic fields of black holes and the variability plane,” arXiv1002.4948, 2010.
- [103] A. R. Prasanna and R. K. Varma, “Charged particle trajectories in a magnetic field on a curved space-time,” *Pramana* 8, 229, 1977.
- [104] L.D. Landau and E.M. Lifshitz, *Classical Theory of Fields*, Butterworth-Heinemann; 4 edition, 1980.
- [105] A. A. Sokolov, I. M. Ternov, A. N. Aliev, and D. V. Galtsov, “Synchrotron radiation in curved space-time,” *Sov. Phys. J.* 26, 36, 1983.
- [106] R. Ruffini and A. Treves, “On a magnetized rotating sphere,” *Astrophys. Lett.* 13, 109, 1973.

# Appendix A

## $\ell$ -parametrization of the orbit

For light from the emitter on a circular orbit that reaches a distant observer, there exists a relation between its angular momentum  $\ell$  and the angle  $\varphi$  where it was emitted. This relation follows from Eq. (3.17). In the numerical calculations it is convenient to consider  $\varphi$  as a function of  $\ell$ . Let us discuss the properties of this function.

From Eq. (3.17) one finds

$$\frac{d\Phi}{d\varphi} \frac{d\varphi}{d\ell} = \frac{dB_{\pm}(\ell, \zeta_e)}{d\ell}. \quad (\text{A.1})$$

Using the definition of  $\Phi$  in Eq. (3.17), one obtains

$$\frac{d\Phi}{d\varphi} = \frac{\sin \varphi \sin \theta_o}{\sqrt{\sin^2 \varphi + \cos^2 \theta_o \cos^2 \varphi}}. \quad (\text{A.2})$$

Hence,  $d\Phi/d\varphi$  is positive for  $\varphi \in (0, \pi)$  and negative for  $\varphi \in (-\pi, 0)$ . Using the

definition Eq. (2.60) of the function  $B(\ell, \zeta_e)$ , one gets

$$\frac{dB(\ell, \zeta_e)}{d\ell} = \int_0^{\zeta_e} \frac{d\zeta}{(1 - \ell^2(1 - \zeta)\zeta^2)^{3/2}}. \quad (\text{A.3})$$

From the above relations one concludes that for direct rays the sign of  $d\varphi/d\ell$  coincides with the sign of  $\varphi$ , that is it is positive for  $\varphi \in (0, \pi)$  and negative for the other segment of the trajectory.

Let us discuss now the case of indirect rays. Let us recall that a null ray has a radial turning point only when  $\ell > \ell_* = 3\sqrt{3}/2$ . The inverse radius of this turning point  $\zeta_m$  is a solution of the equation

$$(1 - \zeta_m)\zeta_m^2 = \ell^{-2}, \quad (\text{A.4})$$

and it belongs to the interval  $(0, 2/3)$ . Differentiating this relation with respect to  $\ell$  one gets

$$\frac{d\zeta_m}{d\ell} = -\frac{2}{\ell^3\zeta_m(2 - 3\zeta_m)} < 0. \quad (\text{A.5})$$

Using the definition Eq. (3.12) of the function  $C(z)$ , one finds

$$\frac{dC(z)}{dz} = \int_0^1 \frac{(y^4 - 3y^2 + 3)dy}{Z^{3/2}}. \quad (\text{A.6})$$

Let us notice that both the derivatives,  $dB/d\ell$  and  $dC/dz$ , are positive definite. (For  $dC/dz$  this is because  $y^4 - 3y^2 + 3 > 0$ ).

Using Eq. (3.17) we obtain

$$\frac{d\Phi}{d\varphi} \frac{d\varphi}{d\ell} = \frac{dB_-(\ell, \zeta)}{d\ell} = 2 \frac{dC(z_m)}{d\zeta_m} \frac{d\zeta_m}{d\ell} - \frac{dB(\ell, \zeta_e)}{d\ell}. \quad (\text{A.7})$$

Both of the terms in the right-hand side of Eq. (A.7) are negative. Eq. (A.2) implies that the sign of  $d\Phi/d\varphi$  coincides with the sign of  $\varphi$ . To summarize,  $d\varphi/d\ell$  is negative in the interval  $\phi \in (0, \pi)$  and positive in the other half of the circle.

## Appendix B

### Radiation from a point-like source

In this appendix we discuss the following problem. Suppose one has a point-like source emitting photons. Denote its 4-velocity by  $\mathbf{u}$ . Denote by  $\tau$  the proper time along the emitter world line. Choose a moment of time  $\tau_e$  and consider a local frame  $\mathbf{e}_a$  ( $a = 0, \dots, 3$ ) at this point. We choose  $\mathbf{e}_0 = \mathbf{u}$ . We consider one of the emitted at  $\tau_e$  photons and call it a *reference photon*. Its initial 4-momentum  $\mathbf{p}$  can be written as follows:

$$\mathbf{p} = \omega_e(\mathbf{u} + \mathbf{N}), \quad \omega_e = -(\mathbf{p}, \mathbf{u}). \quad (\text{B.1})$$

Here  $\omega_e$  is the frequency of the photon in the rest frame of the emitter and  $\mathbf{N}$  is a unit vector orthogonal to  $\mathbf{u}$ . It determines the spatial direction of the reference photon. We choose the vector  $\mathbf{e}_1$  to coincide with  $\mathbf{N}$ . The other two unit vectors  $\mathbf{e}_2$  and  $\mathbf{e}_3$  of the frame are chosen to be orthogonal to both the vectors  $\mathbf{e}_0$  and  $\mathbf{e}_1$ . They are fixed up to a rotation and uniquely (up to the orientation) determine a 2-plane  $\Pi$  orthogonal to  $\mathbf{e}_0$  and  $\mathbf{e}_1$ . We denote the corresponding bi-vector by

$\mathbf{e}_2 \wedge \mathbf{e}_3$ .

Consider a bundle of photons emitted in the direction close to  $\mathbf{N}$  within a solid angle  $\Delta\Omega_e$  which is determined by two vectors  $\Delta_1\mathbf{N}$  and  $\Delta_2\mathbf{N}$ , orthogonal to  $\mathbf{N}$ . The vectors of this bundle can be parameterized as follows

$$\mathbf{N} + \alpha_1\Delta_1\mathbf{N} + \alpha_2\Delta_2\mathbf{N}, \quad \alpha_{1,2} \in (-1/2, 1/2). \quad (\text{B.2})$$

The solid angle  $\Delta\Omega_e$  coincides with the area of the parallelogram in  $\Pi$  determined by these two vectors, which is

$$\Delta\Omega_e = \|\Delta_1\mathbf{N} \wedge \Delta_2\mathbf{N}\| \equiv |\Delta_1N^2\Delta_2N^3 - \Delta_1N^3\Delta_2N^2|, \quad (\text{B.3})$$

where  $\Delta_1N^i$  and  $\Delta_2N^i$  are components of  $\Delta_1\mathbf{N}$  and  $\Delta_2\mathbf{N}$  in the 2D basis  $\{\mathbf{e}_2, \mathbf{e}_3\}$ .

We assume now that the radiation of the emitter is isotropic and denote by  $\mathcal{N}\Delta\tau_e$  the total number of photons emitted during the time interval  $\Delta\tau_e$  of the proper time in the frame co-moving with the emitter. Then the corresponding number of photons emitted in the solid angle  $\Delta\Omega_e$  is

$$n_e\Delta\tau_e = \frac{\mathcal{N}}{4\pi}\Delta\Omega_e\Delta\tau_e. \quad (\text{B.4})$$

The solid angle  $\Delta\Omega_e$  can also be determined by the relation

$$\mathbf{u} \wedge \mathbf{N} \wedge \Delta_1\mathbf{N} \wedge \Delta_2\mathbf{N} = \pm\Delta\Omega_e\mathbf{E}, \quad (\text{B.5})$$

where  $\mathbf{E}$  is the unit 4-form

$$\mathbf{E} = \mathbf{e}_0 \wedge \mathbf{e}_1 \wedge \mathbf{e}_2 \wedge \mathbf{e}_3. \quad (\text{B.6})$$

Adding to  $\mathbf{N}$  the vector  $\mathbf{u}$  does not change the value of the wedge product in the left-hand side of Eq. (B.5). Similarly, adding the vectors proportional to  $\mathbf{u}$  and  $\mathbf{N}$  to the vectors  $\Delta_1 \mathbf{N}$  and  $\Delta_2 \mathbf{N}$  does not change this wedge product. As a result one can rewrite Eq. (B.5) in the form

$$\frac{1}{\omega_e^3} \mathbf{u} \wedge \mathbf{p} \wedge \Delta_1 \mathbf{p} \wedge \Delta_2 \mathbf{p} = \pm \Delta \Omega_e \mathbf{E}, \quad (\text{B.7})$$

or, which is equivalent, in the form

$$\Delta \Omega_e = \pm \frac{1}{\omega_e^3} e_{\mu_1 \mu_2 \mu_3 \mu_4} u^{\mu_1} p^{\mu_2} \Delta_1 p^{\mu_3} \Delta_2 p^{\mu_4}. \quad (\text{B.8})$$

Here  $e_{\mu_1 \mu_2 \mu_3 \mu_4} = \sqrt{-g} \epsilon_{\mu_1 \mu_2 \mu_3 \mu_4}$  is the totally skew symmetric tensor and  $\epsilon_{\mu_1 \mu_2 \mu_3 \mu_4}$  is the Levi-Civita symbol.

# Appendix C

## Small oscillations

In this Appendix we consider small oscillations about a circular orbit. The equations of motion for charged particles in the weakly magnetized Schwarzschild spacetime are

$$\frac{d^2 x^\mu}{d\sigma^2} + \Gamma^\mu_{\nu\lambda} \frac{dx^\nu}{d\sigma} \frac{dx^\lambda}{d\sigma} = \frac{q}{m} F^\mu{}_\kappa \frac{dx^\kappa}{d\sigma}. \quad (\text{C.1})$$

The only nonzero Christoffel symbols,  $\Gamma^\mu_{\nu\lambda}$ , for the Schwarzschild spacetime are

$$\begin{aligned} \Gamma^\theta_{r\theta} &= \frac{1}{r}, & \Gamma^\phi_{r\phi} &= \frac{1}{r}, & \Gamma^r_{rr} &= -\frac{1}{1 - \frac{2M}{r}} \frac{M}{r^2}, \\ \Gamma^T_{rT} &= \frac{1}{1 - \frac{2M}{r}} \frac{M}{r^2}, & \Gamma^r_{\theta\theta} &= -r + 2M, & \Gamma^\phi_{\theta\phi} &= \cot \theta, \\ \Gamma^r_{\phi\phi} &= -\left(1 - \frac{2M}{r}\right) \sin^2 \theta r, & \Gamma^\theta_{\phi\phi} &= -\frac{\sin 2\theta}{2}, \\ \Gamma^r_{TT} &= \left(1 - \frac{2M}{r}\right) \frac{M}{r^2}. \end{aligned} \quad (\text{C.2})$$

We write the coordinates of the perturbed circular trajectory  $x^\mu(\tau)$  as  $x^\mu(\tau) + \delta^\mu(\tau)$ . By linearizing the equations (C.1) and changing the proper time ( $\tau$ ) to the

coordinate time ( $T$ ), one obtains

$$\frac{d^2 \delta^\mu}{dT^2} + c^\mu{}_\nu \frac{d\delta^\nu}{dT} + \delta^\kappa V^\mu{}_{,\kappa} = \mathcal{O}^\mu(\delta), \quad (\text{C.3})$$

where

$$c^\mu{}_\nu = \left[ \frac{2}{\gamma} \Gamma^\mu{}_{\nu\lambda} \frac{dx^\lambda}{d\sigma} - \frac{q}{m\gamma} F^\mu{}_\nu \right] \Big|_{\theta=\pi/2}, \quad (\text{C.4})$$

$$V^\mu{}_{,\kappa} \equiv \frac{\partial}{\partial x^\kappa} V^\mu = \left[ \frac{1}{2} \frac{\partial}{\partial x^\kappa} \left( \frac{1}{\gamma} c^\mu{}_\nu \frac{dx^\nu}{d\sigma} - \frac{q}{m\gamma^2} F^\mu{}_\nu \frac{dx^\nu}{d\sigma} \right) \right] \Big|_{\theta=\pi/2}. \quad (\text{C.5})$$

Here we keep only the terms linear in  $\delta^\mu$ . Thus  $\mathcal{O}^\mu(\delta)$  stands for terms of higher order in  $\delta^\mu$ . Due to the fact that the spacetime is axially symmetric the only nonzero components of  $V^\mu$  and  $c^\mu{}_\nu$  are

$$\begin{aligned} c^r{}_\phi &= (-r + 2M) \sin^2 \theta \left[ \frac{qB}{m\gamma} + 2\Omega \right], & c^\phi{}_r &= \frac{qB}{m\gamma r} + 2\frac{\Omega}{r}, \\ c^r{}_T &= -2 \frac{(-r + 2M)M}{r^3}, & c^T{}_r &= -\frac{2M}{(-r + 2M)r}, \\ c^\theta{}_r &= \sin(2\theta) \left[ \frac{qB}{2m\gamma} + \Omega \right], & c^\phi{}_\theta &= \cot \theta \left[ \frac{qB}{m\gamma} + 2\Omega \right], \\ V^r &= (-r + 2M) [\sin^2 \theta (\Omega_B + \Omega) \Omega - \Omega_K^2], \\ V^\theta &= \frac{\sin(2\theta)}{2} \Omega [\Omega_B + \Omega]. \end{aligned} \quad (\text{C.6})$$

Here

$$\Omega_K = \sqrt{\frac{M}{r^3}}, \quad \Omega_B = \frac{qB}{m\gamma}. \quad (\text{C.7})$$

Setting in Eqs. (C.3) the index  $\mu = 0$  where zero corresponds to the time component, we get

$$\frac{d^2\delta^T}{dT^2} + c^T_r \frac{d\delta^r}{dT} = 0, \quad (\text{C.8})$$

For the index  $\mu = 3$  (the  $\phi$ -component) we get

$$\frac{d^2\delta^\phi}{dT^2} + c^\phi_r \frac{d\delta^r}{dT} = 0. \quad (\text{C.9})$$

Integrating equations (C.8) and (C.9), we get the following equations respectively (the integration constants are ignored):

$$\frac{d\delta^T}{dT} + c^T_r \delta^r = 0, \quad (\text{C.10})$$

$$\frac{d\delta^\phi}{dT} + c^\phi_r \delta^r = 0. \quad (\text{C.11})$$

Next by setting in equation (C.3) the index  $\mu = 1, 2$  (or  $\mu = r, \theta$  respectively) and taking into account equations (C.8) and (C.9), we get

$$\begin{aligned} \frac{d^2\delta^r}{dT^2} + \omega_r^2 \delta^r &= 0, \\ \frac{d^2\delta^\theta}{dT^2} + \omega_\theta^2 \delta^\theta &= 0. \end{aligned} \quad (\text{C.12})$$

From these equation we can see that the motion in the  $r$ - or  $\theta$  - directions is an oscillation. In equation (C.12) we have

$$\omega_r = \left[ \sqrt{V^r_{,r} - c^r_t c^t_r - c^r_\phi c^\phi_r} \right]_{\theta=\frac{\pi}{2}}, \quad (\text{C.13})$$

$$\omega_\theta = \left[ \sqrt{V^{\theta, \theta}} \right]_{\theta=\frac{\pi}{2}} = \Omega_K . \quad (\text{C.14})$$

These equation are the frequencies of the oscillations in the  $r$ - or  $\theta$  - directions. In analogy with the harmonic oscillator, we can calculate the  $\omega_r$  from Eq. (C.13) in the following way:

$$\omega_r^2 = \frac{U_{,rr}}{2} = \frac{\mathcal{E}^2 M}{r^2 (r - 2M)^2} (r - 6M) + \frac{4\tilde{b}^2}{r} (r - 2M) , \quad (\text{C.15})$$

where  $U$  is the effective potential given as follows,

$$U = \left( 1 - \frac{2M}{r} \right) \left[ 1 + \left( \frac{\mathcal{L} - \tilde{b}r^2}{r} \right)^2 \right] . \quad (\text{C.16})$$

If we rescale regarding  $r_g$ , then the dimensionless frequencies for the small oscillations in the  $r$ - and  $\theta$ - direction become

$$\Omega_\theta = r_g \omega_\theta = r_g \Omega_K , \quad (\text{C.17})$$

$$\Omega_\rho^2 = r_g^2 \omega_r^2 = \frac{\mathcal{E}^2}{2\rho^2} \frac{\rho - 3}{(\rho - 1)^2} + \frac{4b^2}{\rho} (\rho - 1) . \quad (\text{C.18})$$

## Appendix D

# Time of a charged particle on a circular orbit

In this Appendix we give an estimation of the time that a charged particle remains in a circular motion of a given radius. We assume that the only source of energy loss is the synchrotron radiation. When a charged particle moves in a uniform and constant magnetic field in flat spacetime it emits radiation; such radiation is called synchrotron radiation. The production of such radiation means that the particles are losing energy and angular momentum and gradually move to smaller radius. The energy loss in flat spacetime is given by the following formula (see e.g [104]),

$$\frac{dE}{dT} = \frac{2e^2v^4\gamma^4}{3r^2c^3}. \quad (\text{D.1})$$

For Eq. (D.1) we consider that the particle density is not very high otherwise we have damping of radiation.

In the paper [105] the power of the synchrotron radiation for ultra relativistic

particles on a circular orbit in Kerr spacetime was estimated,

$$\frac{dE}{dT}_{Kerr} = \frac{e^2}{6r^4} \left( \frac{E}{m} \right)^4 \frac{[\Omega^2(3r^2 + a^2) - 1]^2}{\sqrt{\Delta}\Omega^3}. \quad (\text{D.2})$$

If we set  $a = 0$  and take the limit  $r \gg M$ , then we get

$$\frac{dE}{dT} = \frac{e^2}{6r^4} \left( \frac{E}{m} \right)^4 \left[ 4r^2 - 8Mr - 12M^2 - 16\frac{M^3}{r} - 16\frac{M^4}{r^2} + O\left(\frac{M^6}{\Omega^4}\right) \right] \quad (\text{D.3})$$

As we can see in the zero-order approximation, we get the non-general relativistic formula (D.1). For the ultra relativistic case and for  $c = 1$ ,

$$\frac{dE}{dT} = \frac{2e^2}{3r^2} \left( \frac{E}{m} \right)^4. \quad (\text{D.4})$$

Let us make the following transformation in equation (D.1),

$$c = G = 1, \quad E = \mathcal{E}m, \quad T = tr_g, \quad r = \rho r_g. \quad (\text{D.5})$$

Thus we get the dimensionless energy loss,

$$\frac{d\mathcal{E}}{dt} = \lambda \frac{2v^4\gamma^4}{3\rho^2}, \quad (\text{D.6})$$

where  $\lambda = \frac{e^2}{r_g m}$ . This formula implies

$$\frac{d\rho}{dt} = \lambda \frac{2v^4\gamma^4}{3\rho^2} \left[ \frac{d\mathcal{E}}{d\rho} \right]^{-1}. \quad (\text{D.7})$$

From equation (D.7) we have

$$t = \frac{1}{\lambda} \int_{\rho_1}^{\rho_2} \frac{3\rho^2}{2v^4\gamma^4} \left[ \frac{d\mathcal{E}}{d\rho} \right] d\rho, \quad (\text{D.8})$$

where

$$l = \frac{-b\rho^2 + \sqrt{4b^2\rho^4 + 4b^2\rho^6 - 8b^2\rho^5 + 2\rho^3 - 3\rho^2}}{2\rho - 3}, \quad (\text{D.9})$$

$$\mathcal{E} = \sqrt{1 - \frac{1}{\rho}} \sqrt{1 + \frac{(l - b\rho^2)^2}{\rho^2}}, \quad (\text{D.10})$$

$$\Omega = \frac{\rho - 1}{\rho E} \left( \frac{l}{\rho^2} - b \right), \quad (\text{D.11})$$

$$v = \frac{\Omega\rho}{\sqrt{1 - 1/\rho}}, \quad (\text{D.12})$$

$$\gamma = \frac{1}{\sqrt{1 - v^2}}. \quad (\text{D.13})$$

$$(\text{D.14})$$

For our model,  $b = 2.25$ , and for  $\rho_1 = 1.20$  and  $\rho_2 = 1.21$  we will get

$$t = \frac{1}{\lambda} 0.027. \quad (\text{D.15})$$

Let us now estimate the parameter  $\lambda$ . For an electron we have

$$\frac{e^2}{m} = 2.818 \times 10^{-13} \text{ cm}.$$

For a stellar mass black hole with ten times the mass of the sun, the gravitational radius is going to be  $r_g = 3 \times 10^6$  cm. For a black hole of an arbitrary mass we

would have  $r_g = 3 \times 10^5 M/M_\odot$  cm. Therefore,

$$\lambda = \frac{e^2}{mr_g} = 9.393 \times 10^{-19} \frac{M_\odot}{M}.$$

The time will be

$$t = 2.874 \times 10^{16} \frac{M}{M_\odot}. \quad (\text{D.16})$$

If we multiply this by the characteristic time for stellar mass black hole ( $t_g = r_g/c = 10^{-5} M/M_\odot$  sec) in order to have the time in seconds, we get

$$T_{12} = \frac{t_g}{\lambda} \int_{\rho_1}^{\rho_2} \frac{3\rho^2}{2v^4\gamma^4} \left[ \frac{d\mathcal{E}}{d\rho} \right] d\rho, \quad (\text{D.17})$$

and for the particular example of  $\rho_1 = 1.20$  and  $\rho_2 = 1.21$  the value of  $T_{12}$  is

$$T_{12} = 2.874 \times 10^{11} \left( \frac{M}{M_\odot} \right)^2 \text{ sec}. \quad (\text{D.18})$$

The age of the universe in seconds is  $4.351 \times 10^{17}$ . Thus, for the particle that is orbiting a black hole mass  $M \sim 10^3 M_\odot$  to move from  $\rho = 1.21$  to  $\rho = 1.20$  by losing only synchrotron radiation it will take more than than half of the age of the universe (or 0.658 times the age of the universe).

# Appendix E

## Charge accretion

As we mentioned, a magnetic field modifies the motion of charged particles around a black hole. This effect may be reduced<sup>1</sup> due to the selective charge accretion. In the case of a uniform magnetic field which is aligned along the symmetry axis of the black hole, if there is a preferential rotation direction of the charged particles then, while the negatively charged particles are repelled due to Lorentz force the positively charged particles are pulled into the black hole. Thus, a black hole in a magnetic field surrounded by an ionized interstellar medium will selectively accrete charged particles. So, the black hole is getting electrified. Note that an accretion disk can give a preferential rotation direction and hence a preferential sign of the charge to be pulled into the black hole. Similar effects are discovered in flat spacetime for a conducting sphere [106]. Let us see under which conditions the selective charge accretion cancels out the modification of the orbits of charged particles due to magnetic field.

To discuss selective charge accretion, we consider a weakly magnetized and

---

<sup>1</sup> If the selective charge accretion is very high then the position of ISCO for charged particles can be even further from the black hole than the position of ISCO for neutral particles.

electrified black hole. From the solution of Maxwell's equation we have

$$A^\mu = -\frac{Q}{r_g}\xi_{(t)}^\mu + \frac{B}{2}\xi_{(\phi)}^\mu, \quad (\text{E.1})$$

where the factors  $Q/r_g$  and  $B/2$  come from the properties of the Maxwell tensor and Gauss law (see [72]) where  $Q$  is the charge of the black hole. For a Schwarzschild black hole with  $Q \neq 0$  and  $B = \text{const}$ , we have the following constants of motion,

$$\begin{aligned} E &= -\xi_{(t)}^\mu P_\mu = \left(1 - \frac{r_g}{r}\right) \left[ m \frac{dT}{d\sigma} - q \frac{Q}{r_g} \right], \\ L &= \xi_{(\phi)}^\mu P_\mu = r^2 \sin^2 \theta \left[ m \frac{d\phi}{d\sigma} + q \frac{B}{2} \right]. \end{aligned} \quad (\text{E.2})$$

These are analogous to (2.7, 2.8) for a charged and magnetized black hole. For the equatorial plane and by making the following transformations,

$$\begin{aligned} \mathcal{E} &= \frac{E}{m} & l &= \frac{L}{mr_g}, \\ r &= r_g \rho & T &= r_g t & \sigma &= r_g \tau, \\ \tilde{Q} &= \frac{qQ}{mr_g} & b &= \frac{qB r_g}{2m}, \end{aligned} \quad (\text{E.3})$$

we get

$$\begin{aligned} \mathcal{E} &= \left(1 - \frac{1}{\rho}\right) \left[ \frac{dt}{d\tau} - \tilde{Q} \right], \\ l &= \rho^2 \left[ \frac{d\phi}{d\tau} + b \right]. \end{aligned} \quad (\text{E.4})$$

From the third integral of motion,  $g_{\mu\nu} u^\mu u^\nu = -1$  we have

$$\left(\frac{d\rho}{d\tau}\right)^2 = \mathcal{E}^2 - \left(1 - \frac{1}{\rho}\right) \left[1 - 2\mathcal{E}\tilde{Q} - \tilde{Q}^2 \left(1 - \frac{1}{\rho}\right) + \frac{(\ell - b\rho^2)^2}{\rho^2}\right]. \quad (\text{E.5})$$

Let us define

$$V(\rho) = \mathcal{E}^2 - \left(1 - \frac{1}{\rho}\right) \left[1 - 2\mathcal{E}\tilde{Q} - \tilde{Q}^2 \left(1 - \frac{1}{\rho}\right) + \frac{(\ell - b\rho^2)^2}{\rho^2}\right]. \quad (\text{E.6})$$

If we set  $\tilde{Q} = 0$ , we get the effective potential of a weakly magnetized black hole. For particles in the innermost stable circular orbits (ISCO), we need the following conditions to be satisfied,

$$\begin{aligned} V(\rho) &= 0, \\ \frac{dV(\rho)}{d\rho} &= 0, \\ \frac{d^2V(\rho)}{d\rho^2} &= 0. \end{aligned} \quad (\text{E.7})$$

It is very difficult to solve these equations analytically. However, it can be done numerically. In the case  $\tilde{Q} = 0$ , the position of ISCO is coming closer to the horizon while the magnetic field is increasing. Numerical analysis of (E.7) shows that when  $\tilde{Q} \neq 0$  and while this parameter is increasing the location of ISCO is moving away from the horizon.

Let us estimate the dimensionless parameter  $\tilde{Q}$  of a black hole when a proton falls into it. Assume that while an electron is revolving around the black hole because of the repulsive Lorentz force on it, a proton falls into the black hole due to the attractive Lorentz force on it. We have  $q_e = -4.8 \times 10^{-10} (\text{g cm}^3/\text{s}^2)^{1/2}$ ,

$q_p = 4.8 \times 10^{-10} (\text{g cm}^3/\text{s}^2)^{1/2}$  and  $m_e = 9 \times 10^{-28}$  g. Moreover, in the formula for  $\tilde{Q}$  we need to restore the speed of light. Therefore,

$$\tilde{Q} = \frac{qQ}{m c^2 r_g} = -9 \times 10^{-20}. \quad (\text{E.8})$$

The numerical analysis shows that if the parameter  $\tilde{Q} \sim 1$  then the effect can be observable. If for every proton falling into a black hole the parameter  $\tilde{Q}$  changes only as such as in equation (E.8), we need large number of protons in order to have an observable effect in the orbits of the charged particles in a weakly magnetized spacetime. Moreover, in order to take such effect into account we need to consider a specific model for the disk. Something like this is beyond the purpose of this thesis. In this thesis we shall simply ignore the modification of ISCO due to charge accretion.

Note that we are not considering values of  $\tilde{Q}$  that cause back-reaction.